University of California
Santa Barbara

Search for direct top squark pair production in single lepton final states at a center-of-mass energy of 13 TeV with the CMS detector

A dissertation submitted in partial satisfaction
of the requirements for the degree

Doctor of Philosophy
in
Physics

by

Sicheng Wang

Committee in charge:

Professor Claudio Campagnari, Chair
Professor Jeffrey Richman
Professor Nathaniel Craig

September 2021

The Dissertation of Sicheng Wang is approved.

Professor Jeffrey Richman

Professor Nathaniel Craig

Professor Claudio Campagnari, Committee Chair

August 2021

Search for direct top squark pair production in single lepton final states at a center-of-mass energy of 13 TeV with the CMS detector

by

Sicheng Wang

Acknowledgements

First and foremost, I would like to acknowledge and thank my advisor, Claudio Campagnari, for all his support and guidance during my six years with UCSB. I would also like to thank professor Jeffrey Richman and Nathaniel Craig for kindly be on my committee, as well as for the classes you have taught on particle physics.

I must also thank my fellow students, Nick Amin, Bennett Marsh and Seth Koren, as well as the senior students Alex George and Jason Gran, for your friendship, for the wonderful tools you have developed that have helped me in bringing out this result, and for the various discussions we had about physics. My thanks also go to Frank Golf, Indara Suarez for your guidance and criticism in doing physics analysis, including this one. I would also like to thank Hannsjörg Weber and Ulaşcan Sarıca for your help and input into this analysis.

During my study, I have also learned a lot from professor David Stuart during the MTD project, from other members of the Surf-n-Turf group, from members of the CSC group who have taught me a lot about the detectors, and from people in the ODMB project. There are many others who have offered friendship and shared knowledge with me during my PhD study, including but not limited to Manuel, Ana, Chunxiao, Neelay, Hualin. Please note that I do value our friendship and the time we spent together.

Though they may not be able to read this, I must thank my parents for all their support of me in getting into whatever things I like to do over the past 29 years.

Curriculum Vitæ

Sicheng Wang

Education

2021	Ph.D. in Physics (Expected), University of California, Santa Barbara.
2018	M.A. in Physics, University of California, Santa Barbara.
2015	B.Sc. in Physics and Mathematics, Hong Kong University of Science and Technology, Hong Kong.

Publications

- CMS Collaboration, "Search for direct top squark pair production in events with one lepton, jets, and missing transverse momentum at 13 TeV with the CMS experiment", *JHEP* **05** (2020) 032. [doi:JHEP05(2020)032], [arXiv:1912.08887]

Abstract

Search for direct top squark pair production in single lepton final states at a center-of-mass energy of 13 TeV with the CMS detector

by

Sicheng Wang

Results are presented for a search for top squark pair production using a sample of proton-proton collision data recorded at a center-of-mass energy of 13 TeV by the CMS experiment at the LHC during 2016, 2017 and 2018, corresponding to an integrated luminosity of 137.2 fb^{-1}. The search is carried out using events with a single isolated electron or muon, multiple jets and large transverse momentum imbalance and is tuned to have high sensitivities for a variety of top squark pair production processes, as described by simplified models of supersymmetry. Novel techniques have been applied to boost the signal sensitivity and data-driven methods have been applied to estimate the main backgrounds. The observed data are found to be consistent with expectations from Standard Model processes, and exclusions are set in the context of simplified top squark pair production models in terms of the masses of the top squark and the lightest supersymmetric particle, assumed to be the neutralino. Depending on the model, top squark masses up to 1.2 TeV are excluded for models with a massless neutralino, while neutralino of masses up to 600 GeV are excluded for models with top squark masses of 1 TeV, at the 95% confidence level.

Contents

Chapter 1

Introduction

1.1 The Standard Model

The Standard Model (SM) [1, 2, 3] is a quantum field theory that describes three of the four fundamental forces of nature: the string, electromagnetic and weak interactions. In the quantum field theory of the SM, particles are described as the excitations of the quantum fields, and that explains our observation that all particles of the same type share the same set of properties. Particles are further categorized based on their intrinsic spin as "fermions" (for half-integer spin) and "bosons" (for integer spin), while the fermions are further divided into leptons (include the charged leptons and neutrinos) and quarks. The bosons include the photon, the 8 gluons, the $W^{\pm}$ and Z bosons, and the Higgs boson. The symmetry underlying the electromagnetic, weak, and strong interactions among these 61* known particles can be described within the structure of the gauge

*The counting include both the type and charges of particle and assumes neutrinos are Dirac.

group

$$\mathrm{SU}(3) \otimes \mathrm{SU}(2)_L \otimes \mathrm{U}(1)_Y.$$

Table 1.1 summarizes the types of the fundamental fermions in the SM in terms of the charges under the gauge group that each type carries and the masses[†] of the particles in the 3 generations. The SM does not give a reason on why the values are assigned in this way, and they are determined completely from the observations. There are (to our current understanding) 26 free parameters in the SM. They are the masses (or the Yukawa couplings to the Higgs field) of the 12 fermions, the vacuum expectation value and the mass of the Higgs boson, 3 gauge coupling constants, 8 angles that determine the mixing among the 3 generations of fermions in the electroweak interaction, and the strong CP phase.

Table 1.1: Summary of field contents and the masses of the fermions. Each type of fermion contains 3 generations with different masses. The weak hypercharge of the "left-handed" and "right-handed" fermions are labeled as Y_L and Y_R, respectively, while the weak isospin $I_{\mathrm{W}}^{(3)}$ is only non-zero for the "left-handed" fermions. The quarks are charged under the SU(3) group and each of them carries 1 of the 3 "colors". Q represents the electric charge of the fermions and is completely determined by the weak isospin and the hypercharge by $Q = I_{\mathrm{W}}^{(3)} + Y/2$. The charge conjugate of the fermions, or "anti-fermions", will see a sign flip in Q. The upper bounds on the masses of the neutrinos are taken from the cosmological observation [4] on the sum of the 3 neutrino masses.

Fermion	$I_{\mathrm{W}}^{(3)}$	Y_L	Y_R	Q	Colored	m(1st gen.)	m(2nd gen.)	m(3rd gen.)
Neutrinos	$+\frac{1}{2}$	-1	0	0	No	$< 0.26\,\mathrm{eV}$	$< 0.26\,\mathrm{eV}$	$< 0.26\,\mathrm{eV}$
Charged leptons	$-\frac{1}{2}$	-1	-2	-1	No	$0.511\,\mathrm{MeV}$	$106\,\mathrm{MeV}$	$1.78\,\mathrm{GeV}$
u-type quarks	$+\frac{1}{2}$	$+\frac{1}{3}$	$+\frac{4}{3}$	$+\frac{2}{3}$	Yes	$\sim 2\,\mathrm{MeV}$	$1.3\,\mathrm{GeV}$	$173\,\mathrm{GeV}$
d-type quarks	$-\frac{1}{2}$	$+\frac{1}{3}$	$-\frac{2}{3}$	$-\frac{1}{3}$	Yes	$\sim 5\,\mathrm{MeV}$	$\sim 0.1\,\mathrm{GeV}$	$4.2\,\mathrm{GeV}$

[†]In this thesis, we use the natural units, in which $\hbar = c = 1$.

The Standard Model is the most successful theory on the fundamental building blocks of our nature: the elementary particles. In spite of this, it is still an unfinished theory that needs further development. It is widely believed that our current SM is an effective field theory up to the electroweak scale (describing physics interactions up to an energy $\sim 100\,\mathrm{GeV}$), and new theories at a higher energy scale will eventually come in.

1.2 Beyond the Standard Model

We know that there are still limitations of the SM, and there are many mysteries from our observations of the world that are not yet (well) explained in the current format of the SM.

On the observation front, one mystery is the nature of Dark Matter (DM), whose existence has been receiving growing evidence from astronomical observations [5, 6] while the current SM does not include any particle that can be a good candidate for it. On the theory front, one such mystery is the "naturalness" problem [7], also called the hierarchy problem or the fine-tuning problem, that describes the "unnatural" cancellation that is needed to achieve a small Higgs boson mass that is observed. In the current SM, the leading term of the quantum loop corrections for the Higgs boson mass is given by

$$\delta m_{\mathrm{H}}^2 \sim |y_{\mathrm{t}}|^2 \left[-\Lambda_{\mathrm{UV}}^2 + 3m_{\mathrm{t}}^2 \log\left(\frac{\Lambda_{\mathrm{UV}}^2 + m_{\mathrm{t}}^2}{m_{\mathrm{t}}^2} \right) + \cdots \right],$$

where Λ_{UV} is the energy scale that we expect new physics would come in to replace the

SM that we are familiar with. If we expect the current SM to be valid up to the Planck scale ($\sim 10^{19}\,\text{GeV}$), or at least the scale of a Grand Unified Theory ($\sim 10^{16}\,\text{GeV}$), we would find a huge correction term to the Higgs mass.

This does not pose a direct contradiction to the observed Higgs mass at 125 GeV, as it can in principle be solved by fine-tuning the bare mass term (which is a free parameter) to cancel the loop corrections and bring the observed Higgs mass to electroweak scale $\sim 100\,\text{GeV}$. However, this would seem highly unnatural, to have two extremely large numbers (quadratic in Λ_{UV}), that are otherwise random, happen to land at an extremely narrow window to cancel each other and just happened to bring the Higgs mass from Λ^2_{UV} back to the electroweak scale. From the history of physics, we consider this as a strong hint for a new physics mechanism (or symmetry) to be involved and there can be a "natural" solution to such mysteries within the extended SM by this mechanism (symmetry).

1.2.1 The top squark for the naturalness problem

Among all the extensions of the current Standard Model, supersymmetry (SUSY) [8, 9] is one of the most attractive. Mathematically, SUSY is the only remaining spacetime symmetry that is allowed in a consistent 4-dimensional quantum field theory [10]. It is a symmetry between bosons and fermions, and predicts the existence of a superpartner for every SM particle (referred to as sparticles) that share the same quantum numbers as their SM partners except for differing by one half unit in the spin. Specifically, we call

the superpartners of the fermions squarks and sleptons, the superpartner of the gluons gluinos, the superpartner of the gauge bosons gauginos, and the superpartner of the Higgs bosons higgsinos[‡].

SUSY has to be a broken symmetry since no SUSY particles (that would have the same mass as their SM partner if SUSY is an exact symmetry) has been observed. Under such assumption, the gauginos and higgsinos mix together to form mass eigenstates, and depending on whether they are charged or not, they are called charginos ($\tilde{\chi}^{\pm}_{1,2,3,4}$) and neutralinos ($\tilde{\chi}^{0}_{1,2}$). In many SUSY models that conserve the R-parity [11], the lightest supersymmetric particle (LSP) is often the $\tilde{\chi}^{0}_{1}$ which is neutral and stable. This makes the LSP a great candidate for dark matter, providing also a connection with cosmology.

SUSY provides a natural solution to the quadratic divergences of the Higgs boson mass, since by including contributions from the SUSY particles their quadratic divergent terms naturally cancels with the ones from SM particles because of the fermion boson symmetry. In order to keep the Higgs mass natural, i.e., not too far from the Electroweak scale, the masses of the top squark ($\tilde{\mathrm{t}}$, also called stop), higgsino, and gluino cannot be too large as well, while the masses of other superpartners do not matter much for this problem [12]. In particular, the leading quadratic divergence from the top quark contribution is canceled by the contribution from stop, since it shares the same Yukawa coupling strength as the top quark. The quantum correction to the Higgs mass as a

[‡]In minimal supersymmetry, there need to be at least 2 complex Higgs doublets, which leaves 5 real scalar degrees of freedom after 3 being "eaten" by the W and Z bosons. So there can be at least 5 Higgs bosons, and hence at least 5 higgsinos.

function of m_{t} and $m_{\tilde{\mathrm{t}}}$ is given by

$$\delta m_{\mathrm{H}}^2 \sim |y_{\mathrm{t}}|^2 \left[-\Lambda_{\mathrm{UV}}^2 + 3m_{\mathrm{t}}^2 \log\left(\frac{\Lambda_{\mathrm{UV}}^2 + m_{\mathrm{t}}^2}{m_{\mathrm{t}}^2}\right) + \Lambda_{\mathrm{UV}}^2 - 3m_{\tilde{\mathrm{t}}}^2 \log\left(\frac{\Lambda_{\mathrm{UV}}^2 + m_{\tilde{\mathrm{t}}}^2}{m_{\tilde{\mathrm{t}}}^2}\right) + \cdots \right].$$

Although the quadratic divergence is canceled nicely with the inclusion of stop, it is not hard to see that the mass to the top squark ($m_{\tilde{\mathrm{t}}}$) enters the quantum correction to the Higgs mass itself, at the one loop level. This means that if $m_{\tilde{\mathrm{t}}}$ is too high, it can be the source of a fine-tuning problem itself. This motivates us to look for the top squark around the TeV scale at hadron colliders as they would be able to get produced through the strong interaction.

1.3 The Large Hadron Collider

The Large Hadron Collider (LHC) [13] is built to collide high energy protons to trigger interesting particle interactions that are not part of our normal life and also, hopefully, produce new particles that are not already included in the SM. It is constructed and operated by the European Organization for Nuclear Research (CERN) through a collaboration with thousands of universities and research institutes around the world. It is physically residing in a 26.7 km circular shape tunnel, 50–175 m deep beneath the border of France and Switzerland, near Geneva.

The LHC is the last section of a series of hadron accelerating facilities, with two concentric rings to hold/accelerate two beams of hadrons in the opposite directions, and

they can have intersections at 8 different points along the rings. Protons entering the LHC with an energy of 450 GeV can be accelerated by the 400 MHz radio-frequency (RF) cavities to reach a designed energy of 7 TeV, enabling a proton-proton (pp) collision of center-of-mass energy ($\sqrt{s}$) at 14 TeV. During the "Run II" data taking periods between 2015 and 2018, the LHC had been running pp collisions at $\sqrt{s} = 13$ TeV.

For the most part, the protons are just traveling in the straight sections, while they are turned around by the superconducting dipole magnets that can generate magnetic field up to 7.7 T at 1232 different points for bending the 6.5 TeV proton beam, and there are a further 392 quadrupole magnets to focus the beam.

Each proton beam is separated into thousands of bunches of protons that are arriving at a frequency of 40 MHz. This is a nature outcome of the acceleration by RF cavities, but also enables the detectors to record the collisions at each bunch crossing as "event". The intensity of the beam collision is quantified by luminosity (L), which is calculated from the number of protons in the bunch, the number of bunches, the frequency of the bunch crossings, effective area of the beam and has a unit of $\mathrm{cm}^{-2}\mathrm{s}^{-1}$. This, in combination with the cross section (σ) of the physics process, gives the event rate of the process as $L \cdot \sigma$.

During the running in 2018, the LHC reached a peak luminosity of $2 \times 10^{34}\,\mathrm{cm}^{-2}\mathrm{s}^{-1}$ and average pile-up (i.e. number of pp interactions happening at a single bunch crossing) of about 55.

1.4 Compact Muon Solenoid

The Compact Muon Solenoid (CMS) [14, 15] is a general purpose detector, located at one of the collision point of the LHC proton rings ("point 5" of LHC near the French town Cessy).

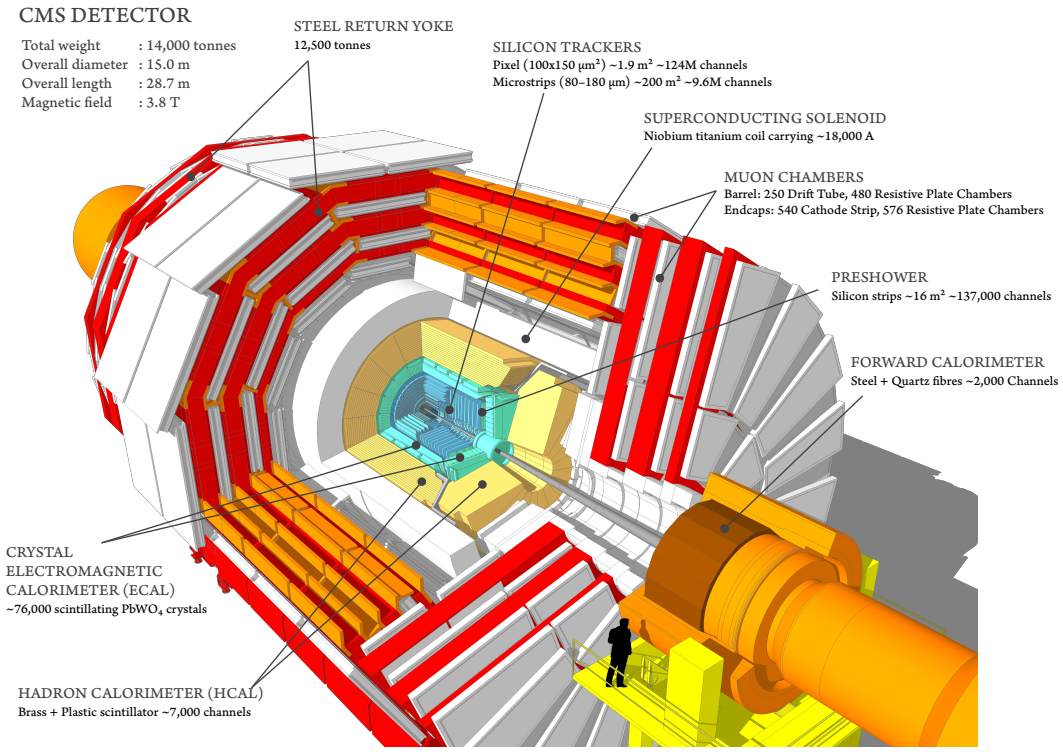

Figure 1.1: A cutaway view for the components and their specifications for the CMS detector, from [16].

The CMS detector is 21 m long and 15 m tall cylindrical shape, consisting of several concentric layers of subdetectors enclosed or around the superconducting solenoid magnet generating the magnetic field. A detailed arrangement and specifications of these subdetectors are shown in Figure 1.1. The size of the detector for modern high energy physics experiments is driven by the necessity to have enough path length for precisely

measure the bend of the charged particles in the magnetic field, by the thickness needed to absorb photons and hadrons in the calorimeter and the need to measure muon trajectories in an outer spectrometer. The CMS detector features a compact design by packing as much subdetectors as possible within the solenoid to reduce the volume and hence the cost of the crystal electromagnetic calorimeter. It is also designed to achieve an excellent muon measurement with a redundant muon detecting system using the gas-ionization chambers embedded in the steel flux-return yoke outside the solenoid.

Particles originating from the interaction point are more commonly described in (η, ϕ) coordinate, where ϕ describes the direction at the transverse plane (i.e. the plane perpendicular to the beamline), and η is the pseudorapidity defined by $\eta \equiv -\ln[\tan(\theta/2)]$ where θ is the angle between the 3-vector of the particle and the z-axis, taken to be the direction along the beamline. The $\phi = 0$ correspond to the direction pointing to the center of the LHC ring, but we do not expect any physics process happening at the LHC to take a preference at the absolute ϕ angle, and only the difference in ϕ between the particles can have physical meaning.

1.4.1 The detector structure

Figure 1.2 shows a slice of the CMS detector in the transverse plane. The subdetectors in the barrel region and examples of how particles may behave traveling through these detector components are given. These subdetector systems are discussed in more detail below.

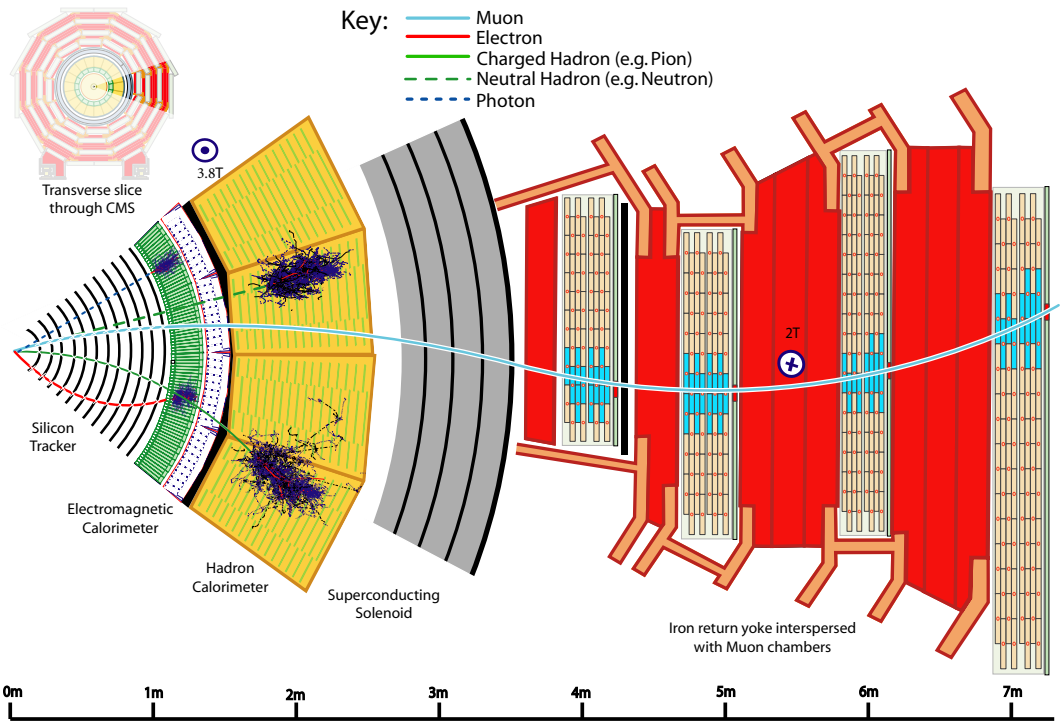

Figure 1.2: The specific particle interactions in a transverse slice of the CMS detector from [17].

Solenoid

The central feature of the CMS apparatus is the superconducting solenoid of 6 m internal diameter, providing a nearly homogeneous magnetic field of 3.8 T, mainly limited by the mechanical strain it exert on the holding structures of the detector. Charged particles traveling through this magnetic field will bend in the transverse direction, with curvature proportion to field strength, their momentum and the charge over mass ratio. The strong field makes particle identification and momentum measurement possible using the compact detector design. The solenoid is accompanied by 4 layers of steel flux-return yoke to regulate the magnetic field outside the solenoid. This return field further helps

with the measurement on the momentum of the muons by the muon chambers.

Silicon Tracker System

The CMS tracker system [18, 19] sits at the innermost layer of the CMS detector, consisting of a total of 14 layers of silicon detectors (4 pixel layers + 10 strip layers) providing high-resolution trajectories for the charged particles when they pass through. The operating principle is that doped silicon that can form electron-hole pairs when charge particles pass through. These electrons/holes drift to the anode/cathode under the voltage difference that is applied and collected by the readout electronics as electronic signals.

The tracker system is further divided into 4 layers of pixel detectors in the barrel and 3 disks in the endcap, with standard size of pixel at $100 \times 150\,\mu\text{m}^2$. and ensuring there can be 4 hits at the pixel detectors for particles within $|\eta| < 2.5$. With the addition of an extra layer of the pixel detectors in 2017, the closest layer is only 2.9 cm to the beamline, just 6 mm apart from the beam pipe. The pixel detectors are surrounded by 10 barrel layers and 12 disks of strip detectors with width of the silicon strips ranging from 80–180 μm and length from 20–25 cm. It is the essential component for the vertex reconstruction, charge particle identifications and is the main driver for measuring the momentum of muons with transverse momentum (p_{T}) less than 200 GeV.

For HL-LHC running conditions, the average pile-up of each bunch crossing can reach above 140, posing new challenges for the vertex reconstruction as there will be much less

average spacing between them. To tackle this challenge, the tracker system is expected to receive an extra outermost layer that can have timing resolution down to 30 ps, to further separate the tracks by their timing difference within a bunch crossing.

Electromagnetic Calorimeter (ECAL)

The ECAL of the CMS detector [20] is divided into ECAL Barrel (EB), covering pseudorapidity range up to $|\eta| < 1.479$, and ECAL Endcap (EE) that is mounted on the nose of the endcap disk and covers the range $1.479 < |\eta| < 3.0$. The major part of the ECAL is composed of scintillating crystals that are made of lead tungstate ($PbWO_4$), of a nearly cuboid shape pointing to the interaction point. The length of each crystal is 23 cm, corresponding to 25.8 times of the radiation length (0.89 cm), and the width is around 2.2–2.9 cm (2.2 cm for EB, 2.9 cm for EE), corresponding to the Molière radius (2.2 cm) in lead tungstate. The energy deposits are read out by photodiodes in the barrel and phototriodes in the endcap.

There is also a preshower detector just before the EE, to help identify boosted $\pi^0 \to \gamma\gamma$ decays that could fake an isolated photon. It is composed of 2 layers of lead radiator and silicon strip sensors for better granularity, and also adds 3 radiation lengths in thickness to the endcap.

Hadronic Calorimeter (HCAL)

There are 4 sections of the HCAL for the CMS detector. The major sections are the HCAL Barrel (HB) and HCAL Endcap (HE), fully enclosed within the solenoid

and covering the pseudorapidity range up to $|\eta| < 3.0$. They are sampling detectors with alternating layers of steel and brass layers to induce hadron showering, and layers of plastic scintillators to measure the shower energies. For the future upgrade of the CMS detector for HL-LHC era, the EE and HE at each endcap will be replaced by a High Granularity Calorimeter (HGCAL) [21] that will use silicon detectors instead of the scintillators for energy measurement.

The HCAL Forward (HF) are specifically designed calorimeters to capture energetic forward jets, placed outside the muon chambers at the endcaps, close to the beamline and 11.2 m from the interaction point. They are made of steel absorbers and embedded radiation hard quartz fibers parallel to the beamline to collect Cherenkov radiation. The HFs are the only subdetectors covering the high pseudorapidity range of $2.9 < |\eta| < 5.2$, and are important pieces that increase the hermeticity of the detector for good missing transverse energy ($E_{\mathrm{T}}^{\mathrm{miss}}$) measurements.

The HCAL Outer (HO), (not specifically drawn in Figure 1.1 or 1.2) is build in the barrel region just outside the solenoid as an additional tail-catcher for the energy that is not contained by EB and HB. It consists mainly just a thin layer of scintillators as the solenoid is serving as the absorber, and the total depth of the calorimeter is extended from 7.8 to at least 10 interaction lengths of the hadrons at the weakest point ($\eta = 0$). The inclusion of HO gives an overall improvement in the measurement of $E_{\mathrm{T}}^{\mathrm{miss}}$.

Muon System

The muon system of the CMS detector [22, 23] is located outside the solenoid, and works as extra tracking layers for the muons to extract their momentum. This is due to the feature of the muon, that it deposits very little energy when traveling through materials, making it almost impossible to build calorimeter. But also because of this, the muon system does not need to be inside the solenoid as muons can penetrate the materials without losing much of their energy.

Three different technologies are used to build a redundant muon detecting system for the CMS detector. The main driving forces are Drift tubes (DT) deployed in the barrel regions and Cathode Strip Chambers (CSC) deployed at both of the endcaps. Resistive Plate Chambers (RPC) are thin plate chambers deployed in between both of the DT and CSC layers to improve the timing.

The basic component of the DT is a rectangular shape drift tube of 42 mm wide, 13 mm thick and 2.4 m long, filled with a gas mixture of 85% Ar and 15% CO_2 and a 50 μm diameter anode wire is at the center of each tube. There are a total of 44 layers of these drift tubes surrounding the solenoid (8–12 layers per chamber), where 32 layers of them oriented along the beamline, providing a measurement focused on the ϕ direction of the muon. The DT chambers cover muons in the pseudorapidity region with $|\eta| < 1.2$, and the full 4 layers of DT chambers coverage is up to $|\eta| < 0.8$.

The CSC system consist of a total for 540 trapezoidal shaped chambers, distributed in 4 disks at each endcap and covering muons with $0.9 < |\eta| < 2.4$, within which the full

4-station CSC coverage is from $1.2 < |\eta| < 2.4$, and the muons within $0.9 < |\eta| < 1.2$ are detected by both DT and CSC. There are 6 layers of strips and wires in each chamber, filled with a gas mixture of $40\%\,\mathrm{Ar} + 50\%\,\mathrm{CO_2} + 10\%\,\mathrm{CF_4}$, with the strips serving as cathodes and the wires as anodes. The strips are aligned in the radial direction, are designed to have better spatial resolution for the muon, and The amount of charges collected at each strip is compared with the neighboring ones and a half-strip precision in the spatial resolution can be achieved for the muons. The wires are mostly perpendicular to the strips, except in the innermost ring of the first station, where the chambers are inside the solenoid and the wires are arranged with a tilting angle of 29° in those chambers. The timing information of the muon for offline analysis resolution is mainly determined from a template fit to the cathode pulse shape, and a resolution of 8 ns can be achieved for each cathode layer. This enables a 2 ns timing resolution for the muons detected by the 4 stations of the CSC system.

Charges collected by the strips in the CSC chambers are passed on to the on-chamber Cathode Front End Board (CFEB), where they get amplified and digitized. Data are collected continuously for every bunch crossing and are held by the CFEBs. They are not passed to the next level unless the trigger signal arrives in 3.2 μs, and most of the data collected are discarded at this stage. On the anode side, charges collected by the wires are amplified by the Anode Front End Boards (AFEB) and the data are held and fitted for an local charge track in the Anode Local Charged Track (ALCT) boards. These are called trigger primitives and this simple information is passed on to the Trigger Mother

Board (TMB) sitting at the peripheral crates just outside the CMS detector. For a proper data readout, data from both the CFEBs and the ALCT are passed to the Data Mother Board (DMB) sitting just beside the TMB. For a subset of the chambers which are expecting a higher rate or muon hits, data from CFEB and ALCT are passed through optical transmission and are read out by the Optical Trigger Mother Board (OTMB) and the Optical Data Mother Board (ODMB).

1.4.2 The trigger system

The LHC is producing collision events at an extremely high rate so that it is unfeasible to read out and store the information for all of them. Most of the events out of the 40 MHz bunch crossings are soft QCD events that are not interesting to us, while the events that are relevant for our physics interests are expected to happen at a rate of smaller than 10 Hz, considering the instantaneous luminosity and the pile-up condition. The trigger system is designed to make decisions on events as early as possible to accommodate the limits on readout bandwidth and storage capability.

The CMS trigger system [24] is composed of a two level system: a Level-1 (L1) trigger for fast decision on data readout, and a High Level Trigger (HLT) system for decision on storage of the event. The L1 trigger uses custom hardware processors to provide fast decision for the subdetectors in a fixed latency less than 4 μs. Its decisions are based on information that are taken from the calorimeters and the muon detectors, for signs of tracks or energy deposits compatible with muons, electrons, photons, jets,

or quantities calculated out of simple combinations of these primitive objects (e.g. the missing transverse momentum). It is designed to have an readout frequency at around 100 kHz for the collision events to be passed on to the next level.

The HLT has access to the full event readout from all subdetectors and runs a dedicated online reconstruction algorithm on a computer farm. The event content is now partially reconstructed, identification criteria are applied and more complex quantities (e.g. invariant masses) are available for event selection at this stage. The event rate passing HLT is reduced to less than 1 kHz before events are stored for offline analysis.

The particle-flow (PF) reconstruction algorithm [17] is used as early as in the HLT step, by correlating the basic elements collected from all relevant subdetectors to identify each final-state particle, and combining the corresponding measurements from these subdetectors to reach the final reconstruction of the particle property. Most notably, with the inclusion of tracker information in the reconstruction of the jets, charged particles with track associated with pile-up vertices can be excluded from the reconstruction of the jet momentum, with the a called charged hadron subtraction [17]. With the help of the muon detectors, the muon energy can also be associated with the jet in the rare cases when muons arise from the charged hadron decays.

Chapter 2

Search Strategy

2.1 The top squark at the LHC

In this search, we only consider scenarios that conserve R-parity, motivated by the non-observation of proton decay as well as the stable LSP assumption. Consequently, we would expect the SUSY particles to always be produced in pairs. The top squark can be pair produced in the LHC through the strong interactions. Figure 2.1 shows the cross section for the direct $\tilde{\mathrm{t}}\bar{\tilde{\mathrm{t}}}$ pair production at the LHC [25, 26], calculated at the approximate NNLO + NNLL as a function of the top squark mass. For reference, the most up-to-date estimated cross section for the SM $\mathrm{t}\bar{\mathrm{t}}$ pair production at the 13 TeV LHC is 831 pb, and this is 5 orders of magnitude larger than the $\tilde{\mathrm{t}}\bar{\tilde{\mathrm{t}}}$ pair production with $m_{\tilde{\mathrm{t}}} \sim 1\,\mathrm{TeV}$.

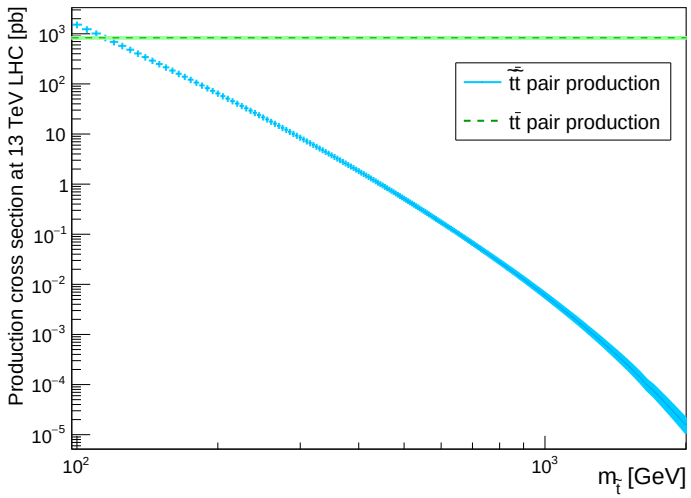

Figure 2.1: The cross sections for the direct $\tilde{t}\bar{\tilde{t}}$ pair production at the 13 TeV LHC, as a function of the top squark mass. For reference, the cross section for the SM $t\bar{t}$ pair production are drawn as dashed line.

2.1.1 The targeted signals

In this thesis, we present the search for $\tilde{t}\bar{\tilde{t}}$ production at the LHC in final states featuring a single lepton (where the lepton is an electron or a muon), multiple jets, and significant transverse momentum imbalance using data from pp collision at $\sqrt{s} = 13$ TeV, collected during the data taking periods of 2016–2018 by the CMS experiment. The total collected data correspond to an integrated luminosity of 137.2 fb^{-1}. We consider signal models where $\tilde{t}$ can decay into a top quark (t) and the lightest neutralino ($\tilde{\chi}_1^0$, which is also taken to be the LSP), or to a b quark and the lightest chargino ($\tilde{\chi}_1^{\pm}$). In the latter scenario, we assume $\tilde{\chi}_1^{\pm}$ decays to a W boson and $\tilde{\chi}_1^0$.

In this search, we consider the simplified models [27] that are featuring direct $\tilde{t}$ pair production in the following three possible decay scenarios:

- $pp \to \tilde{t}\bar{\tilde{t}} \to t^{(*)}\bar{t}^{(*)}\tilde{\chi}_1^0\tilde{\chi}_1^0$ (where t can be off-shell), also known as T2tt
- $pp \to \tilde{t}\bar{\tilde{t}} \to b\bar{b}\tilde{\chi}_1^+\tilde{\chi}_1^- \to b\bar{b}W^+W^-\tilde{\chi}_1^0\tilde{\chi}_1^0$, also known as T2bW
- $pp \to \tilde{t}\bar{\tilde{t}} \to t\bar{b}\tilde{\chi}_1^-\tilde{\chi}_1^0 \to t\bar{b}W^-\tilde{\chi}_1^0\tilde{\chi}_1^0$ (or its charge-conjugate), also known as T2bt

The corresponding diagrams of these processes are depicted in Figure 2.2.

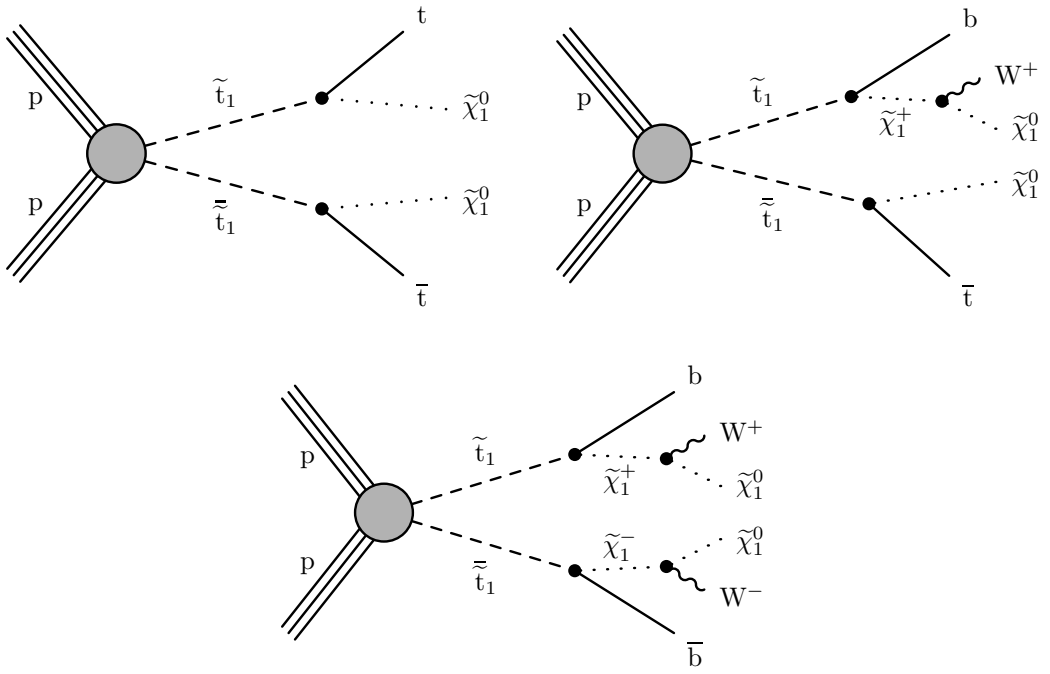

Figure 2.2: Diagrams of $\tilde{t}\bar{\tilde{t}}$ pair production with each top squark decaying into a t quark and a $\tilde{\chi}_1^0$ (top left), or a b quark and a $\tilde{\chi}_1^\pm$ that further decays into a W boson and a $\tilde{\chi}_1^0$ (top right) or allowing the $\tilde{t}$ to decay in both of the former cases (bottom).

Since there is not enough constraints on the masses of the SUSY particles, we scan the parameter space of the two most relevant SUSY particle masses, $m_{\tilde{t}}$ and $m_{\tilde{\chi}_1^0}$ for all 3 signal models. In the T2tt model, the masses of $\tilde{t}$ and $\tilde{\chi}_1^0$ determine the model completely, while in the other two models, the mass of the $\tilde{\chi}_1^\pm$ can also play a role, and it is fixed to a certain value depending on $m_{\tilde{t}}$ and $m_{\tilde{\chi}_1^0}$ in our considerations. For the T2tt model, the

branching fraction of $\tilde{t} \to t\tilde{\chi}_1^0$ is set to 100%, and $\Delta M(\tilde{t}, \tilde{\chi}_1^0) \equiv m_{\tilde{t}} - m_{\tilde{\chi}_1^0}$ is allowed to go as low as 87 GeV to allow some off-shell top quarks as propagators in the model. The minimum of $\Delta M(\tilde{t}, \tilde{\chi}_1^0)$ is set to 175 GeV for the T2bW models and 200 GeV for the T2bt models that are investigated. For the T2bW model, the branching fraction for $\tilde{t} \to b\tilde{\chi}_1^+$ is set to 100%, and the mass of $\tilde{\chi}_1^\pm$ has to be in between the masses of $\tilde{t}$ and $\tilde{\chi}_1^0$. In this analysis, we are only investigating the T2bW models with $m_{\tilde{\chi}_1^\pm} = 0.5(m_{\tilde{t}} + m_{\tilde{\chi}_1^0})$ as an example. For the T2bt model, the branching fractions for both $\tilde{t} \to t\tilde{\chi}_1^0$ and $\tilde{t} \to b\tilde{\chi}_1^\pm$ are set to be 50%, and we only investigate the scenarios where $m_{\tilde{\chi}_1^\pm} = m_{\tilde{\chi}_1^0} + 5\,\text{GeV}$. Hence we are expecting a very soft off-shell W from the $\tilde{t} \to b\tilde{\chi}_1^\pm$ branch of the decay in this signal model.

Previous searches for pair produced stop in all final states [28, 29, 30] with a smaller data set have probed and excluded the existence top squark under similar models with mass up to 1 TeV for a small mass $\tilde{\chi}_1^0$. This thesis describes the details of the search that is an extension to [29] and leads to the latest publication [31] on the full Run II data set.

2.2 Methodology

The snapshot of collisions obtained from the CMS detector are stored as "events" in the data format of ROOT [32]. They are analyzed with the ROOT C++ library, by assembling the raw data into physics objects and quantities. They can be further combined or extracted as physics "observables" and be quantified as a specific number for each event, and the counting of the numbers from all of the events that we are

interested in are shown in histograms. Due to the complex nature of high energy physics processes, the event content can rarely be unambiguously associated with a given physics process, and the analysis will be done through comparing the distributions of these physics quantities in the histograms. Finally "signal regions" (SR), will be defined as selection criteria on the events, and the counting of observed number of events in these signal regions are compared the expectations from a "background only" hypothesis and a "signal + background" hypothesis, to determine how likely the observed data suggest the existence of the signal or exclude its existence.

The following sections of this chapter will give an overview of how the search for top squark pair production in the single lepton final state is designed, what are the main physical observables to be used, and how the backgrounds are divided into different categories, without going into the details of their definitions. The choice of generators and cross sections used for the SM background processes will also be listed in this chapter.

Chapter 3 will introduce how physics objects are constructed, as well as the event selections we made based on them or on higher level variables constructed from these physics objects, and eventually the categorization of these events into what we call signal regions, where we build our sensitivity to the signals we are looking for. Details on the trigger selections and their efficiency measurement, the calibrations put on the physics objects are also discussed there.

Chapter 4 will discuss the details on the estimation of contributions from different SM background categories in the signal regions. This is the part that requires most

of the effort, to carefully study and understand the SM background contributions in the signal regions. Data-driven techniques are used to tackle the main backgrounds, by setting up control regions (CR) that target the specific background, and we can use the observed data in CR to understand the potential mismodeling from simulated samples and eventually reduce the reliance on simulation.

Chapter 5 will reveal our final observations in the signal regions, compare them with the prediction from a SM only hypothesis, and make interpretations as constraints on the targeted signal models when no obvious excess is seen (which is true in this case). Chapter 6 draws the conclusions based on the results we obtained from the observed data.

2.3 Signal topology and background composition

The first step is to identify the signal topology, namely understanding what is the final state to expect for the signal, and select only events with such features, to distinguish the signal against *any* recorded event. The most important action at this step, that has to be taken even before any data is recorded at the LHC, is to decide on a list of triggers to make sure that when signals are produced in the collision, they are recorded.

Figure 2.3 shows the most general picture of the possible decay scenarios in a T2tt model featuring a single lepton in its final state. From the picture, we see that the targeted signal topology will look much like a $t\bar{t}$ pair production decaying in the single lepton channel plus extra missing energy carried away by the two LSPs. Hence the final

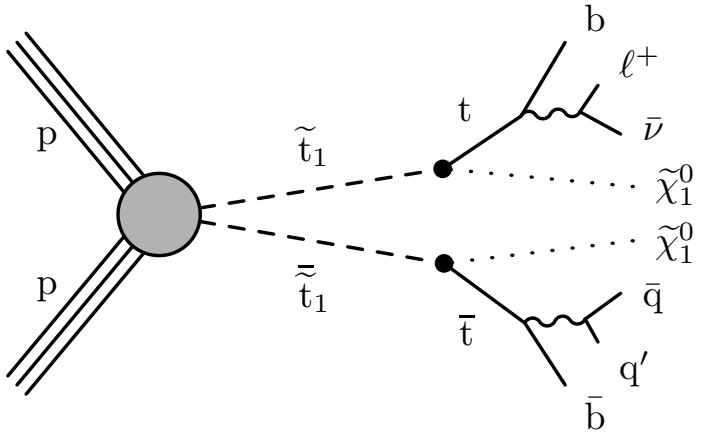

Figure 2.3: Diagram for $\tilde{t}$ pair production with each top squark decaying into a t quark and a $\tilde{\chi}_1^0$ into the single lepton channel.

state objects that can be targeted are similar to those of $t\bar{t} \to 1\ell + E_T^{miss}$ processes, i.e. 1 prompt lepton, some E_T^{miss}, at least 4 jets where 2 of them can be b-tagged. For the single lepton final state of the T2bW and T2bt models, the final state objects will be the same but they may have different kinematic properties from those in the T2tt models due to the differences in the intermediate particles. In the T2bt models the W boson from the $\tilde{t} \to b\tilde{\chi}_1^{\pm}$ branch of the decay will be very soft, and the quarks from the hadronic decay of this W boson may not be detected as jets if the $\tilde{\chi}_1^{\pm}$ does not have a lot of momentum, or they can form a single jet if the $\tilde{\chi}_1^{\pm}$ does have enough initial boost.

The most distinguishable triggering objects in such final states are lepton and large E_T^{miss}, hence events recorded by the single lepton and the E_T^{miss} triggers are to be used. The detail discussion of trigger selections and the estimation of their efficiencies are postponed until Section 3.2.

The second step is to identify the SM background process that can produce similar

final states. It is mentioned above that the final state will resemble $t\bar{t} \to 1\ell$. In fact the largest background will be coming from the single lepton $t\bar{t}$ decay if we only make requirements on the visible objects listed above, and there would be no hope in uncovering the $\tilde{t}\bar{\tilde{t}}$ production as the $t\bar{t}$ will have much higher production cross section and the $\tilde{t}\bar{\tilde{t}}$ signals will be inundated with the SM $t\bar{t}$ background.

The golden feature is, of course, that the $\tilde{t}\bar{\tilde{t}}$ event would have higher $E_{\mathrm{T}}^{\mathrm{miss}}$ in the event and we can always go to higher $E_{\mathrm{T}}^{\mathrm{miss}}$ to achieve a better signal to background discrimination, and this would be the central feature for all Dark Matter searches at the LHC (for which the R-parity conserved SUSY is part of). But we aim to do better than this, because when we go to high $E_{\mathrm{T}}^{\mathrm{miss}}$ we also loose the $\tilde{t}\bar{\tilde{t}}$ signals quickly.

The break points lies in the transverse mass (M_{T}) constructed from the lepton and the $\vec{p}_{\mathrm{T}}^{\,\mathrm{miss}}$, defined as

$$M_{\mathrm{T}} \equiv \sqrt{2p_{\mathrm{T}}^{\ell}E_{\mathrm{T}}^{\mathrm{miss}}\left(1-\cos(\phi^{\ell}-\phi^{\mathrm{miss}})\right)}$$

which is strictly less than the invariant mass of the lepton-neutrino system from the W decay, assuming the neutrino is the only source of the $\vec{p}_{\mathrm{T}}^{\,\mathrm{miss}}$. This means that M_{T} is bound by $m_{\mathrm{W}} \simeq 80.4\,\mathrm{GeV}$. While this will not be an exact cut off in the experimental signature due to the W bosons produced off-shell and smearing effects from the detector resolution, we shall still see a large drop off in the rate, as is visible in Figure 3.6.

With a minimum M_{T} cut to reject the majority of SM background, we are left with backgrounds from:

- **Lost lepton background**: events with more than one leptons produced but with

only one good lepton reconstructed.

- 1ℓ **background**: single lepton events that escape the M_{T} requirement.
- $\mathrm{Z} \to \nu\bar{\nu}$ **background**: events with Z boson produced and decayed invisibly.

ranking from larger to lower in their size of contributions.

The main SM processes contributing to the lost lepton background is $\mathrm{t\bar{t}}$ with both W bosons decaying leptonically, followed by single top productions (mainly tW) with ISR/FSR jets in the final states. This background emerges when one of the lepton in the event fails the selection requirements (p_{T}^{ℓ} lower than the p_{T} threshold, η^{ℓ} being out of acceptance or fails the identification criteria), is a non-isolated lepton, or is a hadronically decaying τ lepton that is not identified. This background is referred to as the "lost lepton" background and continues to dominate even after applying a carefully optimized second lepton veto (including an isolated track veto and hadronic τ veto) to suppress these events. It is the largest SM contribution to the signal regions after the preselections and is to be estimated in a data-driven way through the construction of a dilepton control regions. Detail of the estimation of this background is discussed in Section 4.1.

The left-over one lepton background after the high M_{T} requirement can be divided into two different categories based on the source of the lepton: whether the lepton comes from a W boson that is decay from top or a W boson produced promptly (i.e. events with W produced from pp interactions directly). For an event with the lepton coming from the W boson that is itself from a top quark decay (e.g. $\mathrm{t\bar{t}} \to 1\ell$ event), there is an extra limit

$M_{\mathrm{T}} < m_{\mathrm{t}}$. In the meantime, such extra constraint do not exist in event with the lepton coming from a prompt W boson decay (e.g. W+jets event). There are other differences between the $\mathrm{t\bar{t}} \to 1\ell$ events and W+jets events, such as the existence of b quark jets, the different production cross sections. While there is no reliable way to tell whether the lepton is coming from a top decay or not in the data, this categorization is only trying to differentiate them in our consideration and treatment for backgrounds coming from these two sources. One extra note is that the SM process of single top production in association with a W boson (tW) can contribute in both of these categories, depending on whether the prompt W boson is decaying leptonically, or the W from the t quark decay is decaying leptonically.

The dominant source of $\mathrm{Z} \to \nu\bar{\nu}$ background after the preselection is coming from $\mathrm{t\bar{t}Z}$ production where one of the two W bosons decays leptonically, with subdominant contribution from WZ. This background is not accounted for in either of the two previous estimation strategies because the invisibly decaying Z boson becomes a prompt invisible object itself, and this makes $\mathrm{t\bar{t}Z}$ an irreducible background as it presents the same final state as our signals. In the ideal scenario, this type of background shall be estimated in a data-driven way through the construction of dedicated trilepton control regions, and multiply yields in the control region by the $\mathrm{Z} \to \nu\bar{\nu}$ to $\mathrm{Z} \to \ell^+\ell^-$ ratio, which could be somewhere around 5. However, in most of our designed signal regions, the $\mathrm{Z} \to \nu\bar{\nu}$ contribution itself is already small in absolute scale, so any control region for $\mathrm{Z} \to \ell^+\ell^-$ in the similar final state phase space would not be feasible (i.e. we would not expect

any event produced). Hence we will estimate this type of background from simulation, evaluate all experimental systematic uncertainties, and use theoretical uncertainties such as the PDF and renormalization and factorization scale variations, and use the best known cross section normalization from a separate CMS measurement.

2.4 Simulated samples

Monte Carlo (MC) simulation is used to design the search, providing an insight into the construction and threshold setting for physical quantities as well as understanding the behavior and compositions of the backgrounds. It is also an essential part for the estimation of SM backgrounds, either by providing estimation directly (for 1ℓ from top and $Z \to \nu\bar{\nu}$ background), or it serve as an important component in data-driven methods (for lost lepton and 1ℓ from W backgrounds). MC is also the only way we can use to estimate the signals and to evaluate the sensitivity of the analysis. Various studies have been performed to verify the modeling of MC simulations in terms of object reconstruction/identification efficiencies and corrections are derived to correct for the mismodeling.

Samples of events of SM processes $t\bar{t}$, W + jets, Z + jets and simplified SUSY top squark pair production models are generated at the leading-order (LO) in quantum chromodynamics (QCD) using the MadGraph5_aMC@NLO 2 (2.2.2 or 2.4.2) generator [33]. The MadGraph5_aMC@NLO at next-to-leading-order (NLO) in QCD is used to generate samples of $t\bar{t}Z$, WZ, and $t\bar{t}W$ events, while single top quark (tW + others) events are generated at NLO in QCD using the POWHEG 2.0 [34, 35, 36, 37] program. Samples of

W+jets, $t\bar{t}$, and SUSY events are generated with four, three, and two additional partons included in the matrix element calculations, respectively.

Three different sets of detector simulations are used to generate events reflecting the running conditions and the amount of data collected during three distinct data taking periods in 2016, 2017 and 2018. Additionally, the generator settings are also different between the 2016 samples and the 2017–2018 samples. The NNPDF3.0 [38] parton distribution functions (PDFs) are used to generate all 2016 MC samples, while NNPDF3.1 [39] is used in the generation of the 2017 and 2018 samples, the events are reweighted to have the same PDF variations (NNPDF3.0) as the 2016 samples.

The parton shower and hadronization as well as the pile-up events are modeled with PYTHIA 8.2 (8.205 or 8.230) [40]. The MLM [41] and FxFx [42] prescriptions are employed to match partons from the matrix element calculation to those from the parton showers, for the LO and NLO samples, respectively.

Both the SM background and SUSY signal MC samples for 2016 are generated with the CUETP8M1 [43] PYTHIA tune. while the CP5 [44] tune is used to generate the background samples, CP2 tune is used to generate the signal samples for both 2017 and 2018. The GEANT4 [45] package is used to simulate the response of the CMS detector for all SM processes, while the CMS fast simulation program [46, 47] is used for SUSY signal samples, to reduce the CPU time and load. As a result, the corrections on efficiencies related to reconstructed objects are derived separately for the signal samples.

Table 2.1 lists the simulated samples used in this analysis, together with the cross

section. The sample name include information on the physics process, the generators that are used and the generator filters applied (if any).

Table 2.1: Simulated samples used in this analysis, listed with the corresponding theoretical cross sections and the effective integrated luminosity for the amount of events generated. The cross sections of the SM processes are taken for the best known estimations (usually NLO). The cross sections for the SUSY signals are based on values summarized in Figure 2.1 and determined by $m_{\tilde{t}}$ in the specific model.

Sample name	σ [pb]	L_{eff} [fb^{-1}]
TTJets_DiLept_Tune∗_13TeV-madgraphMLM-pythia8	87.3	956.6
TTJets_SingleLeptFromT_Tune∗_13TeV-madgraphMLM-pythia8	182.7	913.7
TTJets_SingleLeptFromTbar_Tune∗_13TeV-madgraphMLM-pythia8	182.7	855.7
ST_tW_antitop_5f_NoFullyHadronicDecays_Tune∗_13TeV-powheg-pythia8	19.6	375.4
ST_tW_top_5f_NoFullyHadronicDecays_Tune∗_13TeV-powheg-pythia8	19.6	313.3
ST_t-channel_top_4f_inclusiveDecays_Tune∗_13TeV-powheg-madspin-pythia8	136.02	900.5
ST_t-channel_antitop_4f_inclusiveDecays_Tune∗_13TeV-powheg-madspin-pythia8	80.95	795.5
ST_s-channel_4f_leptonDecays_Tune∗_13TeV-amcatnlo-pythia8	3.7	4982
W1JetsToLNu_Tune∗_13TeV-madgraphMLM-pythia8	11752	12.8
W2JetsToLNu_Tune∗_13TeV-madgraphMLM-pythia8	3841	15.7
W3JetsToLNu_Tune∗_13TeV-madgraphMLM-pythia8	1160	63.5
W4JetsToLNu_Tune∗_13TeV-madgraphMLM-pythia8	600	66.5
W1JetsToLNu_NuPt-200_Tune∗_13TeV-madgraphMLM-pythia8	2.36	6910
W2JetsToLNu_NuPt-200_Tune∗_13TeV-madgraphMLM-pythia8	4.95	5989
W3JetsToLNu_NuPt-200_Tune∗_13TeV-madgraphMLM-pythia8	4.94	7332
W4JetsToLNu_NuPt-200_Tune∗_13TeV-madgraphMLM-pythia8	8.83	7171
TTZToLLNuNu_M-10_Tune∗_13TeV-amcatnlo-pythia8	0.25	35576
TTZToQQ_Tune∗_13TeV-amcatnlo-pythia8	0.53	1335
WZTo1L3Nu_13TeV_amcatnloFXFX_madspin_pythia8_v2	3.05	1413
WZTo1L1Nu2Q_13TeV_amcatnloFXFX_madspin_pythia8	10.74	2374
WZTo3LNu_Tune∗_13TeV-amcatnloFXFX-pythia8	4.43	3146
WZTo2L2Q_13TeV_amcatnloFXFX_madspin_pythia8	5.60	8689
TTWJetsToLNu_Tune∗_13TeV-amcatnloFXFX-madspin-pythia8	0.20	34108
TTWJetsToQQ_Tune∗_13TeV-amcatnloFXFX-madspin-pythia8	0.40	2156
WWTo2L2Nu_NNPDF31_Tune∗_13TeV-powheg-pythia8	12.18	803.8
WWToLNuQQ_NNPDF31_Tune∗_13TeV-powheg-pythia8	50.00	731.0
ZZTo4L_13TeV_powheg_pythia8	1.25	78574
ZZTo2L2Q_13TeV_amcatnloFXFX_madspin_pythia8	3.22	11201
ZZTo2L2Nu_13TeV_powheg_pythia8	0.56	46132
ZZTo2Q2Nu_13TeV_amcatnloFXFX_madspin_pythia8	4.73	19939
DYJetsToLL_M-50_Tune∗_13TeV-madgraphMLM-pythia8	6021	56.2
SMS-T2tt_mStop-150to250_Tune†_13TeV-madgraphMLM-pythia8	–	–
SMS-T2tt_mStop-250to350_Tune†_13TeV-madgraphMLM-pythia8	–	–
SMS-T2tt_mStop-350to400_Tune†_13TeV-madgraphMLM-pythia8	–	–
SMS-T2tt_mStop-400to1200_Tune†_13TeV-madgraphMLM-pythia8	–	–
SMS-T2tt_mStop-1200to2000_Tune†_13TeV-madgraphMLM-pythia8	–	–
SMS-T2bW_Tune†_13TeV-madgraphMLM-pythia8	–	–
SMS-T2bt_Tune†_13TeV-madgraphMLM-pythia8	–	–

∗ = CUETP8M1 (2016) or CP5 (2017 & 2018)
† = CUETP8M1 (2016) or CP2 (2017 & 2018)

Chapter 3

Objects and event selections

In this analysis, we search for potential excess in events with a single isolated electron or muon, two or more jets where at least one of them is b tagged, and large $E_{\mathrm{T}}^{\mathrm{miss}}$. Events satisfying the above conditions but with additional electron or muon, any isolated track or hadronic τ are vetoed to reduce backgrounds that contain a lost lepton. The detailed definitions and selection criteria for these basic physics objects are described in Section 3.1. The baseline event selection criteria are described in Section 3.3, together with the description on event level kinematic variables like M_{T} and $\min \Delta\phi(j_{1,2}, \vec{p}_{\mathrm{T}}^{\mathrm{miss}})$ that are used to reduce the backgrounds. This section also includes the description on the construction of 2 dedicated search regions for signals with compressed scenarios. Finally, Section 3.4 introduces the helper variables t_{mod}, $M_{\ell \mathrm{b}}$ and top taggers and describes the division ("binning") of the events passing the baseline selections into individual signal regions based on these variables.

3.1 The physics objects

3.1.1 Leptons

Finding a good balance in the lepton (electron and muon) selection is an important part of this analysis. We want as many events as possible with one and only one prompt lepton in the final state, for which we would identify the lepton as a "good" lepton. At the same time, we want to avoid the events with objects detected as leptons, but are actually other charged particles misidentified as leptons, or are non-prompt leptons coming from the decay of hadrons and mesons.

In the rest of this thesis, the name lepton is generally used to stand for good leptons considered by this analysis, which would only include prompt electrons and muons, and not tau leptons, which are mostly decaying hadronically*. Events with prompt tau leptons are excluded in this analysis because they would require extra complexity that is out of the scope of this search. They will for sure be an important part of the picture if evidence of $\tilde{t}$ is established, and be included in the follow up analyses to measure the $\tilde{t}$ properties.

3.1.1.1 The electron and muon selections

The lepton identification is a set of criteria put on the properties of the reconstructed lepton objects to filter out possible fake leptons or non-prompt ones from the prompt leptons. Every kind of selection we use has to be a balance between efficiency for real

*Events with the tau lepton decaying leptonically, however, can be included or identified as the veto lepton if the electron or muon coming from the τ decay passes their corresponding selections. They consist less than 5% of events in our signal region.

leptons and the fake rate for other objects. Hence 3 different sets of criteria are used to select leptons for different purposes. In this analysis we defined them as *selection* and *veto* criteria, to select the one "good" lepton for signal region selection, or identifying any extra lepton that would veto the event, respectively. The requirement of having no additional *veto* lepton in the events helps to reduce the dileptonic $t\bar{t}$ background, which is the largest remaining background in our search regions. Additionally, a *trailing* criteria that is the same as the *veto* selection except with the p_T requirement raised to 10 GeV, is used when we do want to select a second lepton for the dilepton control region (see Section 4.1). The 3 sets of criteria are summarized in Table 3.1 for electrons and muons.

Our lepton identifications are selections based on recommendations from the standard CMS EGamma/Muon Physics Object Group (POG) cut-based selections [20, 48]. The one exception is that for both electrons and muons, the isolation requirements associated with the original recommendation are replaced by *mini-isolation* described below. The isolation of a lepton, generally defined as the sum of p_T of the hadronic particle flow candidates (p_T^{sum}) within some cone size R, is a measure of the hadronic activities near the lepton. It is a very good indication on whether the lepton is likely to be prompt (isolated) or is likely coming from the cascading decay of a quark (non-isolated). In the case of relative mini-isolation, this cone size R is a variable depending on the p_T of the lepton in question as:

$$R = \begin{cases} 0.2 & \text{if } p_T^\ell < 50\,\text{GeV}, \\ 10/p_T^\ell & \text{if } 50 < p_T^\ell < 200\,\text{GeV}, \\ 0.05 & \text{if } p_T^\ell > 200. \end{cases}$$

This sliding cone requirement avoids efficiency loss for signal topologies with boosted

top scenarios, in which case the lepton (usually high p_{T}) from the W decay and the corresponding b jet can be close to each other. Mini-isolation is also useful in maintaining efficiency of leptons in busy events, where a jet can be near a lepton by chance. By allowing the cone size to shrink with increased p_{T}^{ℓ}, fewer signal events would be vetoed due to the nearby jet fragments since the lepton can still be considered as isolated by mini-isolation. Pile-up mitigation on the calculation is performed via an effective area correction using the average energy density. The effective area is scaled by the size of the cone used by the mini-isolation algorithm.

Electrons are identified by the combined information of ECAL deposits and the hit patterns recorded by the silicon trackers. The quality of the electron is evaluated in terms the shower shape variable $\sigma_{i\eta i\eta}$, the HCAL energy versus the ECAL energy deposits (H/E), the η and ϕ difference between the (seed of the) cluster and inner track $\Delta\eta_{\mathrm{seed}}$ and $\Delta\phi_{\mathrm{in}}$, and the size of the energy momentum difference. The detail of the POG recommended identification requirements are listed in Table 3.2. For events with the electron serving as the selected lepton, we additionally require that the electron is within the coverage of EB (excluding the last two crystals), since previous studies have found higher fake rate with electrons in the endcap region that brings large one lepton backgrounds. By discarding the endcap electrons, we expect to only lose roughly 12%(5%) of the detectable stop signals with a single electron(lepton) final state.

Muons have a much cleaner signatures than the electrons. They are identified by the combined information of muon chamber hits and the hit patterns recorded by the silicon

Table 3.1: Requirement on *selection*, *veto* and *trailing* electrons and muons. The analysis requires exactly one selected lepton and no additional veto leptons. The *trailing* lepton selections are used only in the dilepton control region to select the second lepton, and is based on *veto* selections but with raised p_{T} requirement.

Type	Variable	Selection	Veto	Trailing
electron	p_{T}	$> 20\,\mathrm{GeV}$	$> 5\,\mathrm{GeV}$	$> 10\,\mathrm{GeV}$
	$\lvert\eta\rvert$	< 1.4442	< 2.4	< 2.4
	POG ID w/o Iso.	Medium	Veto	Veto
	Mini-isolation	< 0.1	< 0.2	< 0.2
muon	p_{T}	$> 20\,\mathrm{GeV}$	$> 5\,\mathrm{GeV}$	$> 10\,\mathrm{GeV}$
	$\lvert\eta\rvert$	< 2.4	< 2.4	< 2.4
	POG ID	Medium	Loose	Loose
	Mini-isolation	< 0.1	< 0.2	< 0.2

Table 3.2: EGamma POG recommended selection criteria for the electrons for veto and medium working point for electrons in barrel (endcap).

Variable	POG Veto ID	POG Medium ID
$\sigma_{i\eta i\eta}$	< 0.0126 (0.0457)	< 0.0106
$\lvert\Delta\eta_{\mathrm{seed}}\rvert$	< 0.00463 (0.00814)	< 0.0032
$\lvert\Delta\phi_{\mathrm{in}}\rvert$	< 0.148 (0.19)	< 0.0547
H/E	$< 0.05 + 1.16/E_{\mathrm{SC}} + 0.0324\ \rho/E_{\mathrm{SC}}$ ($< 0.05 + 2.54/E_{\mathrm{SC}} + 0.183\ \rho/E_{\mathrm{SC}}$)	$< 0.046 + 1.16/E_{\mathrm{SC}} + 0.0324\ \rho/E_{\mathrm{SC}}$
$\lvert\frac{1}{E} - \frac{1}{p}\rvert$	< 0.209 (0.132)	< 0.184

trackers. The POG recommended identification of the muon focus on the quality of the fit as well as the displacement from the PV.

3.1.1.2 Isolated track and hadronic τ veto

As explained in the introduction of this section, we are going to veto any events with hadronically decaying τ leptons, and the first thing we are going to consider is the isolated track veto.

Roughly 85% of all τ lepton decays result in only one charged particle, and this will be

referred to as "1-prong" decays, while the "3-prong" decays, with decays consisting of 3 charged particles, account for around 15%. Within the "1-prong" decays, the branching fractions to electrons and muons account for about 17.5% each, while the branching fractions to charged pions and kaons add up the remaining 50%. A single charged hadron plus possibly multiple neutral pions is thus the single largest fraction of all visible τ decay products. Accordingly, the obvious, and most powerful τ lepton veto is an isolated track veto using only the tracker isolation, so as to avoid having the neutral pion decay products of the τ lepton count towards the isolation sum.

In this analysis, an event is vetoed if one or more PF charged hadrons are found with the following criteria:

- $p_{\mathrm{T}}^{\mathrm{trk}} > 10\,\mathrm{GeV}$, $|\eta^{\mathrm{trk}}| < 2.4$, $d_{\mathrm{z}} < 0.1\,\mathrm{cm}$ to the PV
- Opposite sign in charge and $\Delta R > 0.4$ away from the selected lepton
- Require the tracker isolation $p_{\mathrm{T}}^{\mathrm{sum}} < \min\left(0.1 p_{\mathrm{T}}^{\mathrm{trk}}, 6\,\mathrm{GeV}\right)$ for a cone-size of 0.3

To further reduce the lost lepton background, we veto events with an additional hadronic τ in the event. The hadronic τ veto uses the POG recommended tau ID [49], and suppresses some 3-prong τ lepton decays that are not already vetoed by the isolated track veto. An event is vetoed if one or more hadronic τ leptons are reconstructed, meeting the following criteria:

- $p_{\mathrm{T}} > 20\,\mathrm{GeV}$, $|\eta| < 2.3$
- Opposite sign in charge and $\Delta R > 0.4$ away from the selected lepton

- Pass the machine learning based POG ID

3.1.2 Jets

Jets are the physical observable object of high energy quarks and gluons, formed by collimated sprays of hadrons resulting from the fragmentation of the original parton. These hadrons (in the order of hundreds) are constructed by the detector as PF candidates, and could be visually identifiable (through event display) as they are concentrated within a certain range in the η-ϕ space. Quantitatively they are clustered into jets using the anti-k_t algorithm [50, 51, 52], with a distance parameter of 0.4 (AK4 jets) or 0.8 (AK8 jets), for different purposes. The energy and direction of the original parton can be largely recovered by summing the 4-vectors of the included PF candidates. Hereafter in this thesis, the wording of jet will only be referring to an AK4 jet, and the AK8 jet serves only as input to the top tagger described in the later section.

Due to the existence of pile-up interactions, the clustering can be polluted by many soft hadrons coming from other vertices and result in an over-estimate of the original parton energy. The effect coming from charged particles are reduced with the charged hadron subtraction procedure, where tracker information is used to exclude the charged PF candidates associated with a pile-up vertex. For photons and neutral hadrons, this is not possible and their influence are hence corrected empirically, together with the correction for jet energy scales accounting for the nonuniformity in the detector response. These corrections are parameterized as a function of the pileup offset energy density, as

well as the jet area, η, and p_{T} on a jet-by-jet bases [53, 54].

A jet is considered good and counted in this analysis, if it passes the requirements

- $p_{\mathrm{T}} > 30\,\mathrm{GeV}$, $|\eta| < 2.4$
- $\Delta R > 0.4$ away from any selected, veto or trailing lepton
- Passes the tight ID recommended by the POG

where the ΔR requirement is avoiding double counting since every lepton would naturally be also reconstructed as a jet by the algorithm.

The tight ID requirement for jets are implemented to prevent counting fake jets that are actually picked up instrumental noises in the ECAL or HCAL, with the following requirements:

- Neutral hadronic energy fraction < 0.9
- Neutral electromagnetic energy fraction < 0.9
- Number of PF constituents > 1
- Charged hadronic energy fraction > 0
- Charged multiplicity > 0

Although a simple counting should suggest that our signals produces at least 4 jets, we do find cases where the signals could lose jets in the final states either because the hadronically decaying top acquire enough Lorentz-boost in some signal scenarios that

some or all of its decay products becomes unresolvable with a distance parameter of 0.4, or in some other signal scenarios the jets are usually soft that failed to pass the 30 GeV requirement in p_{T}, or the jet can be out of the η acceptance. So for the baseline selection, the requirement is lowered to be at least two jets in the events. The distribution of the number of jets after the baseline selections can be found at Figure 3.1.

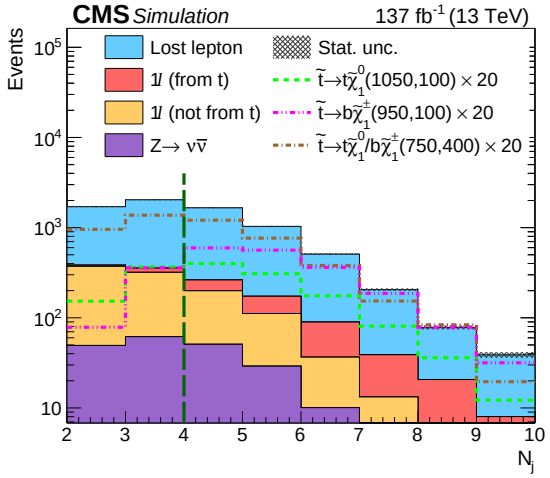

Figure 3.1: Distributions of number of jets from the simulation are shown after applying the preselection requirements that are described in Section 3.3.3. The stacked histograms are showing the SM background, whose categorizations are described in Section 2.3. The expectations for three example signal hypotheses are scaled up by 20 times and overlaid with the SM background, and the masses of the top squark and neutralino for the three hypotheses are listed in the parentheses of their legends, respectively. The last bin in each distribution includes the overflow events.

3.1.2.1 b tagging for jets

The b quark is a bit special experimentally, in that we may be able to identify the jet originating from the b quark, as hadrons containing b quarks tend to have longer lifetimes that allow them to travel a few millimeters before decaying, thus creating a secondary vertex for the tracks in the final state.

A combined secondary vertex algorithm that uses deep neural network, DeepCSV [55] is deployed on every identified jets, and makes use of information such as the tracks and secondary vertices to produce a discriminant on how likely the jet is to result from a b quark decay. Three different working points: *loose*, *medium* and *tight* are defined mainly based on their misidentification probability from light-flavor (udsg) jets, which are roughly at 10%, 1% and 0.1%, respectively, while the tagging efficiencies for real b jets are approximately 85%, 68% and 45%. The misidentification probability from c jets, which could also have long lifetime forming secondary vertices, can be much higher than the light-flavor jets and reach around 40%, 10% and 2%, respectively.

In this analysis, we make use of both the medium and tight working points to identify b jets among the selected good jets, in different signal regions, with the tight working point used for the high $M_{\ell \mathrm{b}}$ signal regions, and medium working point used in all other cases, including the definition of 0b control regions for the high $M_{\ell \mathrm{b}}$ SRs.[†]

3.1.3 Vertices

3.1.3.1 Primary vertex

Vertices are formed by fits to the trajectories of charged tracks [18], and they are considered as the physical location where the pp collision happens. For selected events, the vertex with the highest $\sum p_{\mathrm{T}}^2$ of tracks associated to it is required to satisfy the following criteria:

[†]See Section 3.4.1.2 for the definition of $M_{\ell \mathrm{b}}$ and Section 4.2 for the construction of the 0b CR.

- There are at least 5 degrees of freedom (see Ref. [18]) in the vertex fit.
- The distance along the beam line from the nominal center of the detector is less than 24 cm.
- The transverse displacement from the beam line is less than 2 cm.

This vertex is taken to be the primary vertex (PV) and all physics objects that are considered for each event, are required to originate from the PV.

3.1.3.2 Soft b object

Even for a normal SM $t\bar{t}$ decay, a non trivial fraction of the b quarks are actually produced with very little boost and hence may be very soft and may be out of the scope of our normal jet and b tagging requirement with $p_{\mathrm{T}} > 30\,\mathrm{GeV}$. The fraction of soft b could be even higher for the signal scenarios with compressed mass spectrum, hence we the ability to identify these soft b quarks based on only the presence of a secondary vertex (SV) using the Inclusive Vertex Finder algorithm [56] would be very helpful in the search of such signals. Additional requirements are put on the reconstructed SVs to suppress background originating from light quarks, and the selected SVs will be referred to as soft b tags.

The following requirements (developed by [28]) are applied for each SV to pass the soft b tagging definition:

- The p_{T} of the SV is less than 20 GeV

- The distance in the transverse plane between the SV and the PV is less than 3 cm
- The significance impact parameter (SIP3D) between the SV and the PV is greater than 4
- The angle between the displacement from PV to SV and the total four-momentum of the tracks associated to the SV ($\vec{p}_{\mathrm{SV}}$) is small, defined as $\cos\left(\overrightarrow{(\mathrm{PV},\mathrm{SV})}, \vec{p}_{\mathrm{SV}}\right) > 0.98$
- The number of tracks associated to the SV is greater or equal to 3
- The distance to any jet, $\Delta R(\mathrm{jet}, \vec{p}_{\mathrm{SV}})$, is greater than 0.4 away from any jets or leptons.

The soft b objects will only be used in the definition of one set of dedicated search regions for signals with compressed mass spectrum. It should be noted that the soft b tags are distinct objects (SVs) and are orthogonal to the identified PF jets and leptons, by construction. Another note would be that it is found that soft b objects are not more susceptible to fakes with increasing pile-up in the event, as can be seen in the more detailed study discussed in Appendix A.2.

3.1.4 The missing energy

The $p_{\mathrm{T}}^{\mathrm{miss}}$ or $E_{\mathrm{T}}^{\mathrm{miss}}$ represents the imbalance of the momentum of the observed physics objects in the transverse plane, where there should be a total sum of 0 in momentum from all the visible or invisible physics objects, by conservation of momentum. The same

constraint, unfortunately, cannot be enforced in the z-direction, since currently there's no practical way of measuring the momentum of the final state of the interaction in direction along the beam line at a proton-proton collider. In this thesis, the wording "missing transverse energy", labeled as $E_{\mathrm{T}}^{\mathrm{miss}}$ and "missing transverse momentum", labeled as $p_{\mathrm{T}}^{\mathrm{miss}}$ will be used interchangeably, and they represent the same physics object.

There can be many way to formally define $E_{\mathrm{T}}^{\mathrm{miss}}$, and the one being used in this analysis is based on the PF $E_{\mathrm{T}}^{\mathrm{miss}}$ [57, 58], calculated as the negative vector sum of all the momenta of particle flow candidates reconstructed in the event. The raw PF $E_{\mathrm{T}}^{\mathrm{miss}}$ would receive further corrections through the propagation of corrections derived for the jet energy scales discussed above. The jet energy scale corrections discussed previously are propagated to $E_{\mathrm{T}}^{\mathrm{miss}}$, where the jet energy corrections are applied to the jets in the $E_{\mathrm{T}}^{\mathrm{miss}}$ calculation.

The most famous known source of real missing momentum are neutrinos, which do in principle interact with normal materials through the weak interaction, but the rate is so low that there's no hope in building a neutrino detector in any practical way for a collider experiment. Apart from that, any real contribution can only be coming from undiscovered particles that do not interact, or at best interact very weakly with the normal matter we know and can be used to build detectors. This feature has made $E_{\mathrm{T}}^{\mathrm{miss}}$ the most important variable in searches for BSM models that feature a relatively stable undetectable particle in the final state, as it can be the direct signature for such a particle when it is produced during a collision event. In our case, this particle can be the

neutralino, serving also as the lightest supersymmetric particle in the SUSY models we are targeting. Whether they are themselves heavy in mass or not, they can carry large momentum and leave the detector undetected, creating additional $E_{\mathrm{T}}^{\mathrm{miss}}$ in the signal events.

Aside from the real contributions, there can also be fake $E_{\mathrm{T}}^{\mathrm{miss}}$ that arise from mismeasurements of the visible objects (most notably jets) as well as missing particles that are out of acceptance. Large mismeasurement of the jet happens rarely, but uninteresting QCD multi-jet process with large $E_{\mathrm{T}}^{\mathrm{miss}}$ from mismeasurement can still be very significant given the orders of magnitude higher cross section for strong interactions with the pp initial state. Fortunately, the QCD multi-jet process is not a concern in this analysis because of the isolated prompt lepton and the large $E_{\mathrm{T}}^{\mathrm{miss}}$ requirement, and all of our major backgrounds are processes with real $E_{\mathrm{T}}^{\mathrm{miss}}$ (neutrino) in the final state, combined with mismeasurement to some limited extent that produces some smearing effect in the $E_{\mathrm{T}}^{\mathrm{miss}}$ distribution.

For the baseline selection, a minimum of 250 GeV is required for the $E_{\mathrm{T}}^{\mathrm{miss}}$. The high $E_{\mathrm{T}}^{\mathrm{miss}}$ selection rejects most of the SM background processes and the value 250 GeV is also chosen such that the selected events are at the efficiency plateau of the $E_{\mathrm{T}}^{\mathrm{miss}}$ triggers (described in Section 3.2). This makes it easier to control the modeling of triggers in MC simulation, and in fact the trigger efficiencies are measured to be close to 1, hence no extra corrections for the modeling of triggers are applied to MC.

The distributions of $E_{\mathrm{T}}^{\mathrm{miss}}$ for some example signal models and the SM background

processes after the baseline selections are shown in Figure 3.2. The characteristic of signal events to have larger $E_{\mathrm{T}}^{\mathrm{miss}}$ in the tail of the distribution is further exploited by using exclusive $E_{\mathrm{T}}^{\mathrm{miss}}$ bins in the search regions.

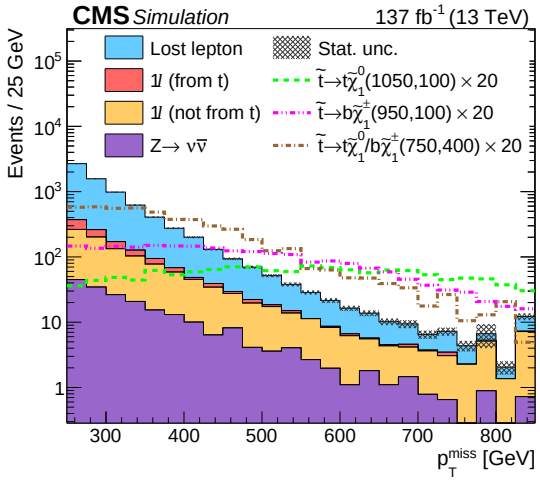

Figure 3.2: Distributions of $p_{\mathrm{T}}^{\mathrm{miss}}$ from the simulation are shown after applying the preselection requirements that are described in Section 3.3.3. The stacked histograms showing the SM background, whose categorizations are described in Section 2.3. The expectations for three example signal hypotheses are scaled up by 20 times and overlaid with the SM background, and the masses of the top squark and neutralino for the three hypotheses are listed in the parentheses of their legends, respectively. The last bin in each distribution includes the overflow events.

3.1.4.1 Mitigating noise in $E_{\mathrm{T}}^{\mathrm{miss}}$

Since the $E_{\mathrm{T}}^{\mathrm{miss}}$ of an event is not measured by one specifically designed subdetector but a combined effort from all subdetectors, it has a wide range of sources for noises. The noisy events, though in general are produced at a very low rate, would have an enhanced presentation in our analysis because we are triggering on $E_{\mathrm{T}}^{\mathrm{miss}}$.

The first obvious thing to do is to veto events that have an identifiable noise content. The following event filters are applied to our selected events to reject events with a high

chance of bad reconstructed $E_{\mathrm{T}}^{\mathrm{miss}}$.

- Beam halo filter
- Bad PF Muon Filter
- HBHE (isolation) noise filter
- Bad ECAL trigger primitive filter
- EE super cluster noise filter
- ECAL bad calibration filter (2017 & 2018 only)

Apart from occasionally noisy events, there is also a milder but persistent noise related to the ECAL Endcap in the year of 2017 and 2018, due to detector aging. This noise creates a large fake $E_{\mathrm{T}}^{\mathrm{miss}}$ component in an event that leads to a larger smearing effect to the overall $E_{\mathrm{T}}^{\mathrm{miss}}$. It has resulted in large discrepancy in the $E_{\mathrm{T}}^{\mathrm{miss}}$ distribution for moderate $E_{\mathrm{T}}^{\mathrm{miss}}$ between the observed data and MC simulation because it is not modeled well in the simulation. This issue is known to be particularly prominent in late 2017, namely the era E and F, for approximately $22.8\,\mathrm{fb}^{-1}$ of the data.

A special recipe to reconstruct $E_{\mathrm{T}}^{\mathrm{miss}}$ is employed for both observed data and MC modeling from 2017, in order to mitigate the difference between them, by fully dropping all jets and unclustered PF candidates with $2.65 < |\eta| < 3.139$ and $p_{\mathrm{T}} < 50\,\mathrm{GeV}$ in the PF $E_{\mathrm{T}}^{\mathrm{miss}}$ calculation. This modification creates larger (but consistent) $E_{\mathrm{T}}^{\mathrm{miss}}$ smearing in both data and MC, and increase the number of events with moderate $E_{\mathrm{T}}^{\mathrm{miss}}$ values

($100 < E_{\mathrm{T}}^{\mathrm{miss}} < 250\,\mathrm{GeV}$), but has a much smaller effect in the event count for our signal regions selections (with $E_{\mathrm{T}}^{\mathrm{miss}} > 250\,\mathrm{GeV}$), where the background is dominated by events with large genuine $E_{\mathrm{T}}^{\mathrm{miss}}$.

3.1.4.2 Resolution correction for the $E_{\mathrm{T}}^{\mathrm{miss}}$

The general smearing in the $E_{\mathrm{T}}^{\mathrm{miss}}$ is also called the $E_{\mathrm{T}}^{\mathrm{miss}}$ resolution. A good understanding of the modeling of $E_{\mathrm{T}}^{\mathrm{miss}}$ resolution is important in this analysis, especially for the estimation of the single lepton backgrounds. In this analysis, the rejection of the SM one lepton background relies on the M_{T} variable, which is more vulnerable to the effect from $E_{\mathrm{T}}^{\mathrm{miss}}$ resolution as it makes use of both the magnitude and the direction of the $\vec{p}_{\mathrm{T}}^{\,\mathrm{miss}}$ vector.

We have designed an *ad hoc* and data-driven method to further calibrate the modeling of $E_{\mathrm{T}}^{\mathrm{miss}}$ resolution in MC, where the $E_{\mathrm{T}}^{\mathrm{miss}}$ in every event from the simulation is corrected with Equation 3.1.

$$\vec{p}_{\mathrm{T,\,new}}^{\,\mathrm{miss}} = \left(\vec{p}_{\mathrm{T}}^{\,\mathrm{miss}} - \vec{p}_{\mathrm{T,\,true}}^{\,\mathrm{miss}}\right) \times \frac{\sigma_{i,j}^{\mathrm{data}}}{\sigma_{i,j}^{\mathrm{MC}}} + \vec{p}_{\mathrm{T,\,true}}^{\,\mathrm{miss}}, \tag{3.1}$$

Here the $\vec{p}_{\mathrm{T,\,true}}^{\,\mathrm{miss}}$ term is a sum of the 3-vectors of prompt neutrinos of the event, and the difference between it and the final reconstructed $E_{\mathrm{T}}^{\mathrm{miss}}$ is the part modeled by the simulation to mimic the detector resolution effect.

The parameters for the calibration, $\sigma_{i,j}^{\mathrm{data}}$ and σ_{i}^{MC}, are derived over a selected sample of γ+jets events from data and MC. Firstly, the γ+jets process has no genuine $E_{\mathrm{T}}^{\mathrm{miss}}$

in the event, and the energy of the photon generally well measured by the ECAL, so that any $E_{\mathrm{T}}^{\mathrm{miss}}$ in the event will result from $E_{\mathrm{T}}^{\mathrm{miss}}$ resolution, i.e. the mismeasurement of jets and other unclustered PF candidates. Secondly, the SM γ+jets process has a huge production cross section, and this means that with a simple selection asking for a high p_{T} photon in the event we can obtain a data sample with large statistics that is dominated by the γ+jets process.

The $E_{\mathrm{T}}^{\mathrm{miss}}$ from the γ+jets sample is projected onto the direction of the photon in the transverse plane, and the $E_{\mathrm{T}}^{\mathrm{miss}}$ component perpendicular to the photon, $E_{\mathrm{T},\perp}^{\mathrm{miss}}$, is taken to be the good measure of $E_{\mathrm{T}}^{\mathrm{miss}}$ due to the resolution effect. The distribution of $E_{\mathrm{T},\perp}^{\mathrm{miss}}$ are plotted for MC simulation of the 3 years and for different eras of each year in observed data, and is fitted separately, each time with a sum of 3 Gaussian distributions. The width parameters of the Gaussian distributions are hence taken as the parameters for calibration.

For each event in the MC, the $E_{\mathrm{T}}^{\mathrm{miss}}$ component result from the resolution effect is scaled by the ratio between 2 of these Gaussian width parameters $\sigma_{i,j}^{\mathrm{data}}$ and σ_{i}^{MC}, that are chosen based on 2 random numbers. The first random number selects the i^{th} ($i \leq 3$) Gaussian from the fit to the $E_{\mathrm{T}}^{\mathrm{miss}}$ distribution, and the second random number selects the j^{th} era (running period) of the data of a year. The final ratios between $\sigma_{i,j}^{\mathrm{data}}$ and σ_{i}^{MC} are around 1.1 for the 2018 data and are up to 1.15 for the last 2 eras of the 2017 data.

We verified this calibration in a $E_{\mathrm{T}}^{\mathrm{miss}}$ sideband from our baseline selections and the M_{T} distributions in this sideband region before and after applying the $E_{\mathrm{T}}^{\mathrm{miss}}$ resolution

correction are shown in Figure 3.3, separately for the 2017 and 2018 data and MC. The results from 2016 are not shown because the calibration factors are small and the data/MC agreement is already good before applying the $E_{\mathrm{T}}^{\mathrm{miss}}$ resolution correction. The top row of the figure shows that there were clear excess of events from the observed data in the range between $100 < M_{\mathrm{T}} < 180\,\mathrm{GeV}$, result from the $E_{\mathrm{T}}^{\mathrm{miss}}$ resolution effect that are unaccounted for in the simulation. We may also identify that this excess is mainly coming from the $\mathrm{t\bar{t}} \to 1\ell$ contributions, in the regions where the M_{T} distribution is experiencing a drop-off due to the W mass constraint. Such effect disappears after the $E_{\mathrm{T}}^{\mathrm{miss}}$ resolution correction is applied to the simulation (see the bottom row of the figure), and no overcorrection is seen in high M_{T}, where the $\mathrm{t\bar{t}} \to 2\ell$ process dominates.

3.2 Triggers

There are hundreds of HLT paths used by the CMS to record events, to satisfy the need for different analysis. Events are grouped into different data sets under the type of trigger they have fired, and overlap is allowed when an event fires different types of the trigger at the same time. We will be explicitly asking data events to pass a certain set of triggers, since we want to have a controllable trigger condition with efficiency that can be measured. The selection of triggers covers most of the desired events for this analysis that are recorded. The desired events feeds into the design of the triggers before the LHC is turned on.

The events of the search regions are selected by a combination of `MET_MHT` and single

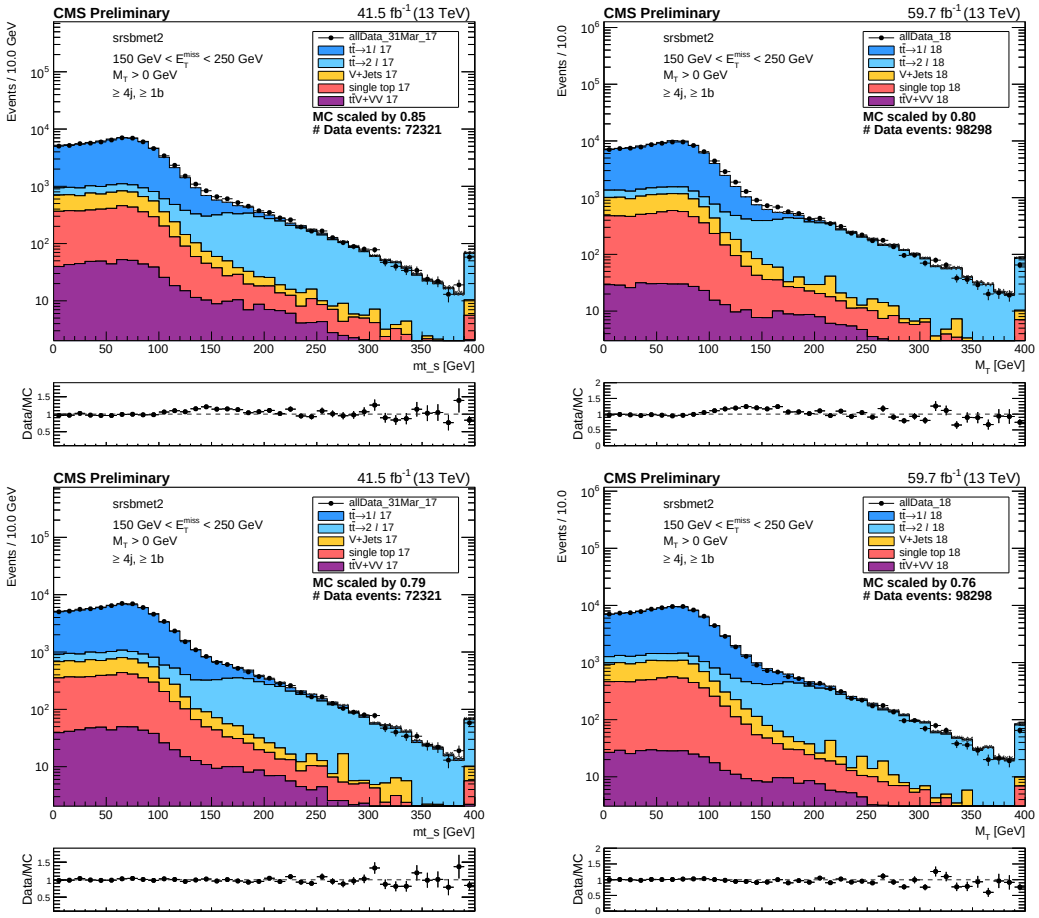

Figure 3.3: Distribution of M_{T} in the $E_{\mathrm{T}}^{\mathrm{miss}}$ sideband ($150 < E_{\mathrm{T}}^{\mathrm{miss}} < 250\,\mathrm{GeV}$) after the baseline selection described in Section 3.3.3, for the observed data and MC simulations for the SM backgrounds for 2017 (left column) and 2018 (right column), before applying the $E_{\mathrm{T}}^{\mathrm{miss}}$ resolution smearing (top row) and after (bottom row). The simulation is scaled to fit the normalization of the observed data, and the scale factors are shown in plots.

lepton triggers, as described in Table 3.3, 3.4 and 3.5 for the data taking periods for 2016, 2017 and 2018, respectively. The names of the triggers are mostly self-explaining for their requirements, while the objects are raw objects before corrections or selections are applied. The real efficiencies of these triggers are hence not a step function after the value in their name, but more like an error function with "turn-on" and eventually reaching the efficiency plateau at a higher value than the trigger selection.

The search only focuses on events with a $E_{\mathrm{T}}^{\mathrm{miss}}$ of at least 250 GeV, which means the `MET_MHT` triggers are expected to be almost fully efficient in the search regions. Using the union of the `MET_MHT` and single lepton triggers recovers the small inefficiency for events with lower $E_{\mathrm{T}}^{\mathrm{miss}}$ values before reaching the efficiency plateau of the `MET_MHT` triggers.

Table 3.3: HLT trigger paths used for 2016 data. Events in the search regions are required to fire at least one trigger in the list of MET, `MET_MHT` and single lepton triggers. The list also contain triggers that may be prescaled for some periods.

Type	HLT path
SingleMuon	`HLT_Iso(Tk)Mu22`, `HLT_Iso(Tk)Mu24`
SingleElectron	`HLT_Ele25_eta2p1_WPTight_Gsf`, `HLT_Ele27_eta2p1_WPTight_Gsf`
MET_MHT	`HLT_PFMET(NoMu)110_PFMHT(NoMu)110_IDTight`, `HLT_PFMET(NoMu)120_PFMHT(NoMu)120_IDTight`
MET	`HLT_PFMET170_NoiseCleaned`, `HLT_PFMET170_JetIdCleaned`, `HLT_PFMET170_HBHECleaned`, `HLT_PFMET170_NotCleaned`

Table 3.4: HLT trigger paths used for 2017 data. Events in the search regions are require to fire at least one trigger in the list of `MET_MHT` and single lepton triggers. The list also contain triggers that may be prescaled for some periods.

Type	HLT path
SingleMuon	`HLT_IsoMu24`, `HLT_IsoMu27`
SingleElectron	`HLT_Ele35_WPTight_Gsf`, `HLT_Ele32_WPTight_Gsf`
MET_MHT	`HLT_PFMET(NoMu)120_PFMHT(NoMu)120_IDTight`, `HLT_PFMET120_PFMHT120_IDTight_PFHT60`, `HLT_PFMET100_PFMHT100_IDTight_PFHT60`

Table 3.5: HLT trigger paths used for 2018 data. Events in the search regions are require to fire at least one trigger in the list of MET_MHT and single lepton triggers. The list also contain triggers that may be prescaled for some periods.

Type	HLT path
SingleMuon	HLT_IsoMu24, HLT_IsoMu27
SingleElectron	HLT_Ele35_WPTight_Gsf, HLT_Ele32_WPTight_Gsf
MET_MHT	HLT_PFMET(NoMu)120_PFMHT(NoMu)120_IDTight, HLT_PFMET120_PFMHT120_IDTight_PFHT60

3.2.1 Measurement of the trigger efficiencies

The efficiency of the trigger set is measured using a orthogonal trigger method, using events that are included in a different data set but have the desired triggering objects as the denominator.

For this analysis, we use the events from the JetHT data set that pass a combination of HLT_PFHT triggers and HLT_AK8PFJet triggers. The events used for the denominator are required to pass an inclusive selection with at least one lepton satisfying the *selection* criteria and at least two jets. The efficiency of the SR trigger set can be calculated by asking whether these events pass any trigger in the SR trigger set. The result is shown in Figs. 3.4, separately for the 3 years of data taking and the flavor of the leading p_{T} lepton, and as a function of $E_{\mathrm{T}}^{\mathrm{miss}}$ and the p_{T} of the leading lepton. The general trigger efficiency for the data data is over 98% for our signal region definition ($E_{\mathrm{T}}^{\mathrm{miss}} > 250\,\mathrm{GeV}$ and $p_{\mathrm{T}}^{\ell} > 20\,\mathrm{GeV}$). Given the comparatively large statistical error in this result, we do not correct for the trigger efficiency in the simulation but include a 2% systematic uncertainty for the backgrounds that are estimated from the simulation directly.

For events entering the dilepton control region, not all of them would necessarily

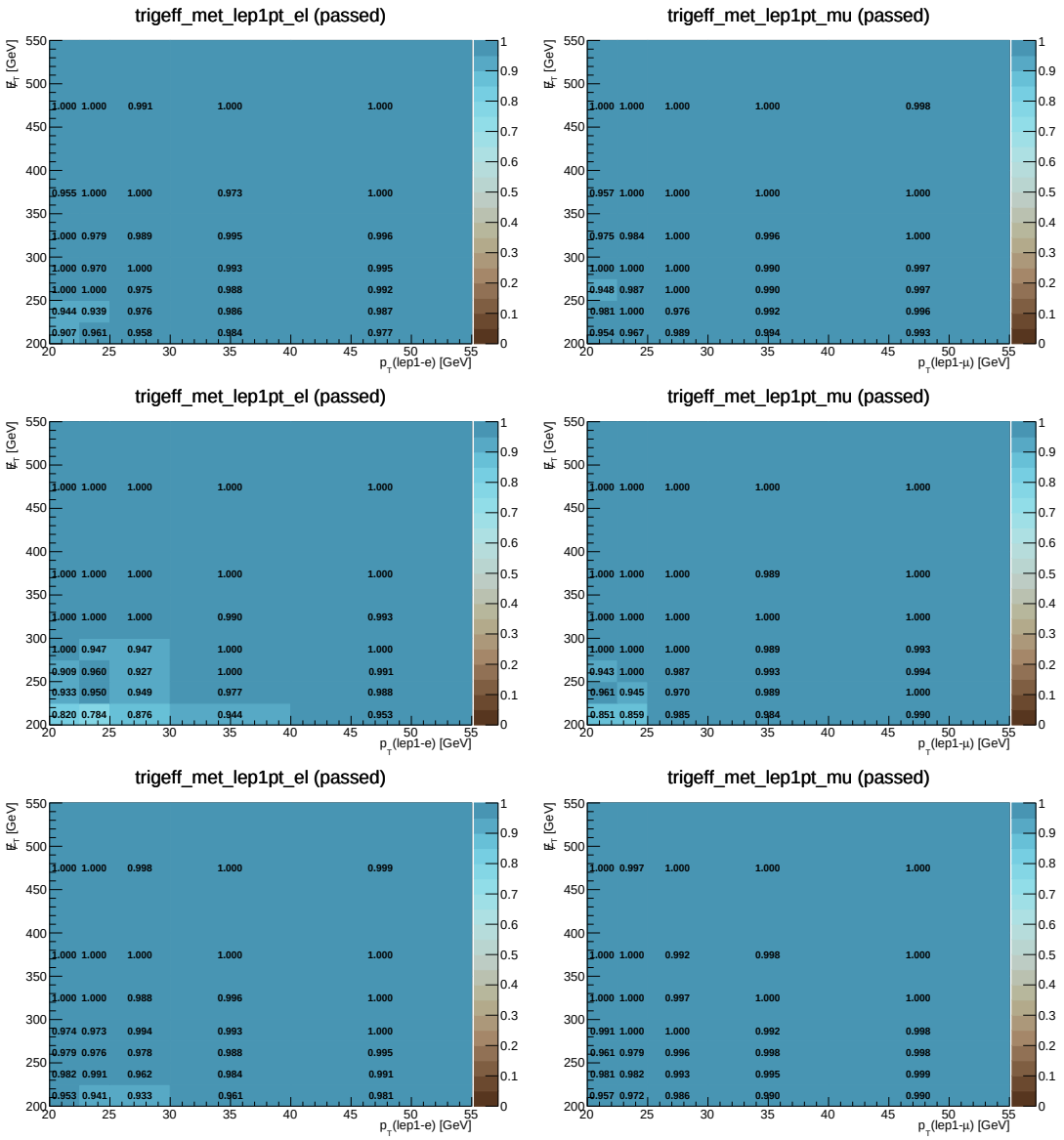

Figure 3.4: Trigger efficiency measurement for the union of the MET, `MET_MHT` and single lepton triggers as a function of $E_{\mathrm{T}}^{\mathrm{miss}}$ and lepton-p_{T} for the 2016 (top row), 2017 (middle row) and 2018 (bottom row) pp collision data set, divided further by the leading lepton flavor is electron (left column) or muon (right column). The exact trigger paths are listed in Table 3.3, 3.4 and 3.5. The color palette presents the measured efficiency.

satisfy $E_{\mathrm{T}}^{\mathrm{miss}} > 250\,\mathrm{GeV}$ requirement, since the CR selection is based on the "removed-lepton $E_{\mathrm{T}}^{\mathrm{miss}}$" (see Section 4.1 for detail), which is the magnitude of the vector sum of

$\vec{p}_{\mathrm{T}}^{\,\mathrm{miss}}$ and the 4-vector of the second lepton. We select this data set with the same trigger set as the one used for the signal regions, but we do perform a separate measurement of the trigger efficiencies as a function of the removed-lepton $E_{\mathrm{T}}^{\mathrm{miss}}$ and the leading lepton p_{T}, over the events one *selection* lepton and one *trailing* lepton and at least two jets. The trigger efficiencies for these dilepton events are shown in Figure 3.5. It can be seen that the trigger efficiencies can reach as low as 70% for events with low lepton-p_{T} or low removed-lepton $E_{\mathrm{T}}^{\mathrm{miss}}$, while the large fluctuation results from the low statistics of the qualified dilepton events in the JetHT data set. We will assign these measured efficiencies as reweighting factors for the corresponding $\mathrm{t\bar{t}}$+jets simulation events in the dilepton control region, and the uncertainties of the trigger efficiency measurement as the uncertainty on the reweighting factors. The final impact from the events with lower trigger efficiencies is not very large, and the possibility of the inclusion of dilepton triggers had been investigated but is not adopted as it does not seem to significantly increase the number of accepted events in the control regions.

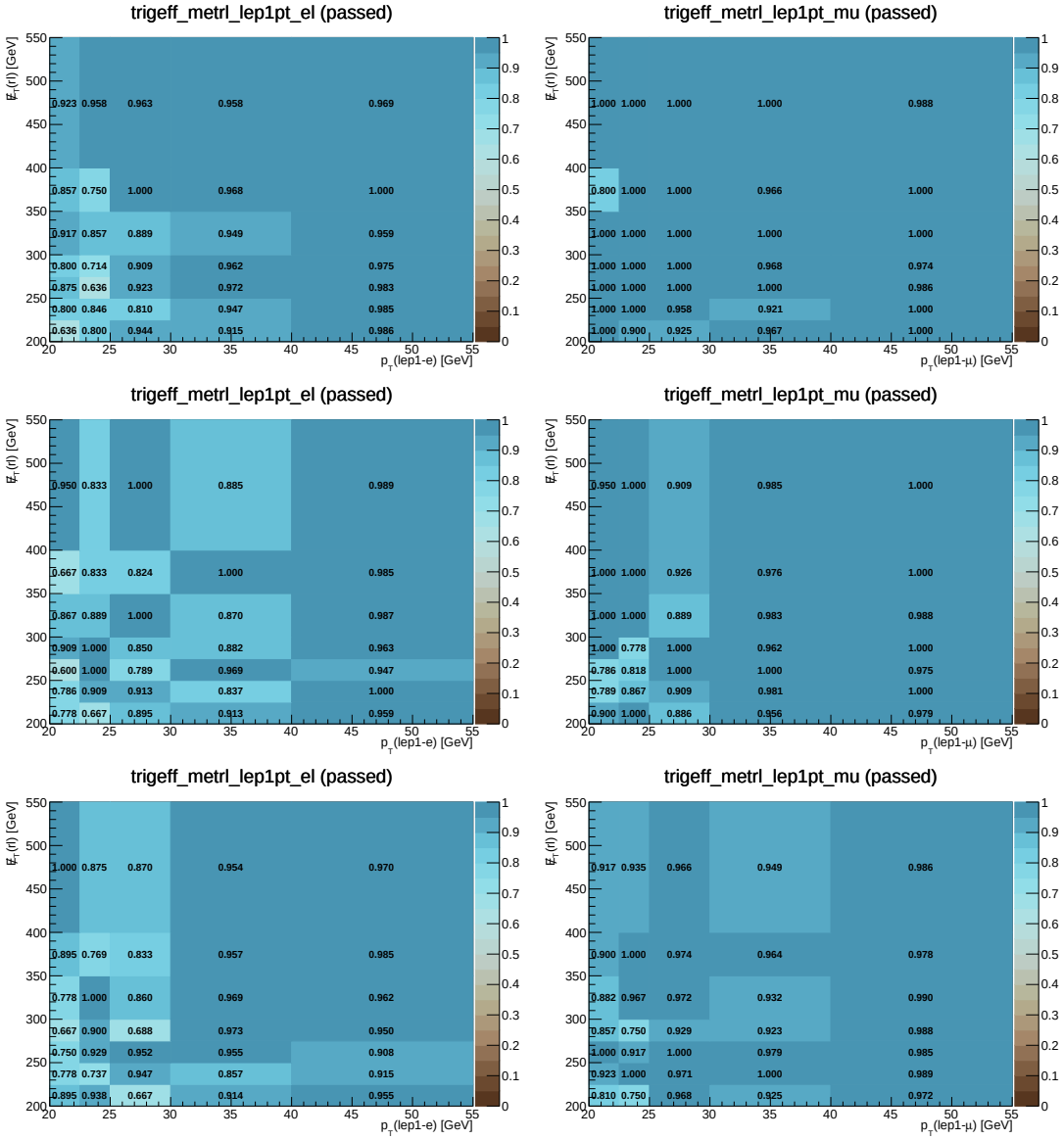

Figure 3.5: Trigger efficiency measurement for the dilepton control region for the union of the `MET_MHT` and single lepton triggers as a function of removed-lepton $E_{\mathrm{T}}^{\mathrm{miss}}$ and lepton-p_{T} for the 2016 (top row), 2017 (middle row) and 2018 (bottom row) pp collision data set, divided further by the leading lepton flavor is electron (left column) or muon (right column). The exact trigger paths are the same as those used for the signal region selections, and are listed in Table 3.3, 3.4 and 3.5. The color palette presents the measured efficiency.

3.3 Event selections

3.3.1 Kinematic variables

3.3.1.1 The transverse mass M_{T} between the ℓ and $E_{\mathrm{T}}^{\mathrm{miss}}$

As already partly discussed in Section 2.3, a high M_{T} requirement to suppress the SM single lepton backgrounds is one of the core feature of this analysis. If the event has a single $\mathrm{W} \to \ell\nu$ decay and has little additional source of $E_{\mathrm{T}}^{\mathrm{miss}}$ (i.e. the neutrino is the main component of $E_{\mathrm{T}}^{\mathrm{miss}}$) in the event, then the M_{T} would mostly be less than m_{W} (80.2 GeV). As can be seen in Figure 3.6, a strong drop-off above this mass is observed. In this analysis, we require $M_{\mathrm{T}} > 150\,\mathrm{GeV}$, to account for the left-over tails that can come from off-shell Ws or detector resolution effects. Since the 1ℓ (from t) background has the extra mass constraints from m_{t}, the left-over contribution from this background is mostly coming from the extra fake $E_{\mathrm{T}}^{\mathrm{miss}}$ from mismeasurement, hence an understanding of the modeling of $E_{\mathrm{T}}^{\mathrm{miss}}$ in simulation can be important for this background.

3.3.1.2 The $\min \Delta\phi(j_{1,2}, \vec{p}_{\mathrm{T}}^{\mathrm{miss}})$ variable

The selection on $\min \Delta\phi(j_{1,2}, \vec{p}_{\mathrm{T}}^{\mathrm{miss}})$, defined as the smaller one of the $\Delta\phi$ between the $E_{\mathrm{T}}^{\mathrm{miss}}$ and the 2 leading p_{T} jets, is put in place to control the background with large fake $E_{\mathrm{T}}^{\mathrm{miss}}$ from jet mismeasurement. When a jet is mismeasured, most of time it is under-measured when some part of the jet is not detected. If the total $E_{\mathrm{T}}^{\mathrm{miss}}$ component is driven by this mismeasurement, the final $\vec{p}_{\mathrm{T}}^{\mathrm{miss}}$ is likely to point at the mismeasured

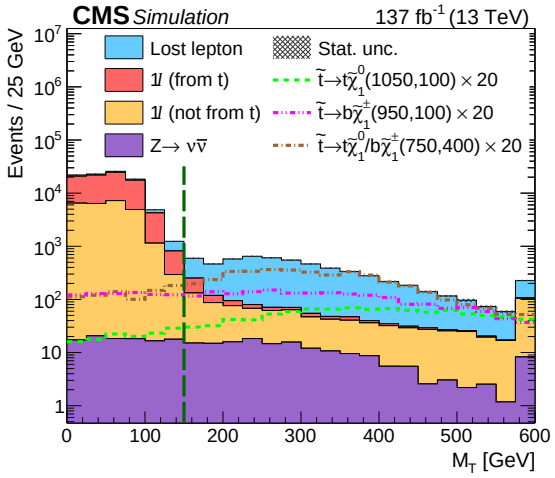

Figure 3.6: Distributions of M_{T} from the simulation are shown after applying the preselection requirements that are described in Section 3.3.3, except for the M_{T} requirement itself. The stacked histograms showing the SM background, whose categorizations are described in Section 2.3. The expectations for three example signal hypotheses are scaled up by 20 times and overlaid with the SM background, and the masses of the top squark and neutralino for the three hypotheses are listed in the parentheses of their legends, respectively. The last bin in each distribution includes the overflow events.

jet. While a ΔR cannot be constructed because of the $\vec{p}_{\mathrm{T}}^{\,\mathrm{miss}}$, we impose a requirement on $\Delta\phi$ in the $x-y$ plane between this jet and $\vec{p}_{\mathrm{T}}^{\,\mathrm{miss}}$ to reduce such background.

As mentioned above, fake $E_{\mathrm{T}}^{\mathrm{miss}}$ components from jet mismeasurement can make itself more problematic by helping events escape the M_{T} requirement, and this effect can be visible in Figure 3.7, where all baseline selections are applied except the $\min\Delta\phi(j_{1,2},\vec{p}_{\mathrm{T}}^{\,\mathrm{miss}})$ itself. The $\min\Delta\phi(j_{1,2},\vec{p}_{\mathrm{T}}^{\,\mathrm{miss}})$ requirement can be especially effective in rejecting the 1ℓ backgrounds, where the source of real $E_{\mathrm{T}}^{\mathrm{miss}}$ is only one neutrino. It is a bit less effective for the lost lepton background, where the source of $E_{\mathrm{T}}^{\mathrm{miss}}$ is more complicated, and the distribution for the irreducible $\mathrm{Z}\to\nu\bar{\nu}$ background follows basically the same trend as for the signal models.

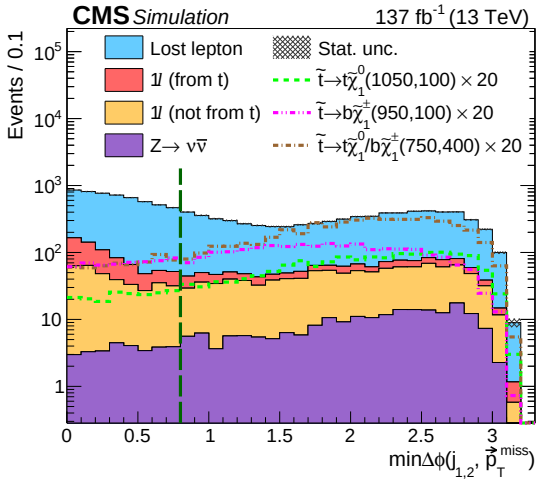

Figure 3.7: Distribution of $\min \Delta\phi(j_{1,2}, \vec{p}_{\mathrm{T}}^{\mathrm{miss}})$ after the baseline selection, except for the for the main backgrounds and various signal models. The SM contributions shown in stacked histogram overlaid by some example signal points shown in dotted lines. The signals are scaled up by 20 times in order to easily compare the shapes. The green dashed vertical line indicate the selection point at 0.8 and only the right hand side of the line are selected by the baseline selection.

3.3.2 Additional selections and corrections

Pile-up reweighting

The pile-up weights are a set of scale factors applied on events from the MC simulation based on the number of true vertices of the event. The reason that such weights are necessary is that the generation of simulated samples usually start before the actual data taking finishes, and so the pile-up condition for the actual data taken can be different from the one that MC samples were generated with. The pile-up profile for observed data is taken from a minimum bias sample, and the ratio between it and the pile-up profile used in MC generation is used to generate the pile-up weights. The weights are determined on a year to year basis, and are generally much smaller than 1 (MC over predicting the

fractions) for events with a high number (>50) of primary vertices. Uncertainties from the measurement in data lead to a shift in the number of vertices distribution, and the uncertainties for the pile-up weights vary the weights accordingly to match this shift in the data distribution.

L1 prefiring weights

The ECAL L1 prefiring is an issue with data taking during the late 2016 and the whole 2017 data set, where interesting events could be falsely blocked from triggering and not recorded by the detector. The cause is traced to distorted pulse shape in ECAL due to detector aging, that results in the association of e/γ objects with the previous bunch crossing, triggering the previous bunch crossing and eventually causing the event to veto itself as the L1 trigger rules forbid consecutive trigger firing.

As there's no way to recover the lost events, we can only correct the MC modeling of such effect by applying the estimated non-prefiring probability as event weights to 2016 and 2017 MC samples, for both the signal and background. Fortunately, the overall effective loss is found to be about 2–5% in our signal regions, with even less effect in higher $E_{\mathrm{T}}^{\mathrm{miss}}$. Similar fraction of loss in background and signal were found.

HT5/HT for EE noise mitigation

It had been discussed in Section 3.1.4 that the EE noise due to detector aging had been creating large fake $E_{\mathrm{T}}^{\mathrm{miss}}$ in events and hence letting in extra backgrounds into our signal regions in the year of 2017 and 2018. As an extra measure to minimize the issue,

we employ an extra requirement of $H_{\mathrm{T}}^{5}/H_{\mathrm{T}} < 1.5$ in the analysis for observed events recorded in the year 2017 and 2018 as well as the corresponding MC simulation for them.

The H_{T} is a measure of the hadronic activity, defined as the scalar sum of the p_{T} of all the jets of $p_{\mathrm{T}} > 30\,\mathrm{GeV}$ and within $|\eta| < 2.4$, while the H_{T}^{5} is calculated with all such jets but within $|\eta| < 5.0$. The jets that are considered are also required to pass the tight jet ID and are not overlapping with the selected or trailing (veto) lepton, and the p_{T} value used are after the jet energy correction. From their definitions, we see that H_{T} only considers jets that are within the coverage of the tracker system, while H_{T}^{5} considers also the jets in EE that are outside the tracker coverage ($2.5 < |\eta| < 3.0$), which are more susceptible to the EE noise problem both because of the lack of tracker information, but also because of worse detector aging from radiation. Hence, the difference between $H_{\mathrm{T}}^{5}/H_{\mathrm{T}}$ ratio and 1 can be considered as a measure for the portion of the measured hadronic activities in the event that could be more susceptible to the EE noise, and by keeping this ratio lower than 1.5 we limit our selection to events that tend to have better measured $E_{\mathrm{T}}^{\mathrm{miss}}$.

The impact of this extra requirement on the signal and background yields in our signal regions have also been assessed, and the results show that the overall effect is very small, causing at most 5% loss in some of the signal regions.

Event veto for HEM 15/16 failure in 2018

Starting from era C of the 2018 data taking, the HCAL Endcap lost 2 sections of its detector, namely the HEM 15/16 due to power issues. This results in bad energy

measurements for jets that fall in this region and can also cause misidentification of electrons due to the absence of hadronic energy measurement. The impact can be visible as a large excess of electrons (with basic *veto* ID) in the affected η-ϕ region around $\eta < -1.4$ and $-1.6 < \phi < -0.8$. This can creates extra background for the dilepton control region with the extra fake electron, or bring fake $E_{\mathrm{T}}^{\mathrm{miss}}$ into the event from the under-measurement of the jet energy. The effect is evaluated by comparing the M_{T} distribution for events with jet falling in the HEM 15/16 region against events with jet falling in the opposite η-ϕ region, and a clear excess can be seen near the W mass edge.

The adopted strategy is to veto the event if any trailing electron or lepton-cleaned jet with $p_{\mathrm{T}} > 30\,\mathrm{GeV}$ falls in the affected region, defined by $\eta < -1.4$ and $-1.6 < \phi < -0.8$. The overall effect on signal yield is found to be very small and does not affect the search sensitivity.

3.3.3 Summary on the event preselection

As a summary for the all the selection cuts from above, we determine the baseline selection for the standard search regions as below:

- One and only one good lepton with $p_{\mathrm{T}}^{\ell} > 25\,\mathrm{GeV}$, with $|\eta^{\mu}| < 2.4$ and $|\eta^{\mathrm{e}}| < 1.442$
- No extra lepton with $p_{\mathrm{T}}^{\ell} > 5\,\mathrm{GeV}$ and $\left|\eta^{\ell}\right| < 2.4$
- No isolated track with $p_{\mathrm{T}}^{\mathrm{trk}} > 10\,\mathrm{GeV}$ and $\left|\eta^{\mathrm{trk}}\right| < 2.4$ other than the selected lepton
- No hadronic τ with $p_{\mathrm{T}}^{\tau} > 20\,\mathrm{GeV}$ and $|\eta^{\tau}| < 2.3$

- $N_{\mathrm{j}} \geq 2$ for jets with $p_{\mathrm{T}} > 30\,\mathrm{GeV}$ and $|\eta| < 2.4$
- $N_{\mathrm{b}} \geq 1$ for DeepCSV medium working point over the selected jets
- $E_{\mathrm{T}}^{\mathrm{miss}} > 250\,\mathrm{GeV}$
- $M_{\mathrm{T}} > 150\,\mathrm{GeV}$
- $\min \Delta\phi(j_{1,2}, \vec{p}_{\mathrm{T}}^{\mathrm{miss}}) > 0.8$

and with addition of the following selections are applied to the partial data set for rejecting possible noises from detector issues:

- $H_{\mathrm{T}}^{5}/H_{\mathrm{T}} < 1.5$ for all events taken in 2017 and 2018 (a total of $101.2\,\mathrm{fb}^{-1}$)
- No electron (*veto* ID) or jet ($p_{\mathrm{T}} > 30\,\mathrm{GeV}$) at $\eta < -1.4$ and $-1.6 < \phi < -0.8$, for run number greater or equal to 319077 (approximately $38\,\mathrm{fb}^{-1}$)

One note should be given that while the N_{j} requirement is only 2, only a small subset of events from the 2–3 jet are selected, and the focus of the analysis is still at $N_{\mathrm{j}} \geq 4$. The count for the number of b-tagged jet, N_{b}, is also included in the count of N_{j}.

3.3.4 Dedicated search regions for the top and W corridor

We are referring a section of the phase space of the T2bt type signals as the "corridor" regions where the mass difference between $m_{\tilde{\mathrm{t}}}$ and $m_{\tilde{\chi}_1^0}$, $\Delta M(\tilde{\mathrm{t}}, \tilde{\chi}_1^0)$, is close to m_{t} or $(m_{\mathrm{W}} + m_{\mathrm{b}})$, namely the top corridor for $150\,\mathrm{GeV} < \Delta M(\tilde{\mathrm{t}}, \tilde{\chi}_1^0) \leq 220\,\mathrm{GeV}$ and W corridor

for $\Delta M(\tilde{\mathrm{t}}, \tilde{\chi}_1^0) \leq 150\,\mathrm{GeV}$. The signal scenarios considered in this analysis, the lower bound for the $\Delta M(\tilde{\mathrm{t}}, \tilde{\chi}_1^0)$ is 87.5 GeV.

When $\Delta M(\tilde{\mathrm{t}}, \tilde{\chi}_1^0) \sim m_{\mathrm{t}}$, the top quark and the $\tilde{\chi}_1^0$ are produced approximately at rest in the rest frame of the $\tilde{\mathrm{t}}$. In this case, both the top quark and the $\tilde{\chi}_1^0$ will inherit the initial boost of the $\tilde{\mathrm{t}}$, which would be back-to-back from each other if no extra ISR/FSR are involved. This will result in small $E_{\mathrm{T}}^{\mathrm{miss}}$ since the $\tilde{\chi}_1^0$s that carry most of the invisible energy are back-to-back and cancel each other in the transverse plane. The key for finding this type of signal topology would be to target the subset of their production in which the $\tilde{\mathrm{t}}\bar{\tilde{\mathrm{t}}}$ pair are receiving non-trivial initial boost from the ISR jets that are produced in association with the $\tilde{\mathrm{t}}\bar{\tilde{\mathrm{t}}}$. In fact, the $E_{\mathrm{T}}^{\mathrm{miss}} > 250\,\mathrm{GeV}$ requirement from the preselection would already serve as selecting ISR boosted events for signals in these topology, and the standard search regions do still retain decent sensitivity for these signals, even though the sensitivity can be considerably smaller than those signals with similar production cross section but with larger $\Delta M(\tilde{\mathrm{t}}, \tilde{\chi}_1^0)$.

The question is whether we can do better in the search for stop signals in the corridor regions by focusing more on the feature of it being an ISR boosted system. The first obvious thing is to explicitly ask for at least one extra high-p_{T} jet in the event, by raising the requirement on number of jets to 5. No extra p_{T} requirement are placed for the jets, as from previous studies, it was realized that the $E_{\mathrm{T}}^{\mathrm{miss}} > 250\,\mathrm{GeV}$ requirement is already enough by itself as the high-p_{T} requirement, and asking the ISR jet to be above some threshold reduces the overall signal acceptance without bringing significantly improve-

ment to the signal to background discrimination. Instead, it is found that requiring the highest-p_{T} jet to be a non b-tagged jet (DeepCSV *medium* WP) improves the signal to background discrimination power, by increasing the probability that this leading jet is an ISR jet instead of the b jet from top decay.

The next tuning would be on the requirement of $\min \Delta\phi(j_{1,2}, \vec{p}_{\mathrm{T}}^{\,\mathrm{miss}})$, which is still necessary for rejecting backgrounds from jet mismeasurement, but can be relaxed a bit to improve acceptance of the signal, since the subleading jet in the boosted scenarios are more likely to be coming from the top quark decay and be more aligned with the $E_{\mathrm{T}}^{\mathrm{miss}}$ that arises mostly by the $\tilde{\chi}_1^0$s and neutrinos.

From a similar argument, we expect the lepton to be also close to the $E_{\mathrm{T}}^{\mathrm{miss}}$ in this case, and this feature can be exploited by the variable $\Delta\phi(\ell, \vec{p}_{\mathrm{T}}^{\,\mathrm{miss}})$ defined as the angle between the selected lepton and the $E_{\mathrm{T}}^{\mathrm{miss}}$ in the transverse plane. Apart from the direction of the lepton, it is noticed that p_{T} of the lepton is usually not very high for the targeted signal, while the backgrounds tend to have higher portion events with high-p_{T} leptons. Hence, an upper limit on the p_{T} of the selected lepton could also be helpful. Further studies were performed and showed that, for leptons $p_{\mathrm{T}} > 50\,\mathrm{GeV}$, a running upper limit based on the $\Delta\phi(\ell, \vec{p}_{\mathrm{T}}^{\,\mathrm{miss}})$ can be better at keeping the sensitivity for the signal as well as rejecting the background. The balance point is found at $(250 - 100 \times \Delta\phi(\ell, \vec{p}_{\mathrm{T}}^{\,\mathrm{miss}}))\,\mathrm{GeV}$, to have a maximum upper limit $250\,\mathrm{GeV}$ when lepton and $E_{\mathrm{T}}^{\mathrm{miss}}$ are closer with each other, or enforcing $\Delta\phi(\ell, \vec{p}_{\mathrm{T}}^{\,\mathrm{miss}}) < 2.5$ for leptons with $p_{\mathrm{T}} > 50\,\mathrm{GeV}$.

For the dedicated top and W corridor search regions, though most of the preselection

criteria standard search regions still holds, they are not a strict subset of the baseline selections listed above. For both dedicated search regions, we are relaxing the requirement on

- $\min \Delta\phi(j_{1,2}, \vec{p}_{\mathrm{T}}^{\,\mathrm{miss}}) \geq 0.5$ (instead of 0.8)

Additionally, the following conditions are added to both dedicated corridor search regions:

- $p_{\mathrm{T}}^{\ell} < \max\left[50, \left(250 - 100 \times \Delta\phi(\ell, \vec{p}_{\mathrm{T}}^{\,\mathrm{miss}})\right)\right]$ GeV
- Leading jet in p_{T} is not b-tagged (DeepCSV medium working point)

When $\Delta M(\tilde{\mathrm{t}}, \tilde{\chi}_1^0) < m_{\mathrm{t}}$ and get close to m_{W}, a large fraction of the b quarks can be produced with very little boost and hence may be very soft and under the threshold 30 GeV for our normal jet selections, but still give rise to displaced vertices. The soft b tags are specially designed to target these type of b quarks in the event, and the number of soft b objects ($N_{\mathrm{b,\ soft}}$) will be used instead of the number of b-tagged jets based on DeepCSV scores (also labeled as $N_{\mathrm{b,\ med}}$ for the purpose of disambiguation with the soft b objects).

Because the soft b objects are orthogonal to the jet collection, the N_{b} requirement in the baseline criteria is interpreted as

- $N_{\mathrm{b,\ soft}} \geq 1$ (instead of $N_{\mathrm{b,\ med}}$)

specifically for the dedicated W corridor search region. The requirement on the N_{j} counting for the W corridor search is also lowered to 3 to accommodate the soft b that are considered "lost" to the definition of jets.

Figure 3.8 shows the $N-1$ distributions for the number of jets, p_{T} of the selected lepton and the $\Delta\phi(\ell, \vec{p}_{\mathrm{T}}^{\,\mathrm{miss}})$ for the dedicated selections for top corridor and W corridor searches described above, respectively. Two example signals, T2tt(450, 275) and T2tt(425, 328), are shown on top of the SM backgrounds. The numbers in the parenthesis refer to $m_{\tilde{\mathrm{t}}}$ and $m_{\tilde{\chi}_1^0}$ in units of GeV, and they fall into the categories of top and W corridor, respectively. The lines for the two signal points are also scaled up by 5 times to allow a better comparison in shape with the SM backgrounds.

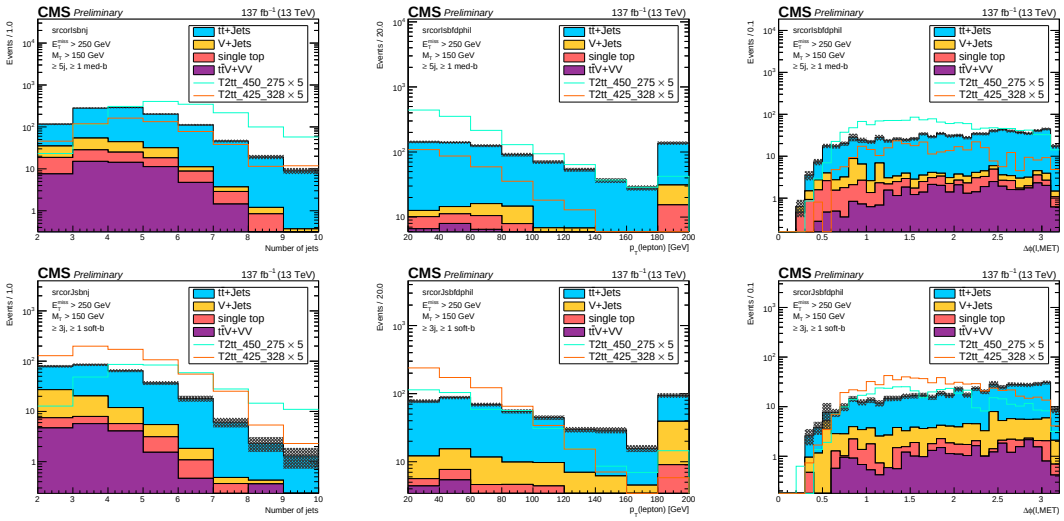

Figure 3.8: The $N-1$ distributions for the number of jets (left column), p_{T} of the selected lepton (middle column) and $\Delta\phi(\ell, \vec{p}_{\mathrm{T}}^{\,\mathrm{miss}})$ (right column) for the dedicated top corridor (upper row) and W corridor (bottom row) searches. The SM backgrounds are shown in stacked histogram, and 2 example signal points, T2tt(450, 275) and T2tt(425, 38), with the numbers in the parenthesis refers to $m_{\tilde{\mathrm{t}}}$ and $m_{\tilde{\chi}_1^0}$ in the unit of GeV, are shown on top with their expected yields scaled up by 5 times to show a better shape comparison with the SM background. They fall into the categories of top and W corridor, respectively.

3.4 Signal region categorizations

3.4.1 Kinematic variables for binning

3.4.1.1 Modified topness: t_{mod}

The topness variable [59] was developed as a way to find dileptonic $\mathrm{t\bar{t}}$ decays with a missing lepton contributing to the $E_{\mathrm{T}}^{\mathrm{miss}}$. It exploits 4 constraints on the masses of the dilepton system, one on the constraint of the W mass, 2 on the top masses, and 1 on the center of mass. During the investigation of this variable based on our search scenarios, it was found that removing some of the terms would help in the overall signal discrimination power. Dropping those terms lead to the development of modified topness (t_{mod}), formally defined as

$$t_{\mathrm{mod}} = \ln(\min S), \text{ with } S = \frac{\left(m_{\mathrm{W}}^2 - (p_\nu + p_\ell)^2\right)^2}{a_{\mathrm{W}}^4} + \frac{\left(m_{\mathrm{t}}^2 - (p_{\mathrm{b}} + p_{\mathrm{W}})^2\right)^2}{a_{\mathrm{t}}^4} \tag{3.2}$$

with $a_{\mathrm{W}} = 5\,\mathrm{GeV}$ and $a_{\mathrm{t}} = 15\,\mathrm{GeV}$ as resolution parameters.

Like the topness variable, the t_{mod} is a χ^2-like variable which tries to evaluate how likely the event is consistent with the hypothesis of dileptonic $\mathrm{t\bar{t}}$ decay with missing lepton. The first term in its definition corresponds to the W boson mass constraint of top quark decay containing the reconstructed lepton, and the second term corresponds to the top quark mass of the top quark decay containing the missing lepton. The minimization of the variable S is done with respect to all three components of the three momentum $\vec{p}_{\mathrm{W}}$,

and the components of the three momentum $\vec{p}_\nu$ along the beam line with the constraints $\vec{p}_{\mathrm{T}}^{\,\mathrm{miss}} = \vec{p}_{\mathrm{T,W}} + \vec{p}_{\mathrm{T},\nu}$ and $p_{\mathrm{W}}^2 = m_{\mathrm{W}}^2$. The minimization is also done through the choice of p_{b}, which is chosen from up to three b-tagged jets with highest DeepCSV discriminator values. In cases of building t_{mod} for events in control regions that have no b-tagged jet, all possibilities with the highest 3 DeepCSV value jets are tried.

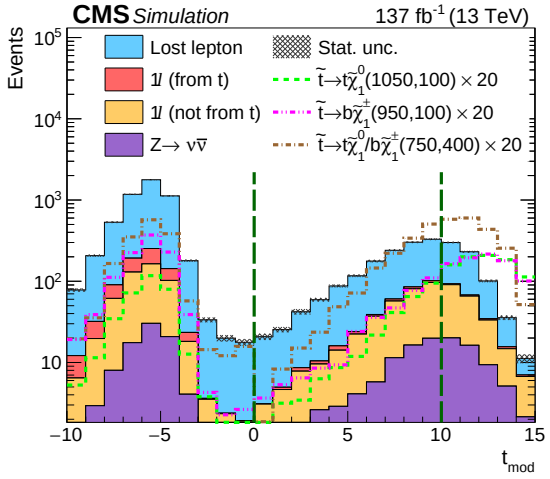

Figure 3.9: Distribution of t_{mod} after the baseline selection, for the main backgrounds and various signal models. The SM contributions shown in stacked histogram overlaid by some example signal points shown in dotted lines. The signals are scaled up by 20 times in order to easily compare the shapes. The green dashed vertical lines indicate the working points where we would use to make classification to the events in Section 3.4.

The distribution of t_{mod} for events passing the preselection is shown in Figure 3.9, with the SM contributions shown in stacked histogram overlaid by some example signal points shown in dotted lines. The signals are scaled up by 20 times in order to easily compare the shapes. It can be seen from the distribution that both the signal and the background show a double peak feature, with a large portion of the events contributing in the peak of $t_{\mathrm{mod}} < 10$, but the shapes of the signals are much more skewed towards higher

value, especially above 10. Another feature is the shape difference between the different signal scenarios, where the T2tt type tends to have a much larger portion of events in higher t_{mod} regime than, for example, the T2bW type. Given the above features, a more sensible way is to bin in this variable instead of cutting on it, and the working points chosen for the binning are 0 and 10, indicated by the green vertical dashed lines in the figure.

The t_{mod} variable gives one of the the largest signal to background discrimination power for events after the preselection by M_{T}, second only to the $E_{\mathrm{T}}^{\mathrm{miss}}$ itself, mainly because it is directly targeting the lost lepton background, which is the largest background in this analysis. It is noted that other similar variables (like $M_{\mathrm{T2}}^{\mathrm{W}}$, topness) that target the dilepton $\mathrm{t\bar{t}}$ production with lost lepton final state can achieve similar results, and were used in the previous versions of this analysis. The t_{mod} is shown to have a slight advantage for lowering the required number of b-tagged jet in its construction, and for being more efficient in rejecting background, not only because it is now able to reject events with one of the b jet not tagged, but also because it is able to cover the lost lepton scenarios of tW events, which are the subleading contribution to the lost lepton background.

3.4.1.2 $M_{\ell\mathrm{b}}$ with the closest b jet

For an event with top quark produced (e.g. $\mathrm{t\bar{t}} \to 2\ell$ or $\mathrm{t\bar{t}} \to 1\ell$), the invariant mass of the lepton and the b quark coming from the same top quark decay shall be limited by

$$m_{\ell \mathrm{b}} \leq m_{\mathrm{t}} \sqrt{1 - \frac{m_{\mathrm{W}}^2}{m_{\mathrm{t}}^2}} \approx 153\,\mathrm{GeV}. \tag{3.3}$$

From the reconstructed objects, the $M_{\ell \mathrm{b}}$ variable is designed to probe the $m_{\ell \mathrm{b}}$ in Equation 3.3, by defining it as the invariant mass of the system of the selected lepton and the b jet (identified by the *medium* WP on the DeepCSV score) that is closest to to the lepton in terms of $\Delta R \equiv \sqrt{\Delta\eta^2 + \Delta\phi^2}$.

Since the required information for this variable include only the visible parts of the semi-leptonic top quark decay and do not depend on $E_{\mathrm{T}}^{\mathrm{miss}}$, this bound also applies to T2tt-like signals that contain on-shell top quark decays as well. On the other hand, such a bound would not exist for the W+jets background or the T2bW-like signals, as there are no on-shell top produced in any intermediate steps. Thus, a selection on $M_{\ell \mathrm{b}}$ could either reduce the W+jets background, by requiring a lower value in $M_{\ell \mathrm{b}}$ when we are looking for T2tt-like signals, or greatly suppress the $\mathrm{t\bar{t}}$ background, by requiring a higher value in $M_{\ell \mathrm{b}}$ when we are looking for T2bW-like signals. In this analysis, the $M_{\ell \mathrm{b}}$ variable is used for binning the events into low and high $M_{\ell \mathrm{b}}$ signal regions. This way we maintain the ability to probe both types of the signals at the same time, with the same set of signal regions.

Figure 3.10 shows the $M_{\ell \mathrm{b}}$ distribution for the SM backgrounds as well as the shapes of 3 T2tt- or T2bW-like signals with different mass splittings for our baseline selection. We can see from the figure that the high $M_{\ell \mathrm{b}}$ region is dominated by W+jets (1ℓ not from t), as expected, while the $\mathrm{t\bar{t}}$ (lost lepton) background is mostly concentrated at lower

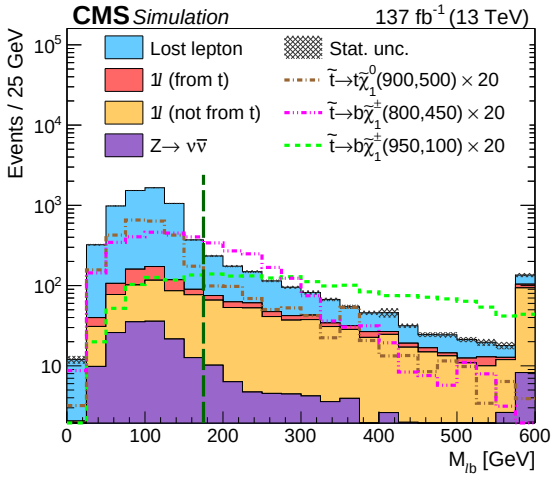

Figure 3.10: Distribution of after after the baseline selection, for the main backgrounds and various signal models. The SM contributions shown in stacked histogram overlaid by some example signal points shown in dotted lines. The signals are scaled up by 20 times in order to easily compare the shapes. The green dashed vertical line indicate the working points where we would use to make classification to the events in Section 3.4.

$M_{\ell b}$ values. While the T2tt signals shows very similar behavior as the $t\bar{t}$ background, the T2bW signals, especially those with larger $\Delta M(\tilde{t}, \tilde{\chi}_1^0)$, tend to have more events at higher $M_{\ell b}$. Considering the physical consequence from Equation 3.3 and accounting for some of the smearing effect coming from the detector resolution at the same time, the division point for "low" and "high" $M_{\ell b}$ regions is chosen to be 175 GeV, and it is drawn as dashed green vertical line in the figure.

To further reduce the W+jets background for the high $M_{\ell b}$ region, we will tighten the b tagging requirement in this region to use the *tight* WP for the DeepCSV b tagging scores to reduce the mistag rate, given that most of the W+jets backgrounds are produced with light-flavor jets. Events with $M_{\ell b} > 175$ GeV and the highest b tagging score in the event that passes the *medium* but not *tight* WP will not be included in any of the final

signal regions.

3.4.1.3 Top tagging

One important feature to note in the decay of the T2tt signal in the single lepton final state, is that one of the top quark is decaying fully hadronically. In contrast, in both the leading and subleading SM backgrounds, $t\bar{t}/tW \to 2\ell$ or $W + \text{jets}$, there would not be any hadronically decaying top in the final states, and the extra jets should be coming from ISR/FSR. This feature can provide an extra handle to us if we can identify the hadronic decays with the help of top taggers to distinguish the signal against the background.

Depending on how boosted the top quark is, we may be able to find its decay products in 3 independent AK4 jets if the top is not acquiring a lot of momentum, or we may find the decay products merged into a single AK8 jet, if the top is heavily boosted. A rough guiding formula for the relation between the ΔR of the decay products and the energy of the mother particle that can be obtained from a simple calculation, would be $\Delta R \approx \frac{2m}{E}$, with m and E indicating the mass and energy of the mother particle. Using this formula, we would expect the top quark decay products to start merging into a single AK8 jet when the top quark momentum reaches $p > 430\,\text{GeV}$. The governing feature for the average boost of the top quark in the final state in each of the signal scenarios would be the variable $\Delta M(\tilde{t}, \tilde{\chi}_1^0)$. Since we do not have any hint yet on where signal may be hiding in nature, we are scanning through all the possible $\Delta M(\tilde{t}, \tilde{\chi}_1^0)$ for a given $m_{\tilde{t}}$, so

either or both types of the decay may be preferred depending on the exact signal we are looking for. On the other hand, we also want to keep the analysis selections as general as possible and it should not change over the different signal hypotheses being looked at. Hence, we employ both a resolved tagger and a merged tagger to target both the resolved and boosted scenarios, by using two deep neural networks (DNNs) to identify hadronically decaying top quarks from the final states.

One DNN, referred to as the resolved tagger, uses the DeepResolved algorithm [60] to identify top quarks with a moderate Lorentz boost, where the decay products result in three separate jets (resolved top quark decay). The DeepResolved algorithm identifies top quarks whose decay products formed three AK4 jets. The three jets of each candidate must have an invariant mass between 100 and 250 GeV, no more than one of the three jets can be identified as a b-tagged jet, and the three jets must all lie within a cone of $\Delta R < 3.14$ of the trijet centroid. The neural network, constructed with information on both the trijet system and the individual jets, is then used to distinguish between trijet combinations whose three jets all match to a decay product of a top quark versus those that do not. The event is considered to have resolved top quark tag if at least one top candidate has discriminator value above a chosen threshold of 0.95.

The second DNN, referred to as a merged tagger, uses the DeepAK8 [61] algorithm to identify top quarks with large boost, where the decay products are merged into a single large-R jet (merged top quark decay). The identification of this boosted top quark signature is based on AK8 jets. A threshold of 0.4 on the discriminator value of the

DeepAK8 tagger is chosen for this analysis.

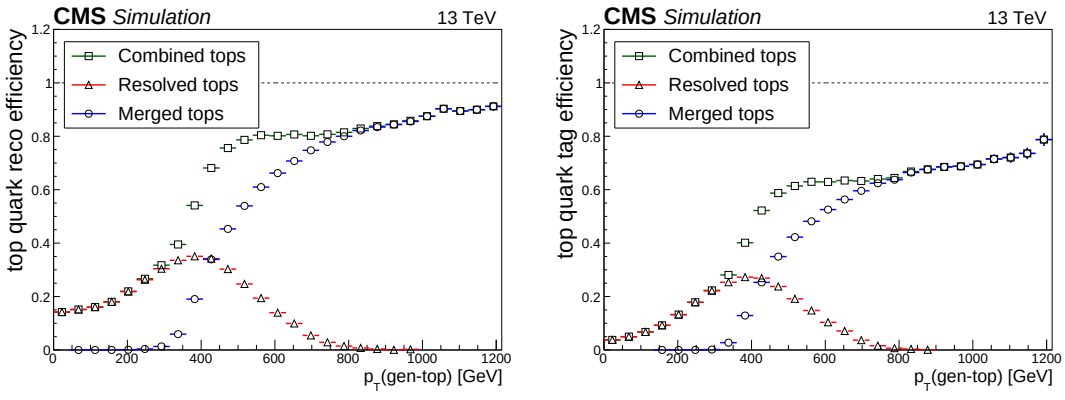

Figure 3.11: The efficiency of a generator truth top quark being reconstructed into the corresponding jet configurations (left) or tagged by the corresponding top taggers (right), as a function of the p_{T} of the top. The decay products of the hadronically decaying top quark are required to be separately identified as three AK4 jets with one of them b-tagged for the top to be categorized as a resolved top, or are all within $\Delta R < 0.8$ of one AK8 jet for the top to be categorized as a merged top. The correct jet configuration is a prerequisite for the top quark to be defined as tagged by the corresponding top tagger.

Figure 3.11 (right) shows the efficiencies of a top quark being tagged by the two types of top taggers as well as their combined efficiency as a function of the p_{T} of the top quark from generator truth information, from the $\mathrm{t\bar{t}}$ simulation. Figure 3.11 (left) also shows the efficiencies for the top quark to be fully reconstructed with the correct jet configurations, i.e. the decay products of the hadronically decaying top quark are required to be separately identified as three AK4 jets with one of them b-tagged for the top to be categorized as a resolved top, or are all within $\Delta R < 0.8$ of one AK8 jet for the top to be categorized as a merged top. The top quark being successfully reconstructed in correct jet configuration is a prerequisite for it to be defined as tagged by the corresponding top tagger. From these two plots, we can clearly see a division

at around 400 GeV in p_{T} where the top quark is becoming more likely to be merged than resolved. We can also conclude that the major limiting factor for the efficiency on the resolved tops is not on the tagging algorithm but the kinematic restrictions on its input (i.e. whether we can find all of the decay products of the top quark as jets with $p_{\mathrm{T}} > 30$ GeV).

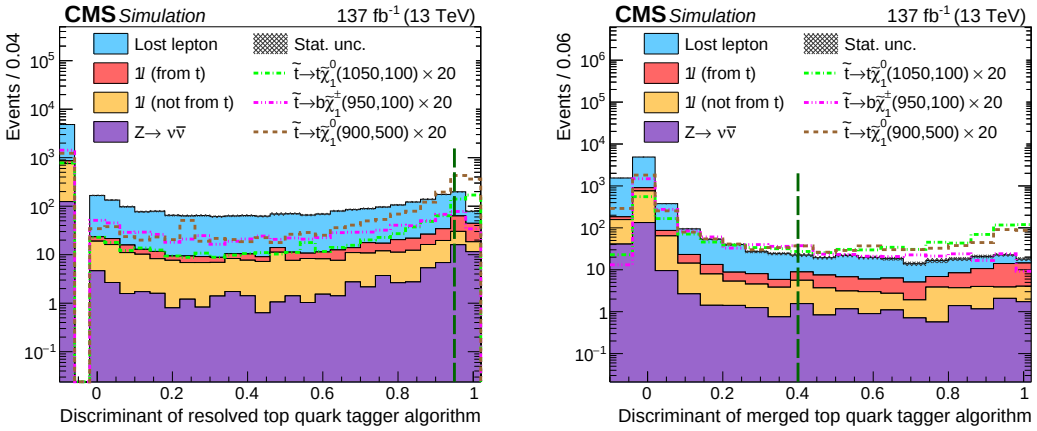

Figure 3.12: Distribution of the leading score from resolved top tag (left) and merged top tag (right) for events after the baseline selection, defined in Section 3.3.3, for the main backgrounds and some example signal models. The leftmost bins (score <0) in both cases are filled with events that do not have the presence corresponding tagged object. The green dashed line indicates the value where we choose as working point for determine whether the we consider the event has the presence of the tagged object.

Figure 3.12 shows the distribution of the leading discriminant values for the resolved tagger (left) and for the merged tagger (right), for events after the baseline selection. Since we are expecting at most one hadronically decaying top quark for our signals, we do not count the number of top tags, but view them as boolean flags that tell us whether an event contains a hadronically decaying top quark. The working point is designed for the leading score of each tagger, to be 0.95 for the resolved tagger and 0.4 for the

merged tagger for a balance between the tagging efficiency and mistag rate from the SM backgrounds in our signal regions. When both taggers give a valid tag for their category, priority is given to the merged top tag as it has a higher tagger efficiency versus mistag rate. For more detailed studies on the tagging efficiencies and the derivation of correction factors, refer to Appendix A.1.

3.4.2 Standard search regions

The main analysis is designed with the mindset to cover all decay scenarios and phase spaces for the T2tt, T2bW and T2bt type of signals. All signals should have produced $\geq$4 jets as baseline, however the number of jets is divided as 2–3 jets and $\geq$4 jets, since the 2–3 jets category are enriched in $t\bar{t} \to 2\ell$ backgrounds, the decision is to drop events with $t_{\text{mod}} < 10$ for the 2–3 regions, and keep only the part where the $t\bar{t} \to 2\ell$ background is already suppressed by the $t_{\text{mod}} \geq 10$ requirement.

For the top tags, it is only reasonable to have them defined where T2tt-like signals are enriched, so only the regions with $M_{\ell \text{b}} < 175\,\text{GeV}$ are split by the top tags. It should also be noted that for events with only 2 jets, the resolved top tag cannot be defined as it needs at least 3 jets as input, while in 3 jets events, there's likely a lost jet or merged jet that is potentially creating ill-defined resolved top as well. Hence the resolved top tag is also not used as categorization in the 2–3 jets regions. One other complication for the top tags is its application to events with lower $E_{\text{T}}^{\text{miss}}$ values only, namely $E_{\text{T}}^{\text{miss}} < 450\,\text{GeV}$ for $\geq$4 jets events and $E_{\text{T}}^{\text{miss}} < 600\,\text{GeV}$ for 2–3 jets events. This because of the concerns

with the statistical power, to avoid inundating the expected signal yield by the statistical and systematic uncertainties from the background. Since the $E_{\mathrm{T}}^{\mathrm{miss}}$ itself is the most discriminating variable for the stop signals, we should prioritize the higher $E_{\mathrm{T}}^{\mathrm{miss}}$ bins. While the top tags could greatly help increase the signal to background ratio in the lower $E_{\mathrm{T}}^{\mathrm{miss}}$ bins, they could also be hindering the background estimations efforts for the higher $E_{\mathrm{T}}^{\mathrm{miss}}$ bins, so they are eventually given up to preserve reasonable expected events in the high $E_{\mathrm{T}}^{\mathrm{miss}}$ bins.

Table 3.6: The definition of signal regions of the standard selection, based on the preselection criteria described in Section 3.3.3. At least one b-tagged jet selected by the medium (tight) working point is required for search regions with $M_{\ell\mathrm{b}}$ lower (higher) than 175 GeV. For the top quark tagging categories, we use the abbreviations U for untagged, M for merged, and R for resolved.

Label	N_{j}	t_{mod}	$M_{\ell\mathrm{b}}$ [GeV]	Top Tag	$E_{\mathrm{T}}^{\mathrm{miss}}$ bins [GeV]
A0	2–3	≥10	<175	Inclusive	[600, 750, +∞]
A1				Untagged	[350, 450, 600]
A2				Mer. tag	[250, 600]
B			≥175	Inclusive	[250, 450, 700, +∞]
C	≥4	<0	<175	Inclusive	[350, 450, 550, 650, 800, +∞]
D			≥175	Inclusive	[250, 350, 450, 600, +∞]
E0		0–10	<175	Inclusive	[450, 600, +∞]
E1				Untagged	[250, 350, 450]
E2				Mer. tag	[250, 350, 450]
E3				Res. tag	[250, 350, 450]
F			≥175	Inclusive	[250, 350, 450, +∞]
G0		≥10	<175	Inclusive	[450, 550, 750, +∞]
G1				Untagged	[250, 350, 450]
G2				Mer. tag	[250, 350, 450]
G3				Res. tag	[250, 350, 450]
H			≥175	Inclusive	[250, 500, +∞]

Table 3.6 records the division of events after preselection criteria described in Section 3.3.3 into the individual signal regions. In each line, we assign an alphabet letter as the SR label to the events that fall in the same category of N_{j}, N_{b}, t_{mod}, $M_{\ell\mathrm{b}}$ and they

are called "topological" regions. For these regions with $M_{\ell \mathrm{b}} < 175\,\mathrm{GeV}$, namely regions A, C, E, G, they are also separated by the conditions on top tags with numbers 0 to 3 attached to the alphabet label. Number 0 is given to those higher $E_{\mathrm{T}}^{\mathrm{miss}}$ bins that the top tagging is not applied, while number 1–3 are given to events that do not have any top tag, have merged top tag or only have resolved top tag, respectively. For events with $\geq$4 jets that have both a merged top tag and a resolved top tag present, the priority is given to the merged top tag category, as the DeepAK8 tagger was shown to have a better tagging efficiency vs mistag rate over the DeepResolved tagger for our background compositions.

The last step is to determine the edges for the $E_{\mathrm{T}}^{\mathrm{miss}}$ binning, to maximize the sensitivity for the signals by creating the larger signal to background ratio (by extending bins with higher $E_{\mathrm{T}}^{\mathrm{miss}}$ value as the low bin edge) as well as preserving signal significance of the signals (by retaining levels of lower $E_{\mathrm{T}}^{\mathrm{miss}}$ bins that could be combined with the higher $E_{\mathrm{T}}^{\mathrm{miss}}$ bins during the fitting process). The guiding principle of keeping around 1 expected yields from all the SM backgrounds in the last $E_{\mathrm{T}}^{\mathrm{miss}}$ bin, while the bins that are immediately lower in $E_{\mathrm{T}}^{\mathrm{miss}}$ is less than an order of magnitude larger in expected yields. The edges for the $E_{\mathrm{T}}^{\mathrm{miss}}$ binning are shown in the last column of Table 3.6. Lastly, the lower $E_{\mathrm{T}}^{\mathrm{miss}}$ bin (250–350 GeV) for signal regions A1 and C are excluded from the final set of signal regions, as they possess a large amount of background events while having very little expected events from signal scenarios that are not yet excluded.

Tables 3.7, 3.8 and 3.9 list the changes in expected yields after applying the baseline

selections and requirements for the binning variable on example signals of the T2tt, T2bW and T2bt type, respectively. For the first part, the baseline selections are applied on top of the previous, while on the second part, the binning variables (t_{mod}, $M_{\ell\text{b}}$ and the top tags) are all applied on top of the baseline selections.

Table 3.7: Cutflow table using the standard selection for T2tt signals for an integrated luminosity of 137.2 fb^{-1}. The t_{mod}, $M_{\ell\text{b}}$ and the top tags are all applied on top of the baseline selections that end with $p_{\text{T}}^{\text{miss}} > 250\,\text{GeV}$. The uncertainties are purely statistical. No correction for signal contamination in data control regions are applied.

Selection	$m_{\tilde{\text{t}}}$ [GeV]	$m_{\tilde{\chi}_1^0}$ [GeV]	$m_{\tilde{\text{t}}}$ [GeV]	$m_{\tilde{\chi}_1^0}$ [GeV]	$m_{\tilde{\text{t}}}$ [GeV]	$m_{\tilde{\chi}_1^0}$ [GeV]
$\text{pp} \to \tilde{\text{t}}\bar{\tilde{\text{t}}} \to \text{t}\bar{\text{t}}\tilde{\chi}_1^0\tilde{\chi}_1^0$	1050	50	850	100	650	350
$\geq 1\ell$, ≥ 2 jets, $p_{\text{T}}^{\text{miss}} > 150\,\text{GeV}$	180.2 ± 1.4		791 ± 6		3445 ± 20	
$+\ M_{\text{T}} > 150\,\text{GeV}$	150.7 ± 1.3		630 ± 6		2111 ± 16	
$+\ \geq 1$ b-tagged jet	119.1 ± 1.1		511 ± 5		1780 ± 14	
$+\ 2^{\text{nd}}\ell$ veto	100.9 ± 1.0		429 ± 5		1482 ± 13	
$+\ \tau_{\text{h}}$, iso. track veto	94.4 ± 1.0		395 ± 4		1363 ± 12	
$+\ \min \Delta\phi(j_{1,2}, \vec{p}_{\text{T}}^{\text{miss}}) > 0.8$	80.0 ± 0.9		339 ± 4		1154 ± 11	
$+\ \vec{p}_{\text{T}}^{\text{miss}} > 250\,\text{GeV}$	74.1 ± 0.9		296 ± 4		650 ± 8	
$t_{\text{mod}} > 0$	57.7 ± 0.8		221.9 ± 3.3		354 ± 6	
$t_{\text{mod}} > 10$	44.3 ± 0.7		156.4 ± 2.8		144 ± 4	
$M_{\ell\text{b}} > 175\,\text{GeV}$	21.5 ± 0.5		71.7 ± 2.0		90.1 ± 3.2	
$M_{\ell\text{b}} \leq 175\,\text{GeV}$	52.7 ± 0.7		224.4 ± 3.3		560 ± 8	
Merged t tag ≥ 1	27.7 ± 0.5		86.0 ± 2.1		53.2 ± 2.4	
Resolved t tag ≥ 1	14.0 ± 0.4		63.3 ± 1.7		137 ± 4	

3.4.3 Dedicated top and W corridor search regions

Table 3.10 records the division of events for the 2 dedicated corridor searches into the individual search regions, after the preselection criteria described in Section 3.3.3 and their shared follow-up modification in Section 3.3.4. Alphabet label I is assigned to the top corridor and J is assigned to the W corridor search regions. The different N_{j} and N_{b} requirement are also listed in the table to identify the main difference between the

Table 3.8: Cutflow table using the standard selection for T2bW signals for an integrated luminosity of 137.2 fb^{-1}. The t_{mod}, $M_{\ell\text{b}}$ and the top tags are all applied on top of the baseline selections that end with $p_{\text{T}}^{\text{miss}} > 250\,\text{GeV}$. The uncertainties are purely statistical. No correction for signal contamination in data control regions are applied.

Selection	$m_{\tilde{\text{t}}}$ [GeV]	$m_{\tilde{\chi}_1^0}$ [GeV]	$m_{\tilde{\text{t}}}$ [GeV]	$m_{\tilde{\chi}_1^0}$ [GeV]	$m_{\tilde{\text{t}}}$ [GeV]	$m_{\tilde{\chi}_1^0}$ [GeV]
	950	100	850	350	600	400
$\geq 1\ell$, ≥ 2 jets, $p_{\text{T}}^{\text{miss}} > 150\,\text{GeV}$	402.5 ± 2.9		1105 ± 8		3595 ± 20	
$+\ M_{\text{T}} > 150\,\text{GeV}$	278.6 ± 2.5		705 ± 7		1461 ± 13	
$+\ \geq 1$ b-tagged jet	236.0 ± 2.2		620 ± 6		1276 ± 12	
$+\ 2^{\text{nd}}\ell$ veto	196.7 ± 2.0		514 ± 6		1030 ± 11	
$+\ \tau_{\text{h}}$, iso. track veto	180.8 ± 1.9		469 ± 5		938 ± 10	
$+ \min \Delta\phi(j_{1,2}, \vec{p}_{\text{T}}^{\text{miss}}) > 0.8$	133.0 ± 1.7		358 ± 5		699 ± 9	
$+\ \vec{p}_{\text{T}}^{\text{miss}} > 250\,\text{GeV}$	109.3 ± 1.5		235 ± 4		252 ± 5	
$t_{\text{mod}} > 0$	58.5 ± 1.1		129.3 ± 2.8		82.0 ± 2.9	
$t_{\text{mod}} > 10$	42.8 ± 0.9		75.8 ± 2.1		18.1 ± 1.4	
$M_{\ell\text{b}} > 175\,\text{GeV}$	82.7 ± 1.3		123.1 ± 2.7		25.5 ± 1.6	
$M_{\ell\text{b}} \leq 175\,\text{GeV}$	26.6 ± 0.8		111.8 ± 2.6		226 ± 5	
Merged t tag ≥ 1	11.0 ± 0.5		18.9 ± 1.1		6.9 ± 0.8	
Resolved t tag ≥ 1	4.59 ± 0.3		19.0 ± 1.0		28.8 ± 1.6	

Table 3.9: Cutflow table using the standard selection for T2bt signals for an integrated luminosity of 137.2 fb^{-1}. The t_{mod}, $M_{\ell\text{b}}$ and the top tags are all applied on top of the baseline selections that end with $p_{\text{T}}^{\text{miss}} > 250\,\text{GeV}$. The uncertainties are purely statistical. No correction for signal contamination in data control regions are applied.

Selection	$m_{\tilde{\text{t}}}$ [GeV]	$m_{\tilde{\chi}_1^0}$ [GeV]	$m_{\tilde{\text{t}}}$ [GeV]	$m_{\tilde{\chi}_1^0}$ [GeV]	$m_{\tilde{\text{t}}}$ [GeV]	$m_{\tilde{\chi}_1^0}$ [GeV]
	900	50	750	400	500	300
$\geq 1\ell$, ≥ 2 jets, $p_{\text{T}}^{\text{miss}} > 150\,\text{GeV}$	407 ± 4		828 ± 9		5788 ± 27	
$+\ M_{\text{T}} > 150\,\text{GeV}$	251.2 ± 2.9		548 ± 7		2336 ± 17	
$+\ \geq 1$ b-tagged jet	201.0 ± 2.5		465 ± 7		2027 ± 16	
$+\ 2^{\text{nd}}\ell$ veto	168.9 ± 2.3		417 ± 6		1792 ± 15	
$+\ \tau_{\text{h}}$, iso. track veto	153.8 ± 2.2		397 ± 6		1710 ± 14	
$+ \min \Delta\phi(j_{1,2}, \vec{p}_{\text{T}}^{\text{miss}}) > 0.8$	126.3 ± 2.0		335 ± 6		1349 ± 13	
$+\ \vec{p}_{\text{T}}^{\text{miss}} > 250\,\text{GeV}$	111.8 ± 1.9		238 ± 5		469 ± 7	
$t_{\text{mod}} > 0$	77.0 ± 1.5		159 ± 4		204 ± 5	
$t_{\text{mod}} > 10$	55.4 ± 1.3		92.6 ± 2.9		71.7 ± 2.8	
$M_{\ell\text{b}} > 175\,\text{GeV}$	31.4 ± 1.0		44.1 ± 2.0		68.1 ± 2.7	
$M_{\ell\text{b}} \leq 175\,\text{GeV}$	80.4 ± 1.6		194 ± 4		401 ± 7	
Merged t tag ≥ 1	21.6 ± 0.8		15.2 ± 1.2		10.7 ± 1.1	
Resolved t tag ≥ 1	12.4 ± 0.6		24.3 ± 1.5		30.1 ± 1.7	

two dedicated search regions. The binning variables t_{mod}, $M_{\ell\mathrm{b}}$ and the top taggers are not used in the dedicated corridor search regions, and the division is happening only in $E_{\mathrm{T}}^{\mathrm{miss}}$, following the same guiding principle as for the standard search regions. It should be noted that overlap of events is possible between the two sets of search regions (I, J) and the standard search regions (A–H).

Table 3.10: The definition of signal regions of the dedicated top and W corridor search strategies for the T2tt signals, based on the preselection criteria described in Section 3.3.3 and their modification in Section 3.3.4.

Label	N_{j}	$N_{\mathrm{b,\ med}}$	$N_{\mathrm{b,\ soft}}$	$E_{\mathrm{T}}^{\mathrm{miss}}$ bins [GeV]
I	≥ 5	≥ 1	–	[250, 350, 450, 550, 750, $+\infty$]
J	≥ 3	–	≥ 1	[250, 350, 450, 550, 750, $+\infty$]

Table 3.11 shows the changes in expected yields after applying the top and W corridor selections criteria on the compressed T2tt signals. For the first part, the selections are applied on top of the previous, while on the second part, N_{j}, N_{b}, and the soft b requirements are all applied on top of the common selections, ending with $p_{\mathrm{T}}^{\mathrm{miss}} > 250\,\mathrm{GeV}$.

Table 3.11: Cutflow table using the dedicated top and W corridor selections for the T2tt signals for an integrated luminosity of $137.2\,\text{fb}^{-1}$. The N_j and b tag requirements for the second part are all applied on top of the baseline selections that end with $p_\text{T}^\text{miss} > 250\,\text{GeV}$. The uncertainties are purely statistical. No correction for signal contamination in data control regions are applied.

Selection	$m_{\tilde{\text{t}}}$ [GeV]	$m_{\tilde{\chi}_1^0}$ [GeV]	$m_{\tilde{\text{t}}}$ [GeV]	$m_{\tilde{\chi}_1^0}$ [GeV]	$m_{\tilde{\text{t}}}$ [GeV]	$m_{\tilde{\chi}_1^0}$ [GeV]
	500	325	425	338	400	300
$\geq 1\ell$, ≥ 3 jets, $p_\text{T}^\text{miss} > 150\,\text{GeV}$	6361 ± 28		9583 ± 35		13422 ± 41	
+ $M_\text{T} > 150\,\text{GeV}$	1845 ± 15		2746 ± 19		4038 ± 22	
+ $2^\text{nd}\ell$ veto	1451 ± 13		2372 ± 17		3409 ± 20	
+ τ_h, iso. track veto	1301 ± 13		2175 ± 17		3134 ± 20	
+ leading jet not b-tagged	1136 ± 12		2090 ± 16		2996 ± 19	
+ $\min \Delta\phi(j_{1,2}, \vec{p}_\text{T}^\text{miss}) > 0.5$	839 ± 10		1642 ± 14		2394 ± 17	
+ $p_\text{T}^\ell < \max[50, (250 - 150 \times \Delta\phi(\ell, \vec{p}_\text{T}^\text{miss}))]\,\text{GeV}$	529 ± 8		1260 ± 12		1673 ± 14	
+ $\vec{p}_\text{T}^\text{miss} > 250\,\text{GeV}$	285 ± 5		761 ± 9		942 ± 10	
≥ 1 medium b-tagged jet	238 ± 5		113 ± 4		210 ± 5	
≥ 1 medium b-tagged jet, ≥ 5 jets	169 ± 4		55.0 ± 2.5		101.6 ± 3.2	
≥ 1 soft b-tagged jet	45.7 ± 2.2		110.5 ± 3.5		241 ± 5	

Chapter 4

Background estimation

As a first estimation of the size and the composition of the main SM background processes, MC simulation are used, and the results are visualized in Figure 4.1, in bins of Table 3.6 and 3.10. In fact, the expected yields from MC simulation in the different $E_{\mathrm{T}}^{\mathrm{miss}}$ bins provide also feedback to the determination of the edges of $E_{\mathrm{T}}^{\mathrm{miss}}$ for the SR categorization in those tables.

4.1 Lost-lepton background

The lost-lepton background represents the total background contribution from all physics processes that contain two or more charged leptons from W decays, where only one of the leptons is recognized, either because the other lepton(s) is(are) out of the detector acceptance (i.e. at high η not covered by the detector, or in between the slits of sub-detectors) or failed to be identified as good lepton (e.g. fails the lepton identification

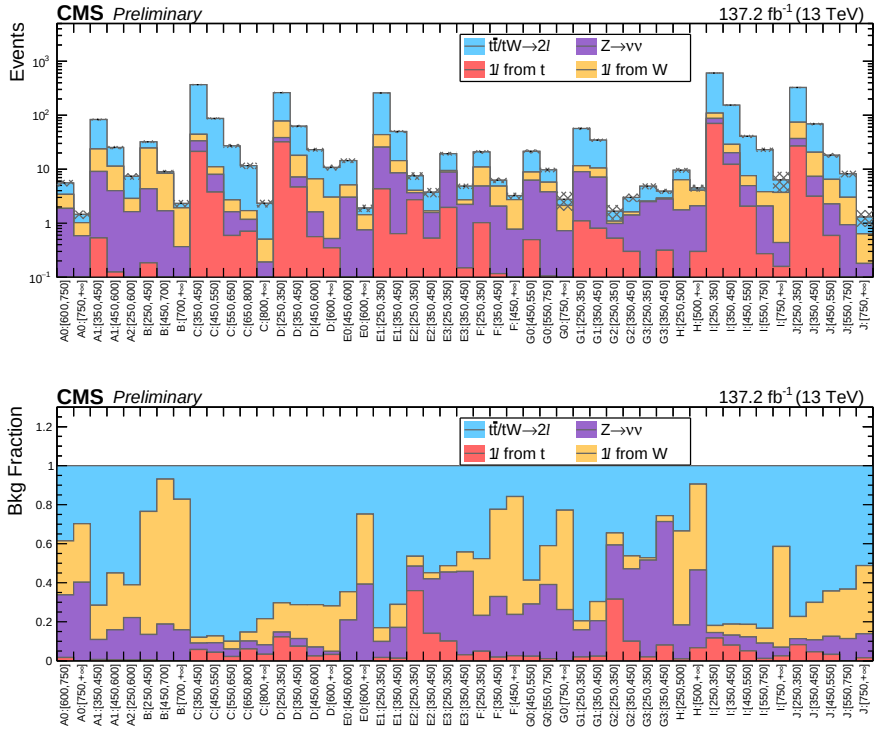

Figure 4.1: The total expected yields (top) and their composition when the yields are normalized to 1 (bottom), from MC simulation in each of the individual signal regions, corresponding to an integrated luminosity of 137.2 fb^{-1} and separated to SM background categories by generator information. The alphabet labels represent the topological regions defined in Table 3.6 and 3.10, and the numbers in brackets describe the $E_{\mathrm{T}}^{\mathrm{miss}}$ range, with dimension in GeV.

rules described in Section 3.1.1).

The presence of a second neutrino in the event could result in M_{T} escaping the limit set by the W mass. Additionally, the misreconstruction of the second lepton itself can contribute to the $E_{\mathrm{T}}^{\mathrm{miss}}$ spectrum in terms of smearing its magnitude. This type of background is thus the largest background in most of the signal regions of this analysis.

The $\mathrm{t\bar{t}}$ pair production, where the Ws from both tops decays leptonically, is the dominant process among the lost-lepton category. The single top production in association

with a W boson, where both the W and the t quark decay (semi-)leptonically, accounts for the second-largest contribution in this category. Additional contributions come from $t\bar{t}$ and diboson processes.

4.1.1 Overview of the estimation method

The lost-lepton background can be estimated by a data-driven method from dilepton control regions that are constructed to be similar to the signal regions but require at least two leptons in the final state. The logic behind is that all physics processes (which are mostly just $t\bar{t} \to 2\ell$) that can contribute as lost-lepton in SR, can be captured by the dilepton control regions when the second lepton is not lost, and the control regions can serves to measure their rate in the similar final state kinematic phase space (e.g. boost of the system) as they would be in the signal region. For the lepton selections, one of lepton is required to pass the *selection* criteria, same as for the signal region, while the other one is only required to pass the looser *trailing* criteria.

A simplified relationship between the counts in SR and CR for the observed data and simulation is shown in Equation 4.1.

$$N^{\mathrm{SR}}_{\text{lost-}\ell} = N^{\mathrm{CR}}_{\ell\ell} \times \frac{M^{\mathrm{SR}}_{\text{lost-}\ell}}{M^{\mathrm{CR}}_{\ell\ell}} \tag{4.1}$$

where we denote the number of data events by N and the expected number of events from MC simulation by M, and the superscript and subscript denotes the yields in SR or CR, and whether they are single lepton lepton (lost-ℓ) or dilepton ($\ell\ell$) events. The advantage

of such a procedure, is that by taking the ratio between the individual signal region and their corresponding control region, most of the systematic uncertainties regarding the MC modeling cancel out to first order, since they are affecting the signal region and control regions in the same way. The most important area where the MC simulation is required to model the data well is the lepton reconstruction and selection efficiency, which is responsible for the migration of events from $M_{\ell\ell}^{\mathrm{CR}}$ to $M_{\text{lost-}\ell}^{\mathrm{SR}}$, and the uncertainty on lepton efficiency is in fact now entering as the square. However, we can say that the lepton reconstruction is in general very well-modeled by simulation and also well controlled by the measurements through $\mathrm{Z}/\gamma^* \to \ell^+\ell^-$ events, and the derived correction factors for the selection efficiency at the percent level.

Other requirements for the control regions would be to have high purity of background contributions only, and that our estimation of the background not be biased by the signal strength. This, for most part, is naturally achieved in the dilepton control region by the fact that our target signals have much smaller cross sections compared to $\mathrm{t\bar{t}}$ production at the LHC. There are, however, sometimes large signal contamination when the signal in quest has $m_{\tilde{\mathrm{t}}}$ very close to m_{t}, where the signal cross section would be much larger. In these cases, the biases are captured by the signal yield modification method described in Section 5.2.1, and our sensitivity to the signal process is reduced. This competes with the positive impact on the signal yield in SR brought by that cross section increase, and in the end the loss in sensitivity is studied and it was determined that no special treatment is needed for these signal hypotheses.

4.1.2 Construction of the dilepton control region

For the construction of the dilepton control region, the following modifications are applied to the signal region selections as summarized in Section 3.3.3 for the standard selections or Section 3.3.4 for the dedicated corridor searches.

- Require the presence of a second lepton passing the *trailing* criteria.
- The veto on any extra lepton or isolated track is removed.
- All $\vec{p}_{\mathrm{T}}^{\,\mathrm{miss}}$ related variables, which included $E_{\mathrm{T}}^{\mathrm{miss}}$, M_{T}, $\min\Delta\phi(j_{1,2},\vec{p}_{\mathrm{T}}^{\,\mathrm{miss}})$, t_{mod} and $\Delta\phi(\ell,\vec{p}_{\mathrm{T}}^{\,\mathrm{miss}})$, are recalculated with the 4-vector of the second lepton added to the $\vec{p}_{\mathrm{T}}^{\,\mathrm{miss}}$. The second lepton can be the lepton that failed the *selection* criteria, or the subleading p_{T} lepton when both leptons pass that selection. This new quantity is referred to as removed-lepton $E_{\mathrm{T}}^{\mathrm{miss}}$.
- An additional requirement $M_{\mathrm{T2}}^{\ell\ell} < 100\,\mathrm{GeV}$ is placed to avoid any overlap with the signal regions for stop search in the dilepton final states.*

The kinematic distributions for dilepton events after the baseline selections as described above are shown in Figure 4.2, for full amount of data and MC simulation, taken/generated over the years 2016–2018. In these figures, the background categorization is similar to those of the SR with only the lost lepton contribution replaced by the dilepton contributions. There is a total normalization scale of 0.81 applied to all MC events, to allow a better comparison in the shape. It can be seen from the figures

*This is a separate CMS search, and will not receive further discussion here.

that, apart from the total normalization, the distributions of the analysis variables are in general well modeled by MC simulations, except for the $E_{\mathrm{T}}^{\mathrm{miss}}$ distribution where some discrepancies can be seen building up from around $E_{\mathrm{T}}^{\mathrm{miss}} > 450\,\mathrm{GeV}$.

It should be noted that some discrepancies between observed data and the MC simulation are expected and are in general not a worry for the estimation, except in the $E_{\mathrm{T}}^{\mathrm{miss}}$ distribution. The discrepancy observed in higher $E_{\mathrm{T}}^{\mathrm{miss}}$ can have significant implication in the $E_{\mathrm{T}}^{\mathrm{miss}}$ extrapolation process that is to be discussed below, and need to be corrected for. The source this discrepancy, together with the large disagreement in the overall normalization for the dilepton CR, is found to come from the mismodeling in the $\mathrm{t\bar{t}}$ MC samples, specifically those used to model the running conditions of the year 2017 and 2018. The discrepancies had been further studied under the $\mathrm{e\mu}$ cross-check regions described in Section 4.1.4, and correction factors are derived to control the $E_{\mathrm{T}}^{\mathrm{miss}}$ shape for the $E_{\mathrm{T}}^{\mathrm{miss}}$ extrapolation process. On the other hand, we decided that the disagreement in the normalization does not have a significant impact in our lost lepton estimation, as this effect is expected to cancel out in Equation 4.1.

4.1.3 $E_{\mathrm{T}}^{\mathrm{miss}}$ extrapolation

Due to the aggressive binning of the signal towards large $E_{\mathrm{T}}^{\mathrm{miss}}$ values to enhance our sensitivity, we would naturally also expect very few dilepton events to fall into the corresponding control region for those high $E_{\mathrm{T}}^{\mathrm{miss}}$ SRs. This could become a problem itself, since with low expected events, the final estimation can be very susceptible to fluctuation

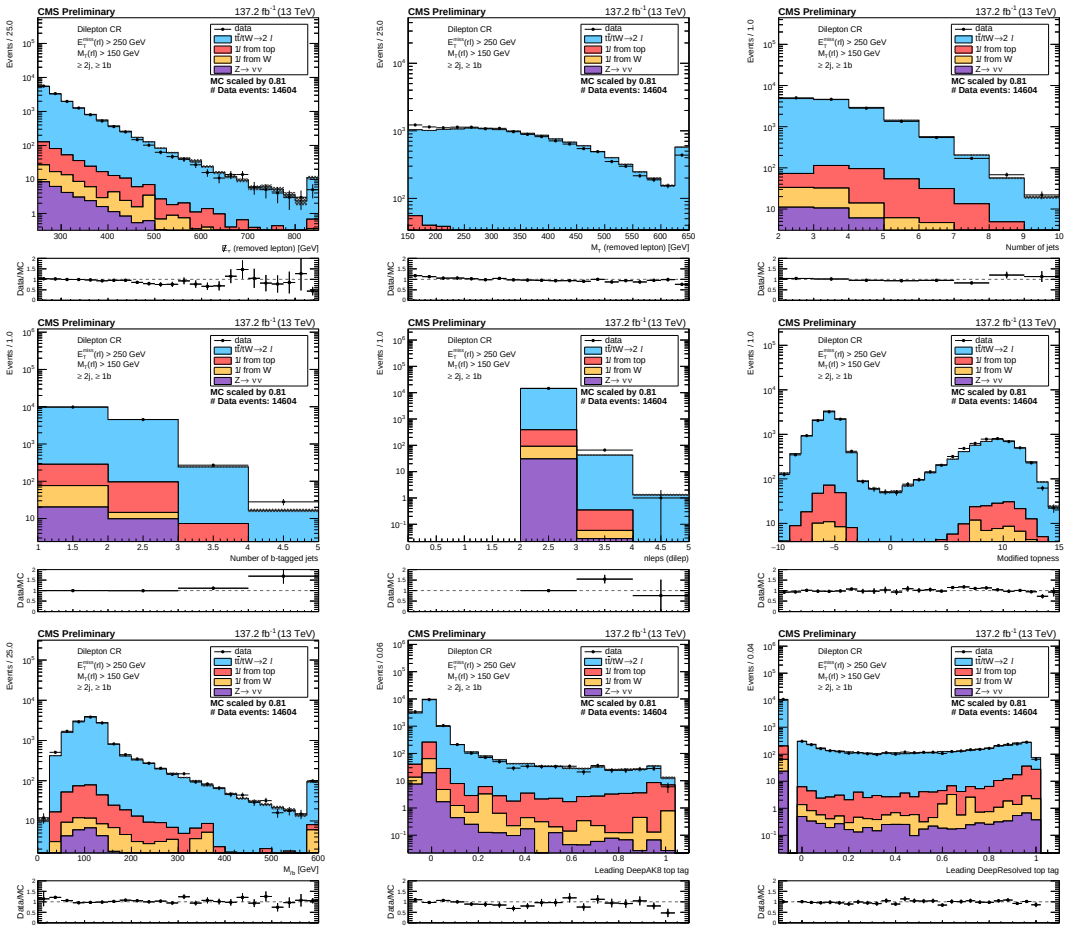

Figure 4.2: Kinematic distributions in the dilepton CR from the simulation and observed data after the baseline selections that are described in Section 4.1.2. The observed data are collected over the period of 2016–2018, corresponding to an integrated luminosity of 137.2 fb^{-1}. The stacked histograms showing the SM background, similar to those described in Section 2.3 with the lost lepton contribution replaced by the dilepton contributions, are first scaled to the same amount of luminosity, and then further scaled by 0.81 to have the same integration as the observed data events, to allow a better comparison in the shape. The last bin in each distribution includes the overflow events as usual.

of the observed yields in the CR. A mitigation strategy called "$E_{\text{T}}^{\text{miss}}$ extrapolation" is thus introduced, and Equation 4.1 becomes Equation 4.2

$$N_{\text{lost-}\ell}^{\text{SR}} = N_{\ell\ell}^{\text{CR}} \times \frac{M_{\text{lost-}\ell}^{\text{SR}}}{M_{\ell\ell}^{\text{CR}}} \times \left(\frac{M_{\ell\ell}^{\text{CR, } E_{\text{T}}^{\text{miss}} \text{ bin}}}{M_{\ell\ell}^{\text{CR, comb}}} \right) \tag{4.2}$$

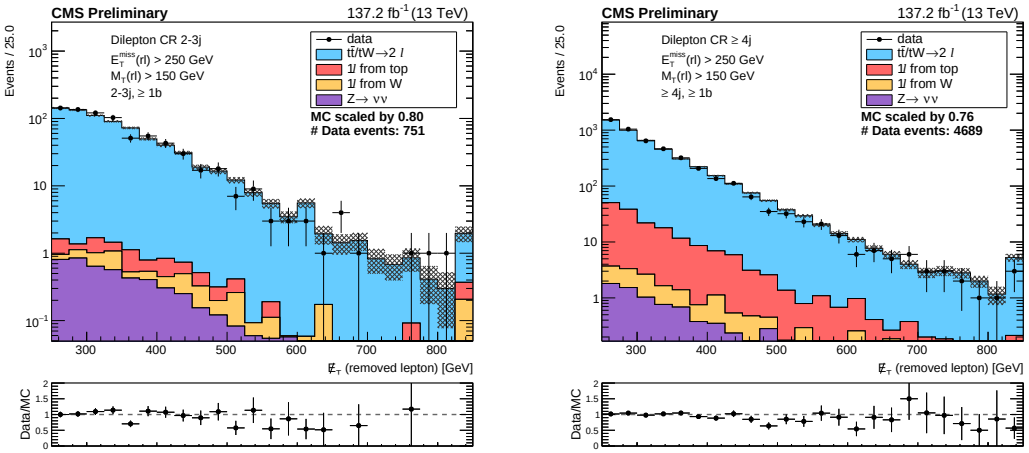

Figure 4.3: Distribution of $E_{\mathrm{T}}^{\mathrm{miss}}$ in the dilepton CR, based on the baseline selections and with the addition of the < 4 jets, $t_{\mathrm{mod}} > 10$ (left) and $\geq$4 jets (right). The left plot can be viewed as the $E_{\mathrm{T}}^{\mathrm{miss}}$ distribution in the aggregated region of SR A and B, and the right as the aggregation of SR C–H.

by combining the neighboring $E_{\mathrm{T}}^{\mathrm{miss}}$ bins of the low statistics CRs into a single one, and introducing an extra $E_{\mathrm{T}}^{\mathrm{miss}}$ extrapolation factor as the last term. Inside the $E_{\mathrm{T}}^{\mathrm{miss}}$ extrapolation factor, $M_{\ell\ell}^{\mathrm{CR,\ comb}}$ represents the yields in the combined control region and $M_{\ell\ell}^{\mathrm{CR,\ } E_{\mathrm{T}}^{\mathrm{miss}}\ \mathrm{bin}}$ represents the original estimation of the individual control region before it is combined with its neighbor. The threshold for making such combination is set to 5 expected events in the CR over the integrated luminosity of $137.2\,\mathrm{fb}^{-1}$, and the list of raw dilepton CR that require $E_{\mathrm{T}}^{\mathrm{miss}}$ extrapolation is shown in Table 4.1.

The main reason for using $M_{\ell\ell}^{\mathrm{CR,\ } E_{\mathrm{T}}^{\mathrm{miss}}\ \mathrm{bin}}$ here instead of the more proper $M_{\ell\ell}^{\mathrm{SR,\ } E_{\mathrm{T}}^{\mathrm{miss}}\ \mathrm{bin}}$ is again due to statistical concern, since we expect very few MC events in the designed signal region, as it is reflected in the size of the statistical only uncertainties in Table 4.1.

Since the extrapolation factors are extracted purely from the MC simulation, it is important to make sure that the shape of the $E_{\mathrm{T}}^{\mathrm{miss}}$ is modeled well. One of the known

Table 4.1: The dilepton control regions where we are applying the $E_{\mathrm{T}}^{\mathrm{miss}}$ extrapolation, quantitatively identified as the expected yields from Monte Carlo simulation in the control region ($M_{\ell\ell}^{\mathrm{CR}}$) is less than 5 for an integrated luminosity of 137.2 fb^{-1}. The region will be merged with the one lower in $E_{\mathrm{T}}^{\mathrm{miss}}$, to form a single control region, iterative. The expected yield from Monte Carlo for the lost-lepton contribution in the SR ($M_{\text{lost-}\ell}^{\mathrm{SR}}$) are also shown as a reference.

Label	$E_{\mathrm{T}}^{\mathrm{miss}}$ [GeV]	$M_{\ell\ell}^{\mathrm{CR}}$ Expected	$M_{\text{lost-}\ell}^{\mathrm{SR}}$ Expected	$E_{\mathrm{T}}^{\mathrm{miss}}$ [GeV]	$M_{\ell\ell}^{\mathrm{CR}}$ Expected	$M_{\text{lost-}\ell}^{\mathrm{SR}}$ Expected
A0	600–750	17.457 ± 1.819	1.9 ± 0.56	>750	3.746 ± 0.782	0.55 ± 0.24
B	450–700	16.037 ± 4.687	0.62 ± 0.32	>700	1.837 ± 0.589	0.41 ± 0.27
C	650–800	14.092 ± 1.494	8.24 ± 1.26	>800	4.033 ± 0.843	5.36 ± 1.04
E0	450–600	31.117 ± 2.295	9.56 ± 1.34	>600	3.813 ± 0.821	0.67 ± 0.29
G0	550–750	19.45 ± 1.756	3.88 ± 0.8	>750	3.319 ± 0.699	1.07 ± 0.44
H	250–500	10.083 ± 1.303	3.27 ± 0.79	>500	4.048 ± 0.779	0.51 ± 0.26
I	550–750	14.497 ± 1.444	18.37 ± 1.86	>750	3.035 ± 0.728	3.93 ± 0.83
J	550–750	6.9 ± 1.25	5.2 ± 1.01	>750	0.8 ± 0.28	0.67 ± 0.4

problem for the 2016 $\mathrm{t\bar{t}}$ sample is its modeling of the initial state radiation, which in terms will affect the p_{T} of the $\mathrm{t\bar{t}}$ system that it is recoiling against, and hence affecting the $E_{\mathrm{T}}^{\mathrm{miss}}$ composed by the neutrinos from the top decay. And *ad hoc* correction had been derived based on the number of ISR jets in the MC sample, by comparing the number of jets distribution between the $\mathrm{t\bar{t}}$ simulation directly with the observed data in an $\mathrm{t\bar{t}}$ enriched region by an $\mathrm{e\mu}$ selection, and the results are listed in Table 4.2. The corrections are applied to the 2016 $\mathrm{t\bar{t}}$ samples and as well the stop signal samples, as they are expected to share the source of the problem that causes the mismodeling. The effectiveness of these correction is also verified in our own $\mathrm{e\mu}$ cross-check region that is discussed in the next section, and they have already been applied to the events that go in all the relevant figures in this thesis.

Table 4.2: The scale factors and uncertainties to apply to the simulation from the SUSY recommendation, in number of ISR jets. They are applied to the 2016 the $t\bar{t}$ sample and the signal FastSim samples of the 3 years.

$N_j^{ISR/FSR}$	0	1	2	3
Scale Factor	1.000 ± 0.000	0.920 ± 0.040	0.821 ± 0.090	0.715 ± 0.143

$N_j^{ISR/FSR}$	4	5	≥6
Scale Factor	0.662 ± 0.170	0.561 ± 0.221	0.511 ± 0.258

4.1.4 Cross-check with eμ events

The $t\bar{t}$ and tW contributions are the most important background component of this analysis, and it is important to understand how well they are modeled by the simulation, even if the lost lepton events are mainly estimated in the data-driven way based on the understanding of lepton efficiency. The eμ events dominantly consist of events with two W bosons in the final state, in which case the $t\bar{t}$ contribution is already an order of magnitude higher than the WW one, and with some requirement on the number of jets and b tag, the eμ events can be considered the easiest channel to measure the properties of the $t\bar{t}$ pair production at the LHC.

Apart from validating the modeling, we also derived important correction factors for the MC simulation or systematic constraints from this $t\bar{t}$/tW pure region, in places where E_T^{miss} extrapolation are applied.

4.1.4.1 Construction of the eμ cross-check regions

For this purpose, we define a $t\bar{t}\to 2\ell$ enriched region with the following selection:

- Pass any of the following eμ dilepton trigger
  - `HLT_Mu8_TrkIsoVVL_Ele23_CaloIdL_TrackIdL_IsoVL(_DZ)`
  - `HLT_Mu8_TrkIsoVVL_Ele17_CaloIdL_TrackIdL_IsoVL`
  - `HLT_Mu23_TrkIsoVVL_Ele12_CaloIdL_TrackIdL_IsoVL(_DZ)`
  - `HLT_Mu17_TrkIsoVVL_Ele12_CaloIdL_TrackIdL_IsoVL`
- Has exactly one electron and one muon with
  - $p_{\mathrm{T}} > 30(15)\,\mathrm{GeV}, |\eta| < 2.1$ for the leading (trailing) lepton
  - Oppositely charged between the 2 leptons
  - POG ID medium (tight) for e(μ)
  - Relative mini isolation < 0.1
- Invariant mass of the dilepton, $m_{\ell\ell} > 20\,\mathrm{GeV}$
- $N_{\mathrm{j}} \geq 2$, for jets with $p_{\mathrm{T}} > 30\,\mathrm{GeV}$,
- $N_{\mathrm{b}} \geq 0$, but the studies will be carried out in regions with 0, 1, and ≥2 b tags, based on the medium WP of the DeepCSV discriminant value

The efficiency of the combined eμ dilepton trigger set is measured in events from the $E_{\mathrm{T}}^{\mathrm{miss}}$ data set and passing an orthogonal $E_{\mathrm{T}}^{\mathrm{miss}}$ trigger. The method asks that an event passes the dilepton selection above, as well as the $E_{\mathrm{T}}^{\mathrm{miss}}$ trigger, then an efficiency is calculated based on whether or not the events pass the eμ dilepton trigger set listed

above. Figure 4.4 show the efficiencies as function of leading and trailing lepton p_{T}, and the number of jets. It can be seen that the trigger efficiencies are approximately flat within statistical uncertainties with respect to the kinematic quantities listed, and are also consistent throughout the 3 years of data taking. Since in all kinematic distributions shown later for the eμ control region the trigger efficiency was not accounted for in the simulation, we shall expect a base of 0.86 in the MC scale factors.

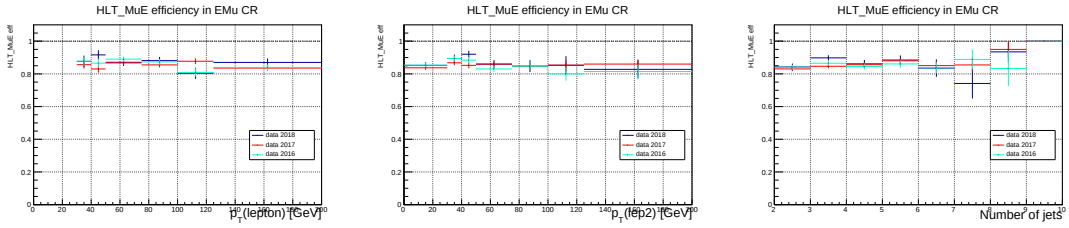

Figure 4.4: The eμ trigger efficiencies in run 2, separated in years, vs. the leading lepton p_{T} (left), trailing lepton p_{T} (center), or number of jets (right).

4.1.4.2 Kinematic distributions in the eμ cross-check regions

The first kinematic distributions to be looked at in the eμ cross-check region are the number of jets and the number of b tags, shown in Figure 4.5. The 2016 MC sample is known to have issue in modeling the ISR jets for $\mathrm{t\bar{t}}$ pair production, and the events from the $\mathrm{t\bar{t}}$ MC entering the plots have already been reweighted by the correction factors described in Table 4.2, based on the number ISR jets ($N_{\mathrm{j}}^{\mathrm{ISR/FSR}}$) from the generator truth information. It can be seen that with the change in Tune, the 2017–2018 MC can model the number of jets to a satisfactory level

The dominant effect for modeling the $E_{\mathrm{T}}^{\mathrm{miss}}$ correctly in the dilepton control region arises from the modeling of the $\mathrm{t\bar{t}}$ system p_{T}, labeled as $p_{\mathrm{T}}(\mathrm{t\bar{t}})$. We reconstruct the

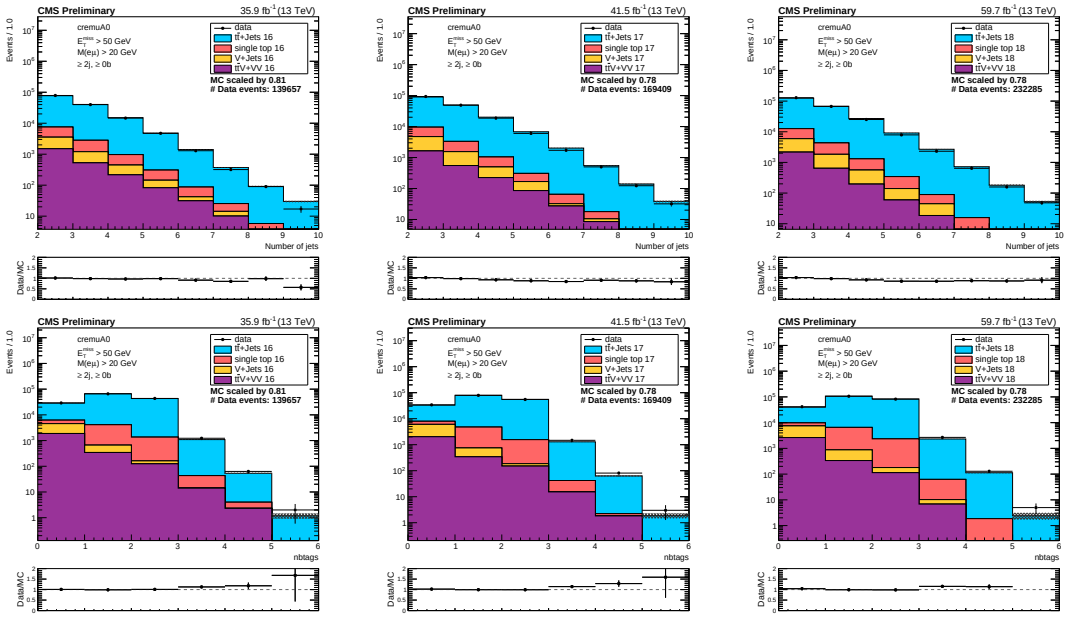

Figure 4.5: Distribution of number of jets (top row), and number of b tags (bottom row) for the eμ CR, both with ≥0 b tag requirement, for 2016 (left column), 2017 (middle column) and 2018 (right column).

approximation to the $p_{\mathrm{T}}(\mathrm{t\bar{t}})$ in the eμ control region, by taking the p_{T} from the sum of 4-vectors of the leading and trailing leptons, the two jets with the highest b tagging discriminator (DeepCSV) value, and the $\vec{p}_{\mathrm{T}}^{\,\mathrm{miss}}$. The comparisons of the $p_{\mathrm{T}}(\mathrm{t\bar{t}})$ distribution in data MC simulation for the 3 years are shown in Figure 4.6. The input variables to the calculation of $p_{\mathrm{T}}(\mathrm{t\bar{t}})$, i.e. dilepton p_{T}, p_{T} of the dijet system from the 2 leading b-tagged jets and the $E_{\mathrm{T}}^{\mathrm{miss}}$ are shown in Figure 4.7, separately for the observed data taken in 3 years as well as the MC samples produced to model the running condition of them.

It can be seen clearly that the 2017 and 2018 MC simulation are showing a trend in over-prediction towards the higher $p_{\mathrm{T}}(\mathrm{t\bar{t}})$ values, going up to over 20% for $p_{\mathrm{T}}(\mathrm{t\bar{t}}) >$ 600 GeV. The over-prediction can also be largely seen in the input variables to $p_{\mathrm{T}}(\mathrm{t\bar{t}})$, which also result from the mismodeling of the $\mathrm{t\bar{t}}$ system p_{T}. While the 2016 simulation

had been initially showing similar trend in the $p_{\mathrm{T}}(\mathrm{t\bar{t}})$ distribution before the application of the $N_{\mathrm{j}}^{\mathrm{ISR/FSR}}$ based correction factors, it can be seen that after the correction the data/MC agreement is largely restored in $p_{\mathrm{T}}(\mathrm{t\bar{t}})$ to a satisfactory level, and the agreements in the input variables, especially the $E_{\mathrm{T}}^{\mathrm{miss}}$ distribution, is generally good within the statistical uncertainties.

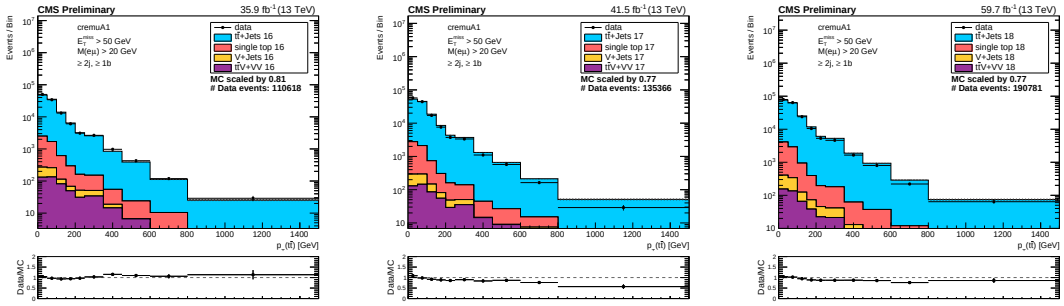

Figure 4.6: Distributions of $\mathrm{t\bar{t}}$ system p_{T}, approximated by the p_{T} of the system consists of the dilepton, two jets with highest b tag discriminant, and the $E_{\mathrm{T}}^{\mathrm{miss}}$, for the $\geq$1 b tag region of the eμ CR, for 2016 (left), 2017 (middle) and 2018 (right).

The large disagreement seen in 2017 and 2018 is eventually traced directly to the mismodeling (especially in $E_{\mathrm{T}}^{\mathrm{miss}}$) in the $\mathrm{t\bar{t}}$ simulation after the change in their Tune. Figure 4.8 shows comparison between the 3 years in the distributions of the $E_{\mathrm{T}}^{\mathrm{miss}}$, the $p_{\mathrm{T}}(\mathrm{t\bar{t}})$ and the number of jets, for both data and the total MC simulation, where the 2017 and 2018 data and MC are scaled to 35.9 fb^{-1} to match the amount of data collected or MC simulated for 2016. From the top row of the figure, we can see that observed data exhibit only little changes in the shape between the 2016 and the 2017–2018 data taking periods, and the small differences can be attributed to the running condition change (e.g. higher pile-up) and detector change (e.g. extra pixel layer). The small increase in $E_{\mathrm{T}}^{\mathrm{miss}}$ can be seen to reach around 10% just before 200 GeV but agreements are quickly restored

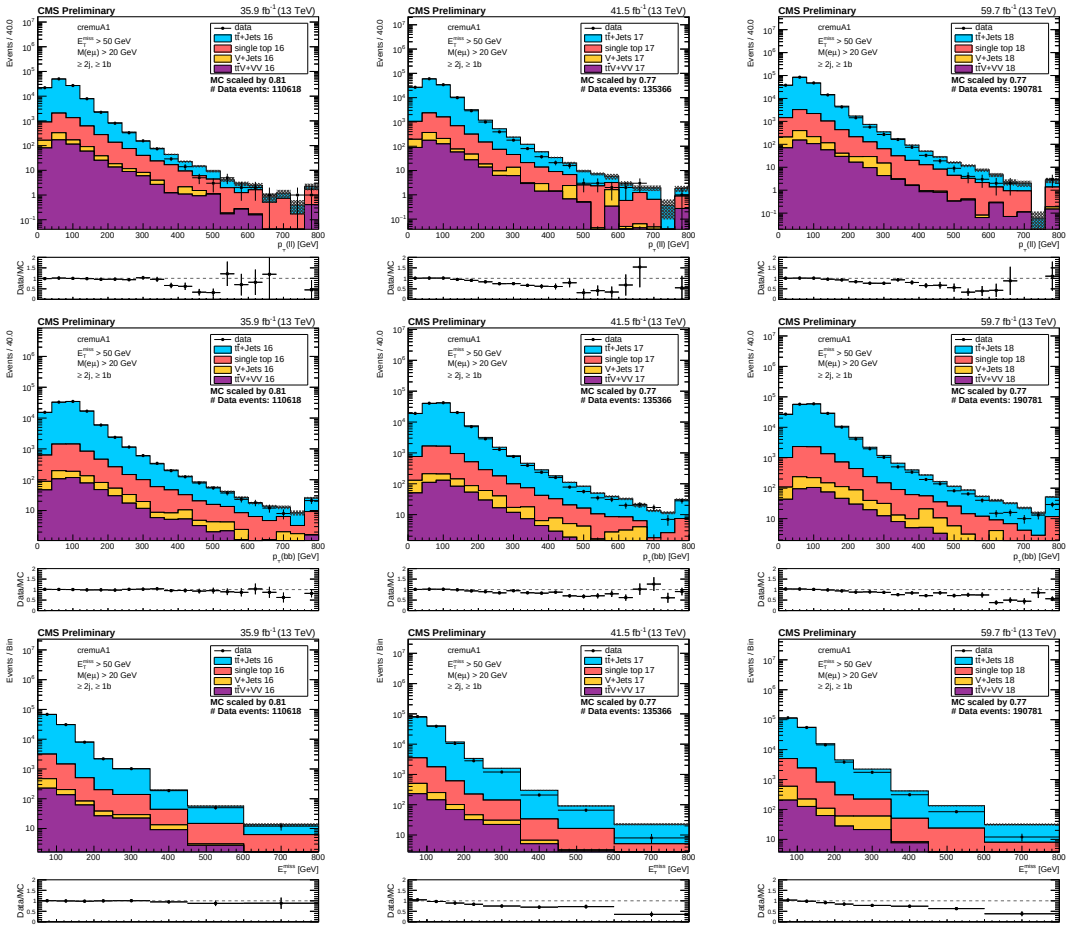

Figure 4.7: Distribution of p_{T} of the vector sum of the 2 leptons (top row), p_{T} of the vector sum of the 2 leading b jets in DeepCSV score (middle row), and $E_{\mathrm{T}}^{\mathrm{miss}}$ (bottom row) for 2016 (left column), 2017 (middle row) and 2018 (bottom row), in the eμ CR defined in Section 4.1.4.1 and with the extra requirement of $\geq$1 b tag to enhance the purity of the $\mathrm{t\bar{t}}$ contribution.

in high $E_{\mathrm{T}}^{\mathrm{miss}}$ region, where the contribution is dominated by the real $E_{\mathrm{T}}^{\mathrm{miss}}$. On the other hand, from the bottom row of the figure it can be seen that the 2017–2018 simulation, which is under a different Tune and almost purely dominated by the $\mathrm{t\bar{t}}$ contribution (its dominance can be read off from the number of b tag distribution in Figure 4.5 for $N_{\mathrm{b}} \geq 1$), shows a continuous increase in the $E_{\mathrm{T}}^{\mathrm{miss}}$ spectrum and eventually reaching a difference of 40% after $E_{\mathrm{T}}^{\mathrm{miss}} \geq 250\,\mathrm{GeV}$. This tell us that with a $E_{\mathrm{T}}^{\mathrm{miss}} \geq 250\,\mathrm{GeV}$

requirement, which is the case for our signal and control regions, we are getting as large as 40% over-prediction from the $t\bar{t}$ MC samples we use, even if they could have been demonstrating good agreement in low $E_{\mathrm{T}}^{\mathrm{miss}}$ ($<$50 GeV) regions.

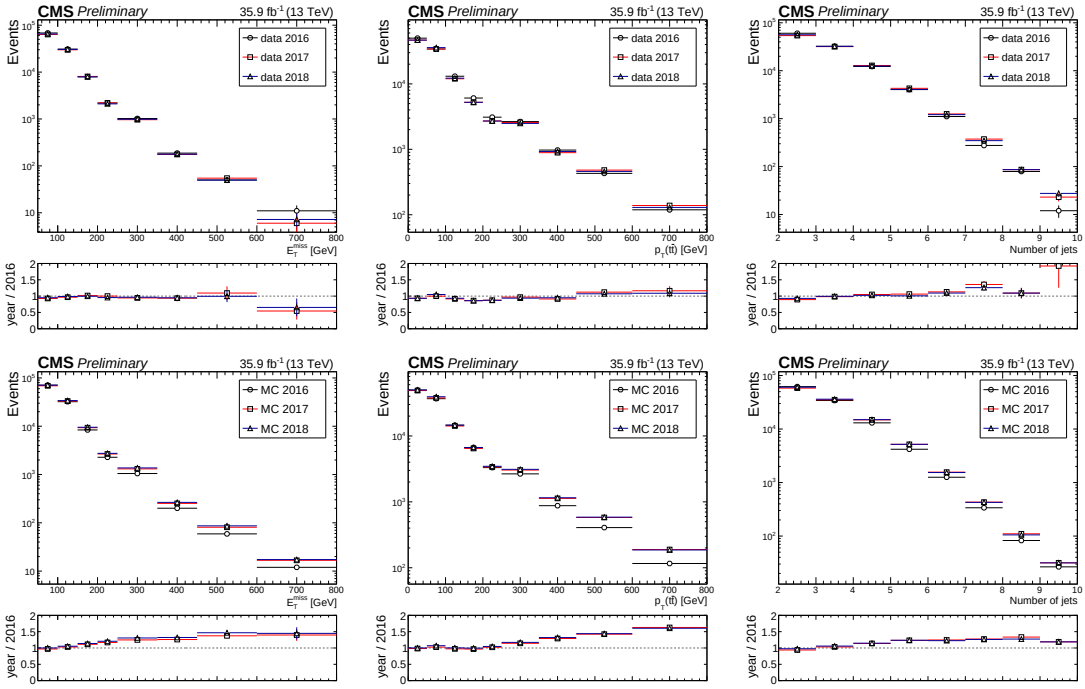

Figure 4.8: Comparison between distributions from 2016, 2017 and 2018 data (top row) and total MC (bottom), for $E_{\mathrm{T}}^{\mathrm{miss}}$ (left), $t\bar{t}$ system p_{T} (middle), and number of jets (right). The 2017 and 2018 data and MC are scaled to 35.9 fb^{-1} to match the amount of data collected or simulated in 2016. The $t\bar{t}$ MC events entering the 2016 distribution received the ISR correction scale factors described in Table 4.2.

In an attempt to correct for the $E_{\mathrm{T}}^{\mathrm{miss}}$ mismodeling from upstream, attempts were made trying to reweight the MC events to the observed data in terms of the $t\bar{t}$ system p_{T}, both in itself and also in each N_{j} bin. The $E_{\mathrm{T}}^{\mathrm{miss}}$ distribution after the reweighting were checked in the same eμ cross-check region. It was found that the disagreement between the data and MC could not be completely fixed. Similar studies are also performed over the NLO $t\bar{t}$ of dilepton final states. While in those samples, consistency among the 3

years are observed, some difference in the $t\bar{t}$ system p_T and the E_T^{miss} distribution remains.

Eventually, we decided to correct the E_T^{miss} for the $t\bar{t}$ modeling directly, using correction factors derived from the difference between data and MC observed in the eμ cross-check regions. Theses correction factors will only be applied to the $t\bar{t}$ dilepton events where E_T^{miss} extrapolation is deployed for the lost lepton background estimate.

The removed-lepton E_T^{miss} distribution for the eμ cross-check region with $N_b \geq 1$ is binned by different edges to mimic the E_T^{miss} binning in those signal regions that require E_T^{miss} extrapolation. The resulting distribution are shown in Figure 4.9, for a combined statistics from all 3 years corresponding to the integrated luminosity of $137.2\,fb^{-1}$, and the scale factors from the relevant E_T^{miss} bins are listed in Table 4.3. The scale factors takes only the shape difference between data and MC for the two neighboring E_T^{miss} bins, by first scaling the combined yields in the two individual bins from MC to the combined yields of the observed data, and the associated uncertainties are purely statistical and driven by the number of data events.

Table 4.3: Shape correction scale factors to apply to the removed-lepton E_T^{miss} distribution extrapolation in lost lepton background estimate, for $137.2\,fb^{-1}$ of the lost lepton estimates.

SR Label	E_T^{miss} [GeV]	Scale Factor	E_T^{miss} [GeV]	Scale Factor
A0	600–750	1.072 ± 0.155	>750	0.763 ± 0.236
B	450–700	1.022 ± 0.051	>700	0.681 ± 0.153
C	650–800	1.221 ± 0.221	>800	0.335 ± 0.195
E0	450–600	1.068 ± 0.056	>600	0.704 ± 0.092
G0	550–750	1.054 ± 0.105	>750	0.661 ± 0.205
H	250–500	1.007 ± 0.011	>500	0.785 ± 0.053
I	550–750	1.054 ± 0.105	>750	0.661 ± 0.205
J	550–750	1.054 ± 0.105	>750	0.661 ± 0.205

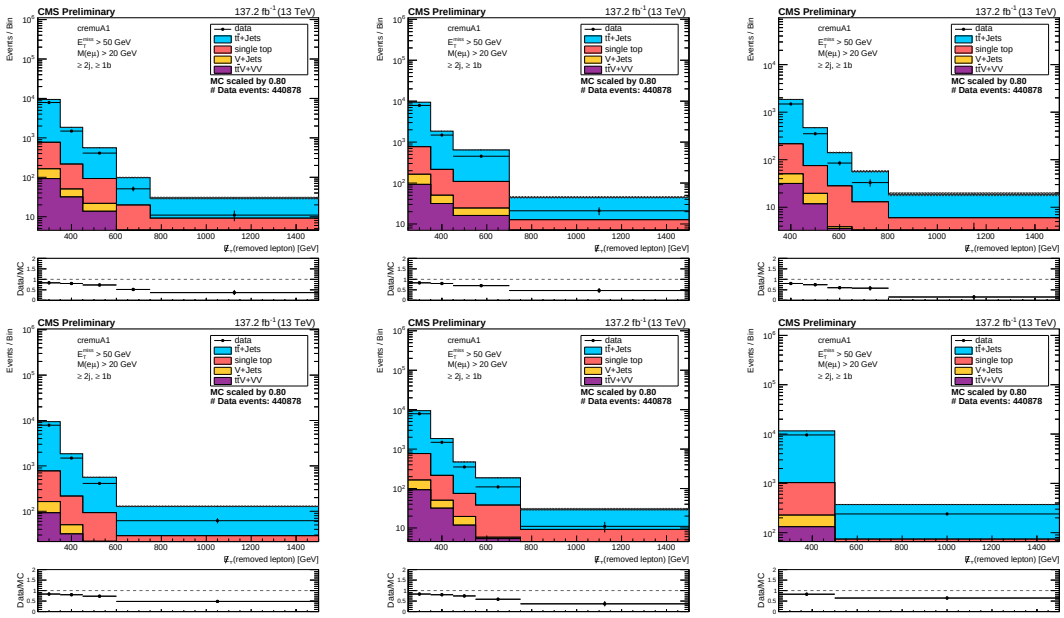

Figure 4.9: Example of different binning for the same distribution of removed-lepton $E_{\mathrm{T}}^{\mathrm{miss}}$ for the $\geq$1 b tag region of the eμ CR, for 137.2 fb^{-1}. The binning is to mimic standard search regions where $E_{\mathrm{T}}^{\mathrm{miss}}$ extrapolation is deployed for the lost lepton background estimate.

4.1.5 Yields in dilepton control region

The numbers related to the data-driven estimation for the lost lepton background in each individual signal and control regions are summarized in Table 4.4. They correspond to an integrated luminosity of 137.2 fb^{-1}, for observed data collected over the period of 2016–2018, and the MC samples generated with the similar running conditions. The observed yields from data and the expected yields from MC simulation for the raw dilepton control regions are also illustrated in Figure 4.10, with the stack histogram showing also the different background categories. In the figure, the CR bins where $E_{\mathrm{T}}^{\mathrm{miss}}$ extrapolation is performed are not combined, while in the data yields column in the table, they are combined to show a single yield and corresponding uncertainties. The $\mathrm{TF}_{\mathrm{CR}}^{\mathrm{SR}}$ column of

the table shows the transfer factors that are used to reweight the data yields in the CR to obtain the final prediction in the last column, and the values are also illustrated in Figure 4.11. They are calculated as the ratio between the lost lepton contribution in SR and the total SM backgrounds in the corresponding CR, both from MC simulation and taking into account the $E_{\mathrm{T}}^{\mathrm{miss}}$ extrapolation process.

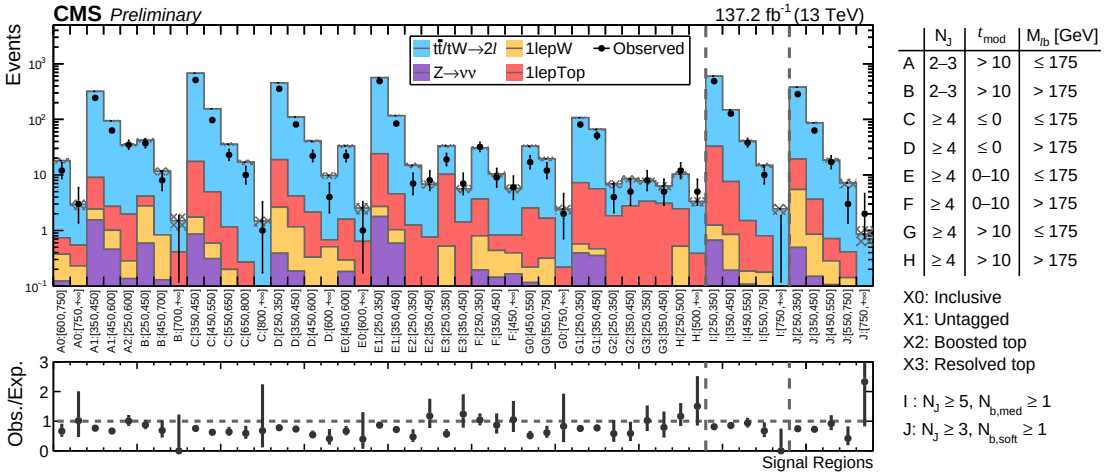

Figure 4.10: The observed and expected yields in Tables 4.4. The estimated SM contributions by MC simulation are shown as stacked histograms, with only statistical uncertainties of the MC are presented as shaded bands. SR labels are used for the topological selections and are explained on the right panel, and the numbers in the square brackets indicate the selection range on $E_{\mathrm{T}}^{\mathrm{miss}}$ in GeV.

4.1.6 Estimation of the systematic uncertainties

The sizes of the leading uncertainties are shown in Figure 4.12, and the list of all uncertainties that are considered are described as follows:

Statistical: There are 2 types of statistical error in the estimation process, the first is the uncertainties on the observed data in the individual dilepton CR ($N_{\ell\ell}^{\mathrm{CR}}$), and the

Table 4.4: The total event yields in the dilepton control regions for the integrated luminosity of 137.2 fb^{-1}, for the observed data recorded by the CMS detector over the data periods during 2016–2018, and the expected SM contributions from MC simulation correspond to the same amount of data and running conditions. Signal region labels A–J are used in place of the selection criteria over N_{b}, $N_{\text{b, soft}}$, t_{mod} and $M_{\ell\text{b}}$.

SR Label	$E_{\text{T}}^{\text{miss}}$ range [GeV]	Lost-ℓ in SR	Total Bkg CR	2ℓ Purity in CR	$\text{TF}_{\text{CR}}^{\text{SR}}$	Data CR	R_{CR}(Data/MC)	Prediction
A0	600–750	2.15 ± 0.6	18.07 ± 1.88	0.94 ± 0.09	$0.11^{+0.14}_{-0.07}$	15^{+5}_{-4}	0.71 ± 0.2	$1.6^{+0.5+0.5}_{-0.4-0.5}$
	≥750	0.43 ± 0.19	2.95 ± 0.61	0.94 ± 0.09	$0.02^{+0.03}_{-0.01}$			$0.26^{+0.09+0.16}_{-0.07-0.16}$
A1	350–450	59.55 ± 3.17	319.32 ± 7.22	0.97 ± 0.0	$0.19^{+0.2}_{-0.17}$	244^{+17}_{-16}	0.76 ± 0.05	$45.5^{+3.1+4}_{-2.9-4}$
	450–600	14.1 ± 1.51	94.23 ± 3.96	0.97 ± 0.01	$0.15^{+0.16}_{-0.14}$	63^{+9}_{-8}	0.67 ± 0.09	$9.4^{+1.3+0.9}_{-1.2-0.9}$
A2	250–600	4.51 ± 0.89	34.73 ± 2.4	0.94 ± 0.01	$0.13^{+0.15}_{-0.11}$	35^{+7}_{-6}	1.01 ± 0.18	$4.5^{+0.9+0.7}_{-0.8-0.7}$
B	250–450	7.54 ± 1.16	42.21 ± 3.89	0.9 ± 0.02	$0.18^{+0.21}_{-0.15}$	37^{+7}_{-6}	0.88 ± 0.17	$6.6^{+1.3+1.0}_{-1.1-1.0}$
	450–700	0.62 ± 0.32	11.65 ± 1.85	0.91 ± 0.13	$0.07^{+0.08}_{-0.05}$	$8^{+3.9}_{-2.8}$	0.61 ± 0.23	$0.55^{+0.27+0.12}_{-0.19-0.12}$
	≥700	0.4 ± 0.26	1.5 ± 0.51	0.91 ± 0.13	$0.01^{+0.01}_{-0.0}$			$0.07^{+0.03+0.05}_{-0.02-0.05}$
C	350–450	324.96 ± 7.56	677.91 ± 10.54	0.97 ± 0.0	$0.5^{+0.5}_{-0.4}$	512^{+24}_{-23}	0.76 ± 0.04	245^{+11+20}_{-11-20}
	450–550	76.2 ± 3.65	154.95 ± 5.03	0.97 ± 0.01	$0.5^{+0.5}_{-0.4}$	97^{+11}_{-10}	0.63 ± 0.07	48^{+5+4}_{-5-4}
	550–650	24.33 ± 2.11	35.71 ± 2.38	0.97 ± 0.02	$0.7^{+0.8}_{-0.6}$	23^{+6}_{-5}	0.64 ± 0.14	$15.7^{+4+1.9}_{-3.2-1.9}$
	650–800	10.15 ± 1.5	16.93 ± 1.79	0.98 ± 0.1	$0.6^{+0.7}_{-0.5}$	$11^{+4.4}_{-3.3}$	0.6 ± 0.19	$6.6^{+2.6+1.0}_{-2.0-1.0}$
	≥800	1.83 ± 0.35	1.46 ± 0.29	0.98 ± 0.1	$0.05^{+0.12}_{-0.01}$			$0.57^{+0.23+0.7}_{-0.17-0.7}$
D	250–350	184.55 ± 5.84	454.43 ± 8.62	0.96 ± 0.0	$0.4^{+0.4}_{-0.4}$	355^{+20}_{-19}	0.78 ± 0.04	144^{+8+10}_{-8-10}
	350–450	44.66 ± 2.86	110.22 ± 4.1	0.96 ± 0.01	$0.4^{+0.5}_{-0.4}$	81^{+10}_{-9}	0.73 ± 0.09	33^{+4+4}_{-4-4}
	450–600	16.47 ± 1.65	40.59 ± 2.65	0.95 ± 0.02	$0.41^{+0.46}_{-0.35}$	22^{+6}_{-5}	0.54 ± 0.12	$8.9^{+2.3+1.2}_{-1.9-1.2}$
	≥600	7.85 ± 1.16	9.76 ± 1.31	0.93 ± 0.03	$0.8^{+1.0}_{-0.6}$	$4^{+3.2}_{-1.9}$	0.41 ± 0.21	$3.2^{+2.5+0.7}_{-1.5-0.7}$
E0	450–600	9.34 ± 1.34	33.08 ± 2.44	0.94 ± 0.06	$0.26^{+0.29}_{-0.23}$	23^{+6}_{-5}	0.65 ± 0.14	$5.9^{+1.5+0.7}_{-1.2-0.7}$
	≥600	0.47 ± 0.2	2.53 ± 0.58	0.94 ± 0.06	$0.02^{+0.03}_{-0.01}$			$0.45^{+0.11+0.26}_{-0.09-0.26}$
E1	250–350	214.71 ± 6.08	564.54 ± 9.45	0.96 ± 0.0	$0.38^{+0.41}_{-0.35}$	490^{+23}_{-22}	0.87 ± 0.04	186^{+9+14}_{-8-14}
	350–450	35.6 ± 2.47	116.62 ± 4.28	0.96 ± 0.01	$0.31^{+0.33}_{-0.28}$	84^{+10}_{-9}	0.72 ± 0.08	$25.6^{+3.1+2.3}_{-2.8-2.3}$
E2	250–350	3.51 ± 0.72	14.85 ± 1.57	0.92 ± 0.03	$0.24^{+0.3}_{-0.17}$	$7^{+3.8}_{-2.6}$	0.47 ± 0.19	$1.7^{+0.9+0.5}_{-0.6-0.5}$
	350–450	2.06 ± 0.61	6.8 ± 1.09	0.89 ± 0.05	$0.3^{+0.43}_{-0.18}$	$8^{+3.9}_{-2.8}$	1.18 ± 0.46	$2.4^{+1.2+1.0}_{-0.8-1.0}$
E3	250–350	9.85 ± 1.2	33.24 ± 2.41	0.69 ± 0.04	$0.3^{+0.35}_{-0.24}$	19^{+5}_{-4}	0.57 ± 0.14	$5.6^{+1.6+1.0}_{-1.3-1.0}$
	350–450	2.11 ± 0.47	5.64 ± 0.93	0.75 ± 0.09	$0.37^{+0.49}_{-0.26}$	$7^{+3.8}_{-2.6}$	1.24 ± 0.51	$2.6^{+1.4+0.8}_{-1.0-0.8}$
F	250–350	9.96 ± 1.26	30.66 ± 2.16	0.88 ± 0.02	$0.33^{+0.37}_{-0.28}$	32^{+7}_{-6}	1.04 ± 0.2	$10.4^{+2.2+1.4}_{-1.8-1.4}$
	350–450	1.39 ± 0.44	10.39 ± 1.3	0.92 ± 0.04	$0.13^{+0.22}_{-0.05}$	$9^{+4.1}_{-2.9}$	0.87 ± 0.31	$1.2^{+0.6+0.7}_{-0.4-0.7}$
	≥450	0.51 ± 0.3	5.68 ± 1.03	0.86 ± 0.07	$0.09^{+0.25}_{-0.07}$	$6^{+3.6}_{-2.4}$	1.06 ± 0.47	$0.54^{+0.32+0.9}_{-0.22-0.9}$
G0	450–550	12.68 ± 1.59	32.99 ± 2.29	0.92 ± 0.02	$0.38^{+0.43}_{-0.34}$	17^{+5}_{-4}	0.52 ± 0.13	$6.5^{+2.0+0.8}_{-1.6-0.8}$
	550–750	4.09 ± 0.83	19.53 ± 1.77	0.92 ± 0.07	$0.19^{+0.25}_{-0.13}$	14^{+5}_{-4}	0.64 ± 0.18	$2.7^{+0.9+0.9}_{-0.7-0.9}$
	≥750	0.63 ± 0.27	2.4 ± 0.47	0.92 ± 0.07	$0.02^{+0.03}_{-0.01}$			$0.33^{+0.11+0.15}_{-0.09-0.15}$
G1	250–350	45.11 ± 2.84	107.24 ± 4.38	0.93 ± 0.01	$0.4^{+0.5}_{-0.4}$	81^{+10}_{-9}	0.76 ± 0.09	$34^{+4+3.2}_{-4-3.2}$
	350–450	24.1 ± 2.06	66.1 ± 3.36	0.92 ± 0.02	$0.36^{+0.41}_{-0.32}$	51^{+8}_{-7}	0.77 ± 0.11	$18.6^{+3.0+2.3}_{-2.6-2.3}$
G2	250–350	0.63 ± 0.39	6.88 ± 1.1	0.73 ± 0.08	$0.09^{+0.13}_{-0.06}$	$4^{+3.2}_{-1.9}$	0.58 ± 0.31	$0.37^{+0.29+0.14}_{-0.17-0.14}$
	350–450	1.39 ± 0.45	8.54 ± 1.24	0.68 ± 0.07	$0.16^{+0.19}_{-0.13}$	$5^{+3.4}_{-2.2}$	0.59 ± 0.28	$0.81^{+0.6+0.14}_{-0.35-0.14}$
G3	250–350	2.23 ± 0.57	7.81 ± 1.1	0.57 ± 0.07	$0.29^{+0.33}_{-0.24}$	$8^{+3.9}_{-2.8}$	1.02 ± 0.39	$2.3^{+1.1+0.4}_{-0.8-0.4}$
	350–450	0.99 ± 0.3	6.31 ± 1.07	0.52 ± 0.09	$0.16^{+0.19}_{-0.13}$	$5^{+3.4}_{-2.2}$	0.79 ± 0.38	$0.78^{+0.5+0.15}_{-0.34-0.15}$
H	250–500	3.21 ± 0.78	10.28 ± 1.31	0.79 ± 0.07	$0.2^{+0.27}_{-0.14}$	17^{+5}_{-4}	1.25 ± 0.33	$3.4^{+1.1+1.1}_{-0.8-1.1}$
	≥500	0.43 ± 0.2	3.32 ± 0.62	0.79 ± 0.07	$0.07^{+0.09}_{-0.04}$			$1.11^{+0.34+0.4}_{-0.27-0.4}$
I	250–350	494.62 ± 9.24	599.64 ± 9.79	0.95 ± 0.0	$0.8^{+0.9}_{-0.8}$	488^{+23}_{-22}	0.81 ± 0.04	403^{+19+35}_{-18-35}
	350–450	125.7 ± 4.66	148.48 ± 4.9	0.95 ± 0.01	$0.8^{+0.9}_{-0.8}$	127^{+12}_{-11}	0.86 ± 0.08	108^{+10+11}_{-10-11}
	450–550	33.34 ± 2.39	40.56 ± 2.61	0.96 ± 0.01	$0.8^{+1.0}_{-0.7}$	38^{+7}_{-6}	0.94 ± 0.16	31^{+6+6}_{-5-6}
	550–750	19.23 ± 1.93	14.85 ± 1.49	0.95 ± 0.08	$1.1^{+1.3}_{-0.9}$	$10^{+4.3}_{-3.1}$	0.58 ± 0.19	$10.9^{+5+2.1}_{-3.4-2.1}$
	≥750	2.68 ± 0.54	2.44 ± 0.53	0.95 ± 0.08	$0.18^{+0.27}_{-0.09}$			$1.8^{+0.8+0.9}_{-0.6-0.9}$
J	250–350	268.33 ± 7.36	379.93 ± 8.84	0.95 ± 0.01	$0.7^{+0.8}_{-0.6}$	284^{+18}_{-17}	0.75 ± 0.05	201^{+13+17}_{-12-17}
	350–450	52.52 ± 3.25	86.52 ± 4.17	0.96 ± 0.01	$0.6^{+0.7}_{-0.5}$	63^{+9}_{-8}	0.73 ± 0.1	38^{+5+4}_{-5-4}
	450–550	12.49 ± 1.7	18.47 ± 1.85	0.96 ± 0.01	$0.7^{+0.8}_{-0.6}$	17^{+5}_{-4}	0.92 ± 0.24	$11.5^{+3.5+1.6}_{-2.8-1.6}$
	550–750	5.59 ± 1.11	7.16 ± 1.37	0.95 ± 0.16	$0.7^{+0.9}_{-0.5}$	$5^{+3.4}_{-2.2}$	0.62 ± 0.3	$3.5^{+2.3+1.2}_{-1.5-1.2}$
	≥750	0.59 ± 0.39	0.85 ± 0.33	0.95 ± 0.16	$0.08^{+0.15}_{-0.02}$			$0.41^{+0.28+0.33}_{-0.18-0.33}$

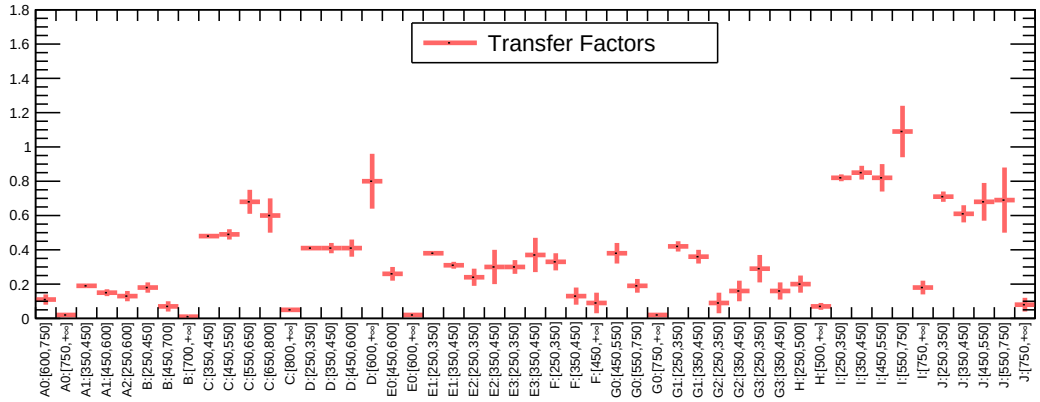

Figure 4.11: The transfer factors calculated as the ratio between each SR and their corresponding control regions, with the $E_{\mathrm{T}}^{\mathrm{miss}}$ extrapolation factors included.

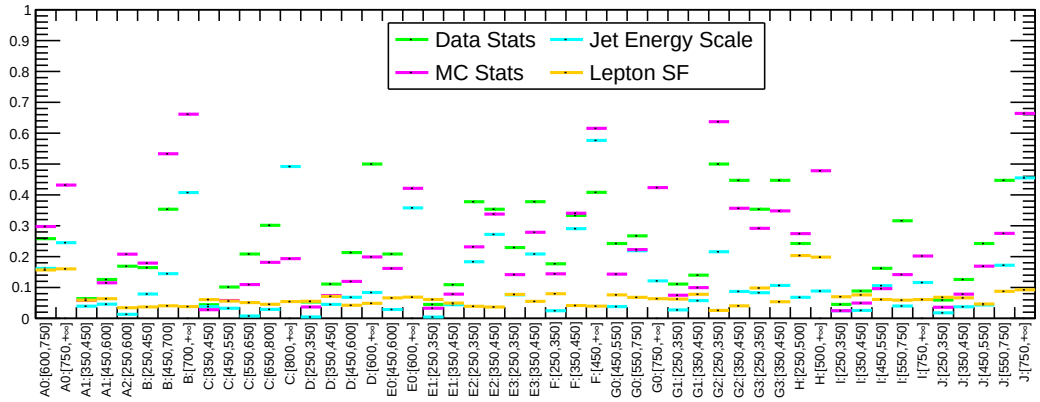

Figure 4.12: The prefit sizes of variations in the lost lepton estimation by the statistical uncertainties and the leading systematic uncertainties.

second one is on the transfer factors $M^{\mathrm{SR}}_{\text{lost-}\ell}/M^{\mathrm{CR}}_{\ell\ell}$ derived from the MC simulation yields in both the SR and the dilepton CR. The uncertainty on the transfer factor is mainly driven by the small number of simulated events in the SR. Both type of statistical uncertainties are the largest uncertainties of the estimation, and can go up to 60% in some low statistic SR.

Lepton scale factor: Uncertainties on the lepton reconstruction and selection efficiencies have the second largest impact on the lost lepton background estimation. The uncertainties by themselves are small (1–5%), but is magnified to about 3–10% as in the final impact. To first order, the square of these uncertainties enters the ratio $M^{\mathrm{SR}}_{\text{lost-}\ell}/M^{\mathrm{CR}}_{\ell\ell}$ as it appears in both the numerator and the denominator of the transfer factors in the anti-correlated way.

Jet Energy Scale: This uncertainty is estimated by applying different corrections on jets to model the migration of events, in the number of jets category, due to jets going in and out of the p_{T} acceptance, or in the $E_{\mathrm{T}}^{\mathrm{miss}}$ bins, due to the change in the value of $E_{\mathrm{T}}^{\mathrm{miss}}$. The jet energy scale variation affects the numerator and denominator in the same way and are canceled in the ratio $M^{\mathrm{SR}}_{\text{lost-}\ell}/M^{\mathrm{CR}}_{\ell\ell}$ to the first order.

CR2l trigger efficiencies: The measurement of the trigger efficiencies in the dilepton control region has been described in Section 3.2 and the uncertainties on the measurement from the `JetHT` data set shown in Figure 3.5. are applied as variations on the event count of $M^{\mathrm{CR}}_{\ell\ell}$. The final size of this uncertainty on the estimation is less than 2%.

ISR: The ISR-N_{j} reweighting scale factors derived by the SUSY POG are applied to the 2016 signal and $\mathrm{t\bar{t}}$ MC samples, to correct for the jet multiplicity spectrum in these samples based on the number of jets tagged as ISR jet by generator object matching. To determine the ISR uncertainty, the scale factors are varied by their uncertainties, which is about 4% when there is only 1 ISR jet, and reaches 26% when there are 6 or more ISR

jets. The 2017 and 2018 $t\bar{t}$ MC samples, however, are produced with a different `Tune`, and the data/MC agreement on the native N_j distribution is good enough. Nevertheless, we are varying the left-over difference from unity observed in the N_j distribution with $N_j > 2$ from the eμ cross-check region described in Section 4.1.4, which also reaches around 20% when there are 6 or more ISR jets, in place of the uncertainties for ISR-N_j scale factors. The ISR uncertainty also cancels to the first order in the transfer factor and final impact from this uncertainty is usually less than 1%.

E_T^{miss} resolution: The fake E_T^{miss} contribution in the simulation is corrected by scale factors obtained from a single photon control region, and the correction is also varied by the uncertainties on those scale factors on an event by event basis to model event migration effects. This effect also cancels in the ratio $M^{SR}_{\text{lost-}\ell}/M^{CR}_{\ell\ell}$ to first order except when a E_T^{miss} extrapolation is applied, though in those cases the fake E_T^{miss} contribution is very small. The final impact from this uncertainty is usually below 1% but can reach 10% in some bins.

E_T^{miss} in $t\bar{t}$/tW system: This uncertainty applies only to bins where the E_T^{miss} extrapolations are performed, and is specific only to the lost lepton background estimation. The difference between data and simulation in the shape of the E_T^{miss} spectrum of the $t\bar{t}$/tW system is normally canceled out in the the ratio $M^{SR}_{\text{lost-}\ell}/M^{CR}_{\ell\ell}$ that we trust, except for the bins where the E_T^{miss} extrapolation is performed. In these bins the E_T^{miss} extrapolation factor uses the shape of the removed-lepton E_T^{miss} from MC. The E_T^{miss} extrapolation

scale factors described in Table 4.3 are varied by their statistical uncertainties from their measurement in an anti-correlated way between the neighboring $E_{\mathrm{T}}^{\mathrm{miss}}$ bins where the $E_{\mathrm{T}}^{\mathrm{miss}}$ extrapolation is performed.

b tagging scale factors: There are 2 uncorrelated uncertainties in this category. We vary the heavy/light flavor component of the b tagging scale factors, provided by the BTV POG, by their uncertainties in the measurement. The uncertainty from b tagging scale factors in the lost lepton estimation cancels in the ratio $M_{\text{lost-}\ell}^{\mathrm{SR}}/M_{\ell\ell}^{\mathrm{CR}}$ to the first order and the final impact is usually less than 2%.

τ scale factor: The hadronic τs considered in this analysis is excluding the τs that are already forming an isolated track that would veto the event, and the compensated τ scale factors are applied to $\mathrm{t\bar{t}}$ events with hadronic τ in the final states but pass both the isotrack veto and the hadronic τ veto, to correct for the inefficiencies for τ identification. The τ scale factors provided by the Tau POG, and the variation in those scale factors become the τ scale factor uncertainty. The impact from this uncertainty on the lost lepton estimate usually has less than 1% impact in the final estimation.

Pile-up reweighting: The variation in the lost lepton estimation induced by the variation of the pile-up weights described in Section 3.3.2. The effect on the lost lepton estimate is small as the lost lepton background consist of genuine $E_{\mathrm{T}}^{\mathrm{miss}}$, and it also cancels to the first order in the transfer factor.

PDF variation: The variations in the parton distribution function in the simulation, and are parameterized as different weights for an event. We take the average of 100 different PDF variations stored, and use the standard deviation of this average to vary the acceptance on the simulation. This uncertainty cancels in the ratio $M^{\mathrm{SR}}_{\text{lost-}\ell}/M^{\mathrm{CR}}_{\ell\ell}$ to first order.

α_s **variation:** The QCD scale of the event is varied in the simulation, and reflected as different weights of the event. This uncertainty cancels in the ratio $M^{\mathrm{SR}}_{\text{lost-}\ell}/M^{\mathrm{CR}}_{\ell\ell}$ to first order.

Q^2 **variation:** The largest two variations in renormalization and factorization scale are taken as an envelope, but only the change in the acceptance is taken as uncertainty. This uncertainty is the largest among the theory uncertainties though it also cancels in the ratio $M^{\mathrm{SR}}_{\text{lost-}\ell}/M^{\mathrm{CR}}_{\ell\ell}$ to first order.

L1 prefiring: The scale of the impact from the L1 prefiring effect on the 2016 and 2017 simulation is varied. This uncertainty cancels to first order in the ratio $M^{\mathrm{SR}}_{\text{lost-}\ell}/M^{\mathrm{CR}}_{\ell\ell}$.

4.2 One lepton background with lepton from W

The one lepton background from W refers to the physics processes that produce a single lepton in the prompt final state, and this lepton is not from a top quark decay. W+jets is the single largest contribution to this category. Implicitly, this contain all

SM processes with a W boson from direct production as well as some ISR/FSR jets, except for those that also contain a $Z \to \nu\bar{\nu}$ decay (e.g. the WZ process) that would be categorized into the $Z \to \nu\bar{\nu}$ category and discussed in Section 4.3.2. In these events, the neutrino from the $W \to \ell\nu$ process provides genuine source of E_T^{miss}, pushing the events to pass the $E_T^{miss} > 250\,GeV$ requirement when the W boson receives a moderate boost from the jets it is recoiling against. While the general $W \to \ell\nu$ background is heavily suppressed by the preselection requirements of $M_T > 150\,GeV$, a small portion from off-shell W bosons can still survive and make its way into our signal regions. It can still be a large source of background given the huge production cross section (around 20 nb) of W boson at the LHC compared to the signal and other background processes. In signal regions with $M_{\ell b} > 175\,GeV$, W+jets can be the leading contribution of all the SM backgrounds.

Another barrier for the W + jets process to enter the signal regions is the b tag requirement. As the jets in the W+jets process are mostly light-flavor jets, the W+jets events can cross this barrier by either having a misidentified b tag (with $\sim 1\%$ mistag rate per jet) or in the case of having an associated $b\bar{b}$ production. In fact, W+ $b\bar{b}$ events contribute more than 80% of the W+jets events in signal regions with $M_{\ell b} > 175\,GeV$. This can be seen in Figure 4.13 for the check by simulation about the fraction W+ $b\bar{b}$ events among the W+jets events in all SRs, or Figure 4.14 for the parton source of the jets that also tell us charm quark jets make up most of the fake b-tagged jets.

In spite of this, we expect the general W+jets events, that feature light-flavor jets in

the final state and fail the b tag requirement, to share the same final state kinematics as those that enter the SR. We can make use of these events to estimate the W+jets background in the SR in a data-driven way.

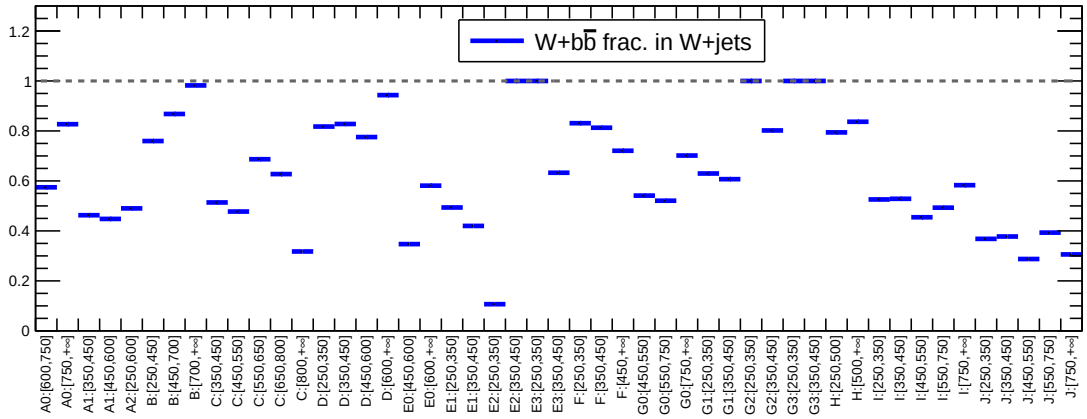

Figure 4.13: Fraction of W+$b\bar{b}$ in all the W+jets events, analyzed in individual signal regions. The SR labels defined in Section 3.4 are used in place of the selections criteria over N_{b}, $N_{\mathrm{b,\,soft}}$, t_{mod} and $M_{\ell\mathrm{b}}$, and the numbers in the square bracket indicates the $E_{\mathrm{T}}^{\mathrm{miss}}$ ranges.

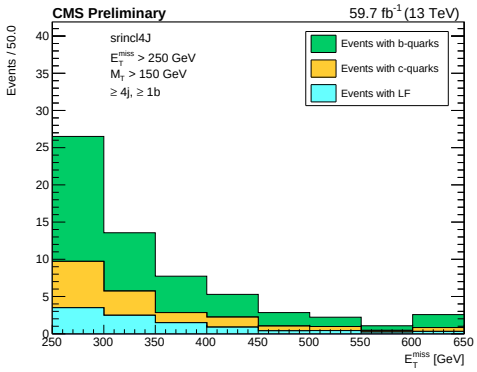

Figure 4.14: Generator truth information from the W+jets MC on the parton source of jets, in baseline signal region selection and ≥4 jets.

4.2.1 Overview of the estimation method

Similarly to the method described for the lost lepton estimates, in most of the signal regions, the W+jets background estimates are obtained from a control sample of events with the same selections except for a b-tagged jet veto. The relation is summarized in Equation 4.3

$$N_{\geq 1\mathrm{b}}^{\mathrm{SR}} = N_{0\mathrm{b}}^{\mathrm{CR}} \times \frac{M_{\geq 1\mathrm{b}}^{\mathrm{SR}}}{M_{0\mathrm{b}}^{\mathrm{CR}}} \times \left(\frac{M_{0\mathrm{b}}^{\mathrm{CR},\ E_{\mathrm{T}}^{\mathrm{miss}}\ \mathrm{bin}}}{M_{0\mathrm{b}}^{\mathrm{CR,\ comb}}} \right) \tag{4.3}$$

In the equation, the label N represents the event count for the observed data in SR or CR, and M represents the expected yields from MC for the SR or CR bin. The last term is the extrapolation factor and it is only present in the few bins where the $E_{\mathrm{T}}^{\mathrm{miss}}$ extrapolation is employed.

For signal regions where at least one top tag is required, however, the data-driven method can not be applied. The presence of a b quark is an important feature of the top decay, while on the other hand, having a top tag in the event also implies the presence of a b tag in the event as well. This means that the top tag requirement is in conflict with the 0b requirement for the CR, and there will only be very few expected events in the corresponding CR, making a CR to SR transfer impossible. Furthermore, correlation between the SR selection variable (in this case, the top tag) and the number of b tags should be avoided in general, as it is defeating the assumption that the events in SR and 0b CR have similar final state kinematics and differ only by the number of b tags.

Fortunately, the top tags themselves are very efficient in rejecting the W+jets in the SR, and making them less important backgrounds in these signal regions so that

estimating them directly from simulation becomes a viable option. From Figure 4.1 it can be seen that W+jets are in general contributing less than 15% in regions where at least one top tag is required (A2, E2, G2, E3, G3). The W+jets backgrounds for these signal regions are therefore estimated directly from the MC simulation, and the numbers of the final prediction for these regions can be found directly in Table 5.1 of the final results. They are since dropped from the following discussions below, that focus on the data-driven method.

4.2.2 Construction of the 0b control region

For the construction of the 0b control region, the following modifications are applied to the signal region selections as summarized in Section 3.3.3

- Require the event to contain 0 b-tagged jet, based only on the *medium* WP of the DeepCSV score uniformly for all signal regions. This applies to all standard search regions and the two dedicated corridor search regions.

- For the dedicated W corridor search regions, where the b requirement was placed on the soft b object, the 0b control region for them requires that there is no soft b object and no b-tagged jet in the event at the same time.

- Since there's no b-tagged jet, the $M_{\ell \mathrm{b}}$ variable is calculated with the jet that has the highest DeepCSV score in the event.

The kinematic distributions in the 0b CR from the simulation and observed data after

the baseline selections are shown in Fig 4.15, for the full amount of observed data and MC simulation, taken/generated over the year 2016–2018, corresponding to an integrated luminosity of 137.2 fb^{-1}. There is scale of 1.05 applied to the MC events, in order to allow a clearer comparison in the shapes of the distributions between data and MC under the same total normalization.

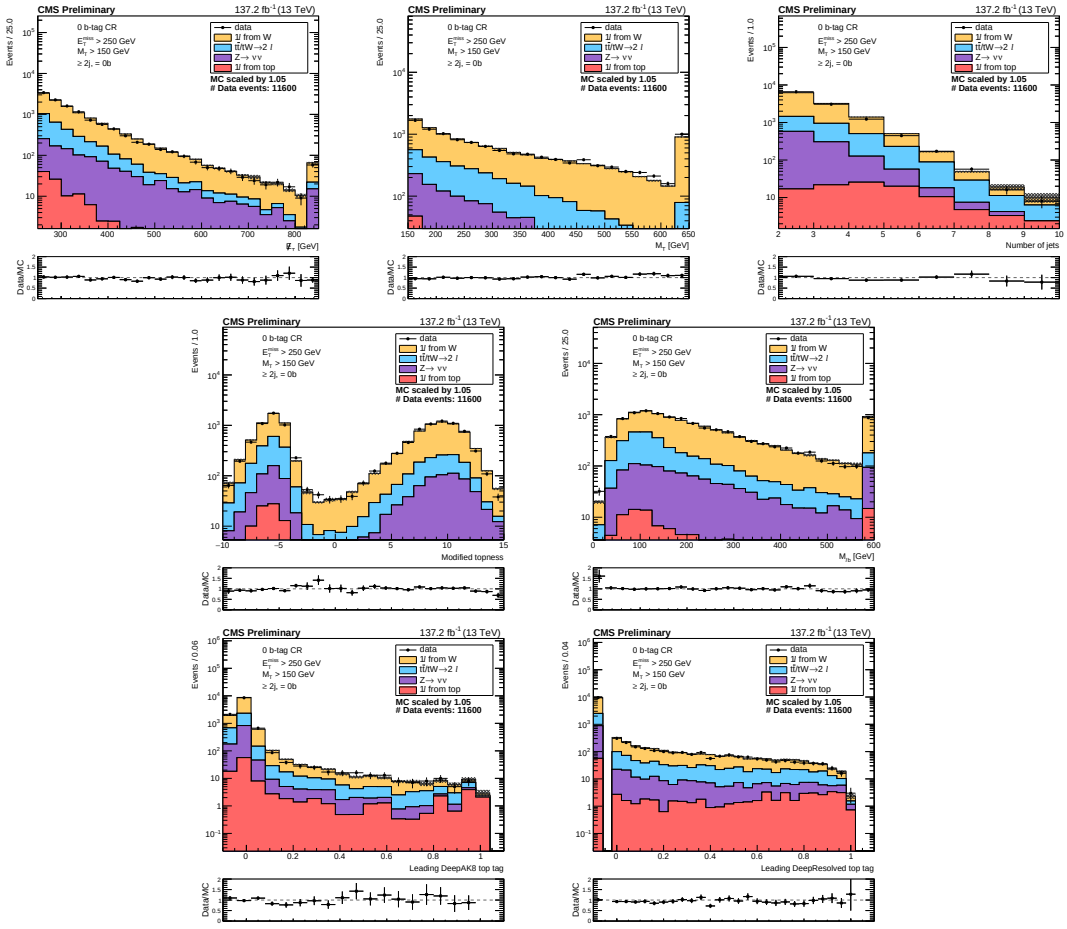

Figure 4.15: Kinematic distributions in the 0b CR from the simulation and observed data after the baseline selections that are described in Section 4.2.2. The observed data are collected over the period of 2016–2018, corresponding to an integrated luminosity of 137.2 fb^{-1}. The stacked histograms showing the SM background, similar to those described in Section 2.3, are first scaled to the same amount of luminosity, and then further scaled by 1.05 to have the same integration as the observed data events, to allow a better comparison in the shape. In each distribution, the rightmost bin also includes the overflow events.

Table 4.5 listed the 0b control region bins where he $E_{\mathrm{T}}^{\mathrm{miss}}$ extrapolation is performed. Unlike the case in the lost lepton estimate, no extra uncertainties are assigned regarding the $E_{\mathrm{T}}^{\mathrm{miss}}$ shape since no obvious disagreement between data and MC is seen in the $E_{\mathrm{T}}^{\mathrm{miss}}$ distribution of the 0b control region.

Table 4.5: Search regions where the corresponding 0b control regions are combined when estimating the W+jets background.

Label	Selection			$p_{\mathrm{T}}^{\mathrm{miss}}$ bins [GeV]	
C	$\geq$4 jets,	$t_{\mathrm{mod}} \leq 0$,	$M_{\ell \mathrm{b}} \leq 175\,\mathrm{GeV}$	650–800	>800
E0	$\geq$4 jets,	$0 < t_{\mathrm{mod}} \leq 10$,	$M_{\ell \mathrm{b}} \leq 175\,\mathrm{GeV}$	450–600	>600
G0	$\geq$4 jets,	$t_{\mathrm{mod}} > 10$,	$M_{\ell \mathrm{b}} \leq 175\,\mathrm{GeV}$	550–750	>750

The validity of the usage of other selection variables involving b-tagged jets should also be checked for possible difference between the SR selection and the 0b selection. The most important one is $M_{\ell \mathrm{b}}$. In the 0b control region, since there's no b-tagged jet, the jet with the highest DeepCSV score is used for calculating the $M_{\ell \mathrm{b}}$ variable. There are two questions to be answered regarding the W+jets events in SR and those in the 0b CR. The first one is whether the W+ $\mathrm{b\bar{b}}$ events, which consists of 50–60% in lower $E_{\mathrm{T}}^{\mathrm{miss}}$ SRs and up to 100% in high $E_{\mathrm{T}}^{\mathrm{miss}}$ SRs, share a similar $M_{\ell \mathrm{b}}$ distribution as the normal W+jets events. The second one is whether the choice of b leg in the $M_{\ell \mathrm{b}}$ definition, which is the closest b-tagged jet for events in the SR and could be a random choice among all jets for W+jets events in the CR, creating a difference in the $M_{\ell \mathrm{b}}$ distribution. We can use this information to decide whether the transfer factor can be constructed only on the b tag efficiency or in a more complicated way.

Figure 4.16 shows the comparison in the $M_{\ell \mathrm{b}}$ shapes from the simulated W+jets events between the 0b CR and the SR, covering the inclusive baseline region ($\geq$2 jets), and the

actual signal regions (2–3 jets with $t_{\mathrm{mod}} > 10$ or $\geq$4 jets). The W+b$\bar{\mathrm{b}}$ contributions in the SR are also plotted separately, to investigate if there are any shape differences caused by the W+ b$\bar{\mathrm{b}}$ kinematics. Although we have found good agreement between the $M_{\ell\mathrm{b}}$ shape between the $\geq$1b tag and 0b tag control samples in a lower $E_{\mathrm{T}}^{\mathrm{miss}}$ sideband or the high $E_{\mathrm{T}}^{\mathrm{miss}}$ but lower M_{T} and lower N_{j} control sample [29], this newly conducted check shows that there are differences in the $M_{\ell\mathrm{b}}$ distribution between SR and CR selections and the differences start appearing when we specifically require $t_{\mathrm{mod}} > 10$ or $\geq$4 jets. These differences are absorbed into the transfer factors, which are derived from the simulation, but this also mean that the transfer factors do rely on the MC modeling of the $M_{\ell\mathrm{b}}$ shape, and a specific uncertainty should be assigned to account for any possible mismodeling of $M_{\ell\mathrm{b}}$ from simulation, and a reasonable choice can be half of the difference between the inclusive $M_{\ell\mathrm{b}}$ distribution in SR and CR for the 2 different jet categories (as shown in Figure 4.16 middle and right), anti-correlated between the low and high $M_{\ell\mathrm{b}}$ search regions.[†] It should be noted that part of this uncertainty is already partially covered by the W+b$\bar{\mathrm{b}}$ cross section uncertainty, as the difference in $M_{\ell\mathrm{b}}$ shape can be seen correlated with the W+ b$\bar{\mathrm{b}}$ events to a certain extent.

[†]The checks for $M_{\ell\mathrm{b}}$ in 2–3 jets with $t_{\mathrm{mod}} > 10$ or $\geq$4 jets are performed after the publication of this analysis and the $M_{\ell\mathrm{b}}$ shape uncertainty is not included in the published version of this analysis. Despite this, we have performed a dedicate check with this uncertainty included, and it is shown that the impact on the final result from adding this uncertainty is very small.

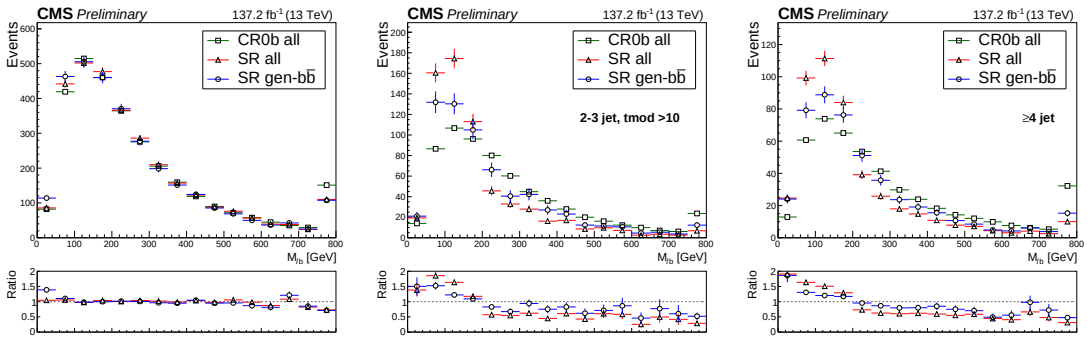

Figure 4.16: Validation of the $M_{\ell \mathrm{b}}$ shapes by the simulated W+jets events between the 0b CR (green), the SR (blue), and the W+ $\mathrm{b\bar{b}}$ contributions in SR (red) for the baseline selection (left), the baseline plus 2–3 jets and $t_{\mathrm{mod}} > 10$ (middle), or the baseline plus $\geq$4 jets.

4.2.3 Yields in the 0b control region

The numbers related to the data-driven estimation for the one lepton from W background in each individual signal and control regions are summarized in Table 4.6. The numbers correspond to an integrated luminosity of 137.2 fb^{-1}, for observed data collected over the period of 2016–2018, and the MC samples generated with the similar running conditions. The observed data and the expected yields from MC simulation for the raw 0b control regions are also illustrated in Figure 4.17, with the stacked histogram showing also the different background categories. In the figure, the CR bins where the $E_{\mathrm{T}}^{\mathrm{miss}}$ extrapolation is performed are not combined, while in the data yields column in the table, they are combined to show a single yield and corresponding uncertainties. The $\mathrm{TF}_{\mathrm{CR}}^{\mathrm{SR}}$ column shows the transfer factors that are used to reweight the data yields in the CR to obtain the final prediction in the last column, and their values are also illustrated in Figure 4.18. They are calculated as the ratio between the W+jets contribution in SR and the total SM backgrounds in the corresponding CR, both from MC simulation and taking

into account the $E_{\mathrm{T}}^{\mathrm{miss}}$ extrapolation process. The W+jets purity in CR, indicating the fractional contribution from W+jets among the total background in the control region, does not enter the prediction directly, but is an important indication of the robustness of the estimation. Half of the distance from unity is assigned as an extra uncertainty on the final prediction.

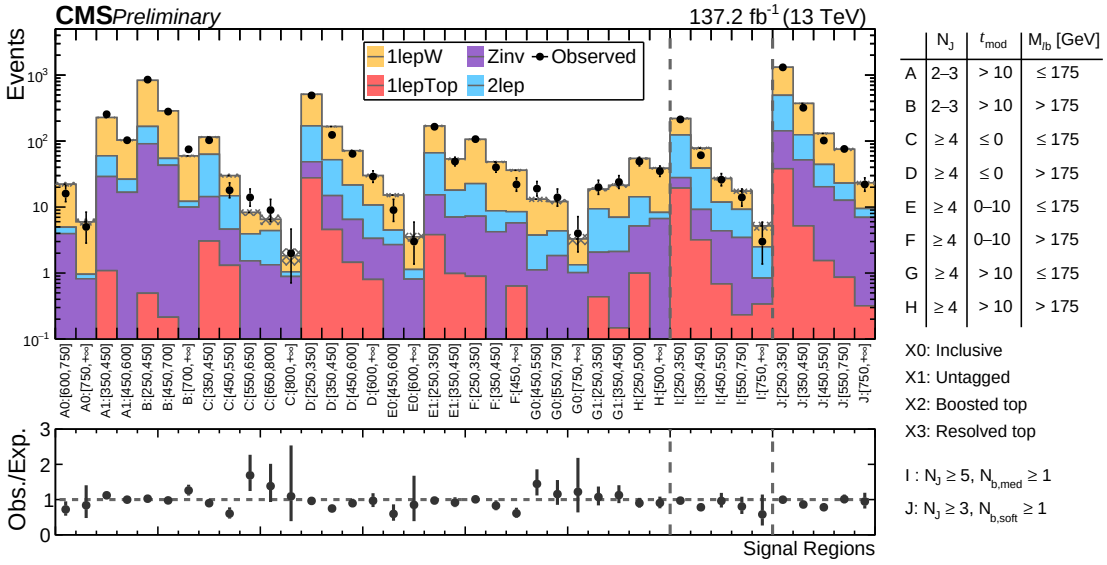

Figure 4.17: The graphical representation of the observed and expected yields in individual 0b control regions. The estimated SM contributions by MC simulation are shown as stacked histograms, with only statistical uncertainties of the MC are presented as shaded bands. SR labels are used for the topological selections and are explained on the right panel, and the numbers in the square brackets indicates the selection range on $E_{\mathrm{T}}^{\mathrm{miss}}$ in GeV. The raw CR are not combined for the $E_{\mathrm{T}}^{\mathrm{miss}}$ extrapolation process.

4.2.4 Estimation of the systematic uncertainties

The relative sizes of the leading uncertainties for the are shown in Figure 4.19, and the list of all uncertainties that are considered are described as follows:

Table 4.6: The inputs and the final prediction of the one lepton from W background in all the signal and 0b tag control regions where the data-driven method is employed. The numbers correspond to the full data or MC simulation correspond to an integrated luminosity of 137.2 fb^{-1}. Signal region labels A–H are used in place of the selection criteria over N_{b}, $N_{\text{b, soft}}$, t_{mod} and $M_{\ell\text{b}}$.

SR Label	$E_{\text{T}}^{\text{miss}}$ [GeV]	W+jets in SR	Total Bkg CR	W+jets Purity in CR	$\text{TF}_{\text{CR}}^{\text{SR}}$	Data CR	R_{CR}(Data/MC)	Prediction
A0	600–750	1.54 ± 0.19	22.19 ± 1.69	0.78 ± 0.04	$0.07^{+0.09}_{-0.05}$	16^{+5}_{-4}	0.72 ± 0.19	$1.11^{+0.35+0.4}_{-0.27-0.4}$
	≥750	0.44 ± 0.1	5.96 ± 0.71	0.84 ± 0.08	$0.07^{+0.11}_{-0.03}$	$5^{+3.4}_{-2.2}$	0.84 ± 0.39	$0.37^{+0.25+0.2}_{-0.16-0.2}$
A1	350–450	14.66 ± 0.62	227.42 ± 4.71	0.74 ± 0.01	$0.06^{+0.09}_{-0.04}$	255^{+17}_{-16}	1.12 ± 0.07	$16.4^{+1.1+5}_{-1.0-5}$
	450–600	7.34 ± 0.48	103.24 ± 3.86	0.74 ± 0.02	$0.07^{+0.09}_{-0.05}$	103^{+11}_{-10}	1.0 ± 0.11	$7.3^{+0.8+2.3}_{-0.7-2.3}$
B	250–450	20.27 ± 0.77	832.91 ± 15.46	0.8 ± 0.01	$0.02^{+0.06}_{--0.01}$	854^{+30}_{-29}	1.03 ± 0.04	$20.8^{+0.7+31}_{-0.7-31}$
	450–700	6.69 ± 0.38	286.72 ± 4.76	0.81 ± 0.01	$0.02^{+0.04}_{-0.01}$	280^{+18}_{-17}	0.98 ± 0.06	$6.5^{+0.4+4}_{-0.4-4}$
	≥700	1.56 ± 0.2	59.55 ± 2.49	0.8 ± 0.03	$0.03^{+0.04}_{-0.01}$	75^{+10}_{-9}	1.26 ± 0.15	$1.96^{+0.25+1.1}_{-0.23-1.1}$
C	350–450	10.88 ± 1.23	114.78 ± 3.86	0.45 ± 0.02	$0.09^{+0.13}_{-0.06}$	103^{+11}_{-10}	0.9 ± 0.09	$9.8^{+1.1+3.3}_{-1.0-3.3}$
	450–550	3.06 ± 0.34	29.94 ± 1.93	0.51 ± 0.03	$0.1^{+0.13}_{-0.07}$	18^{+5}_{-4}	0.6 ± 0.15	$1.8^{+0.5+0.5}_{-0.4-0.5}$
	550–650	1.07 ± 0.17	8.29 ± 0.92	0.53 ± 0.06	$0.13^{+0.19}_{-0.07}$	14^{+5}_{-4}	1.69 ± 0.49	$1.8^{+0.6+0.8}_{-0.5-0.8}$
	650–800	0.54 ± 0.12	6.51 ± 1.13	0.35 ± 0.02	$0.08^{+0.1}_{-0.05}$	$11^{+4.4}_{-3.3}$	1.32 ± 0.44	$0.87^{+0.35+0.27}_{-0.26-0.27}$
	≥800	0.31 ± 0.08	1.83 ± 0.52	0.35 ± 0.02	$0.02^{+0.03}_{-0.01}$			$0.25^{+0.1+0.11}_{-0.07-0.11}$
D	250–350	39.57 ± 2.68	511.2 ± 10.88	0.67 ± 0.01	$0.08^{+0.1}_{-0.05}$	492^{+23}_{-22}	0.96 ± 0.05	$38.1^{+1.8+13}_{-1.7-13}$
	350–450	11.13 ± 0.89	166.0 ± 4.78	0.69 ± 0.02	$0.07^{+0.09}_{-0.04}$	124^{+12}_{-11}	0.75 ± 0.07	$8.3^{+0.8+3.3}_{-0.7-3.3}$
	450–600	5.03 ± 0.6	71.45 ± 2.68	0.7 ± 0.02	$0.07^{+0.1}_{-0.04}$	64^{+9}_{-8}	0.9 ± 0.12	$4.5^{+0.6+1.8}_{-0.6-1.8}$
	≥600	2.51 ± 0.51	30.01 ± 1.79	0.64 ± 0.04	$0.08^{+0.11}_{-0.06}$	29^{+6}_{-5}	0.97 ± 0.19	$2.4^{+0.5+0.8}_{-0.4-0.8}$
E0	450–600	2.11 ± 0.21	15.17 ± 1.03	0.7 ± 0.02	$0.12^{+0.16}_{-0.08}$	$12^{+4.6}_{-3.4}$	0.64 ± 0.19	$1.5^{+0.6+0.5}_{-0.4-0.5}$
	≥600	0.68 ± 0.12	3.53 ± 0.52	0.7 ± 0.02	$0.03^{+0.04}_{-0.02}$			$0.34^{+0.13+0.13}_{-0.1-0.13}$
E1	250–350	18.15 ± 1.38	169.56 ± 5.97	0.61 ± 0.02	$0.11^{+0.14}_{-0.07}$	165^{+14}_{-13}	0.97 ± 0.08	$17.7^{+1.5+6}_{-1.4-6}$
	350–450	5.91 ± 0.44	53.49 ± 2.3	0.66 ± 0.02	$0.11^{+0.14}_{-0.08}$	49^{+8}_{-7}	0.92 ± 0.14	$5.4^{+0.9+1.6}_{-0.8-1.6}$
F	250–350	6.18 ± 0.45	106.19 ± 3.22	0.79 ± 0.02	$0.06^{+0.09}_{-0.03}$	107^{+11}_{-10}	1.01 ± 0.1	$6.2^{+0.7+3.1}_{-0.6-3.1}$
	350–450	2.79 ± 0.31	48.39 ± 1.71	0.82 ± 0.02	$0.06^{+0.09}_{-0.03}$	40^{+7}_{-6}	0.83 ± 0.13	$2.3^{+0.4+1.1}_{-0.4-1.1}$
	≥450	1.96 ± 0.27	36.07 ± 1.63	0.76 ± 0.03	$0.05^{+0.08}_{-0.02}$	22^{+6}_{-5}	0.61 ± 0.13	$1.2^{+0.31+0.7}_{-0.25-0.7}$
G0	450–550	2.64 ± 0.27	13.14 ± 1.15	0.72 ± 0.06	$0.2^{+0.27}_{-0.13}$	19^{+5}_{-4}	1.45 ± 0.36	$3.8^{+1.1+1.3}_{-0.9-1.3}$
	550–750	1.94 ± 0.28	12.11 ± 1.02	0.63 ± 0.02	$0.17^{+0.22}_{-0.12}$	18^{+5}_{-4}	1.17 ± 0.29	$3.1^{+0.9+0.9}_{-0.7-0.9}$
	≥750	1.4 ± 1.01	3.28 ± 0.61	0.63 ± 0.02	$0.05^{+0.06}_{-0.03}$			$0.83^{+0.25+0.25}_{-0.19-0.25}$
G1	250–350	2.61 ± 0.32	18.64 ± 1.27	0.5 ± 0.03	$0.14^{+0.19}_{-0.09}$	20^{+6}_{-4}	1.07 ± 0.25	$2.8^{+0.8+1.0}_{-0.6-1.0}$
	350–450	3.4 ± 0.3	21.27 ± 1.54	0.67 ± 0.04	$0.16^{+0.21}_{-0.11}$	24^{+6}_{-5}	1.13 ± 0.24	$3.8^{+1.0+1.3}_{-0.8-1.3}$
H	250–500	4.64 ± 0.49	54.43 ± 2.16	0.74 ± 0.03	$0.09^{+0.12}_{-0.05}$	49^{+8}_{-7}	0.9 ± 0.13	$4.2^{+0.7+1.9}_{-0.6-1.9}$
	≥500	1.98 ± 0.21	38.71 ± 1.66	0.79 ± 0.03	$0.05^{+0.08}_{-0.02}$	35^{+7}_{-6}	0.9 ± 0.16	$1.79^{+0.4+1.0}_{-0.3-1.0}$
I	250–350	22.06 ± 3.64	219.51 ± 7.8	0.44 ± 0.02	$0.1^{+0.14}_{-0.06}$	213^{+16}_{-15}	0.97 ± 0.07	$21.4^{+1.6+8}_{-1.5-8}$
	350–450	8.71 ± 1.25	78.02 ± 3.88	0.5 ± 0.02	$0.11^{+0.15}_{-0.07}$	61^{+9}_{-8}	0.78 ± 0.11	$6.8^{+1.0+2.4}_{-0.9-2.4}$
	450–550	2.63 ± 0.32	27.03 ± 1.76	0.56 ± 0.03	$0.1^{+0.13}_{-0.07}$	26^{+6}_{-5}	0.96 ± 0.2	$2.5^{+0.6+0.8}_{-0.5-0.8}$
	550–750	1.75 ± 0.27	17.42 ± 1.55	0.47 ± 0.04	$0.1^{+0.14}_{-0.07}$	14^{+5}_{-4}	0.8 ± 0.23	$1.4^{+0.5+0.5}_{-0.4-0.5}$
	≥750	3.27 ± 2.55	5.18 ± 0.78	0.52 ± 0.08	$0.63^{+1.17}_{-0.09}$	$3^{+2.9}_{-1.6}$	0.58 ± 0.35	$1.9^{+1.8+1.6}_{-1.0-1.6}$
J	250–350	37.55 ± 3.59	1315.05 ± 20.87	0.62 ± 0.01	$0.03^{+0.03}_{-0.02}$	1311^{+37}_{-36}	1.0 ± 0.03	$37.4^{+1.1+7}_{-1.0-7}$
	350–450	13.49 ± 1.26	372.04 ± 6.56	0.67 ± 0.01	$0.04^{+0.04}_{-0.03}$	320^{+19}_{-18}	0.86 ± 0.05	$11.6^{+0.7+2.1}_{-0.6-2.1}$
	450–550	4.22 ± 0.35	130.42 ± 4.15	0.66 ± 0.02	$0.03^{+0.04}_{-0.03}$	102^{+11}_{-10}	0.78 ± 0.08	$3.3^{+0.4+0.5}_{-0.33-0.5}$
	550–750	2.09 ± 0.21	75.11 ± 3.95	0.69 ± 0.03	$0.03^{+0.03}_{-0.02}$	76^{+10}_{-9}	1.01 ± 0.13	$2.11^{+0.27+0.5}_{-0.24-0.5}$
	≥750	0.46 ± 0.12	23.26 ± 1.63	0.59 ± 0.04	$0.02^{+0.03}_{-0.01}$	22^{+6}_{-5}	0.95 ± 0.21	$0.44^{+0.11+0.12}_{-0.09-0.12}$

Statistical: The two types of statistical uncertainties are the same as those described for the lost lepton estimates. Compared to the lost lepton estimates, the sizes of the statistical uncertainties are smaller because there are more events in the control region as well as more events from the W+jets MC. The sizes of the statistical uncertainties

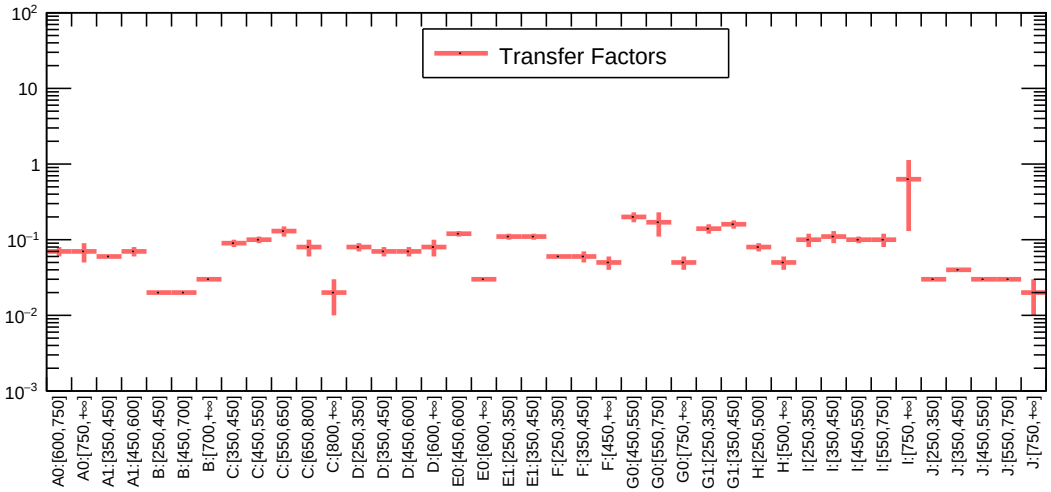

Figure 4.18: The transfer factors calculated as the ratio between the W+jets process in each SR and the total background in the corresponding CR, with the $E_{\mathrm{T}}^{\mathrm{miss}}$ extrapolation process taken into account. The SR labels defined in Section 3.4 are used in place of the selections criteria over N_{b}, $N_{\mathrm{b,\,soft}}$, t_{mod} and $M_{\ell\mathrm{b}}$, and the numbers in the square bracket indicates the $E_{\mathrm{T}}^{\mathrm{miss}}$ ranges.

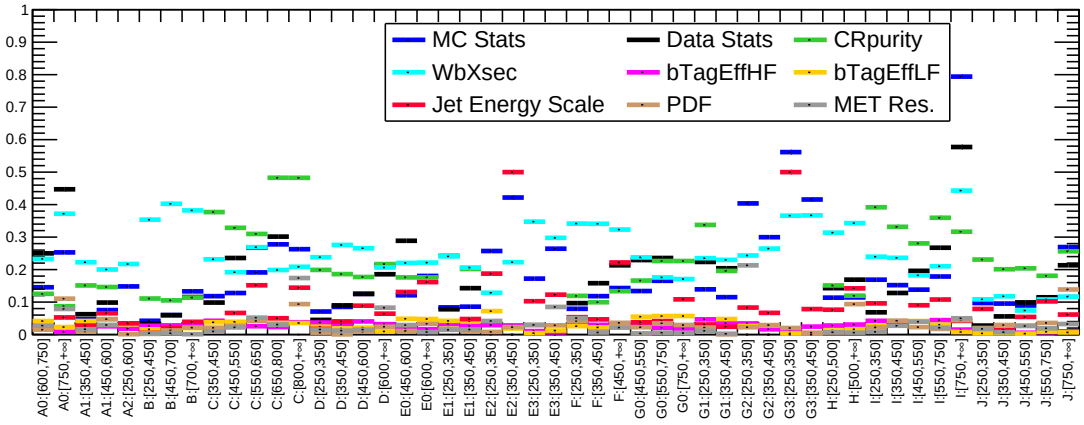

Figure 4.19: The prefit sizes of variations in the one lepton from W background estimation by the statistical uncertainties and the leading systematic uncertainties.

are generally less than 20% in regions with $M_{\ell\mathrm{b}} > 175\,\mathrm{GeV}$ where the W+jets is the dominant background contribution.

$\mathrm{W}+\mathrm{b\bar{b}}$ **cross section:** The seemingly largest uncertainty of the W+jets estimation, is due to our lack of understanding on the actual production of the $\mathrm{W}+\mathrm{b\bar{b}}$ events at the LHC, and they consist most of the W+jets events in the SR. A 50% uncertainty is assigned to the simulated W+jets events with at least one b quark jet. This uncertainty has a linear impact on the estimate as it basically only appears in the numerator. It is correlated over all search regions and is heavily constrained in the final fit.

W+jets purity in 0b CR: From Table 4.6 or Figure 4.17, we found that the W+jets process consist only 65–80% of the expected events in the 0b CRs with high $M_{\ell\mathrm{b}}$, or as low as 40% for low $M_{\ell\mathrm{b}}$ regions. This opens a window for the mismodeling of other background processes (notably $\mathrm{t\bar{t}}+\mathrm{jets}$) to bias the estimate for one lepton from W background. Hence the CR purity uncertainty is introduced by varying the contributions from the non W+jets processes in the 0b CR by 50%. This results in around 10–20% effect in the transfer factors for $M_{\ell\mathrm{b}} > 175\,\mathrm{GeV}$ regions.

b tagging scale factors: The heavy and light-flavor component of the b tagging is varied in the same way as described for the lost lepton estimation. They are more important for the W+jets estimate as the square of them enters the transfer factors now.

The PDF, Q^2, α_s, Jet Energy Scale, pile-up reweighting, L1 prefiring and $E_{\mathrm{T}}^{\mathrm{miss}}$ resolution uncertainties also present in the one lepton from W background estimates, and the share the same procedure as those described in Section 4.1.6.

4.3 Backgrounds estimate from simulation directly

The $Z \to \nu\bar{\nu}$ background and the single lepton backgrounds coming from $t\bar{t}$ or tW, where the single lepton is from the top quark decay fall into this category.

4.3.1 One lepton background with lepton from top decays

Processes with a single prompt lepton in the final state coming from top decay cannot be estimated through the 0b CR, as there will always be at least one real b jet from the top decay as well. The $M_{\mathrm{T}} > 150\,\mathrm{GeV}$ requirement is designed to suppress this background as much as possible, and it should be negligible in all signal regions compared to other backgrounds, due to the extra upper mass constraint on the W boson, imposed by the top quark mass. The small left-over is estimated through simulation because there is no good method to estimate it in a data-driven way, and also because the left-over contributions from this background are expected to be small enough to not affect the final fit, especially in the high $E_{\mathrm{T}}^{\mathrm{miss}}$ bins where the fit is most sensitive to the signal.

Since the spill-over of events with a single lepton from top to $M_{\mathrm{T}} > 150\,\mathrm{GeV}$ is mostly due to large misreconstruction of the $E_{\mathrm{T}}^{\mathrm{miss}}$, it is important to have a good modeling of this effect in the MC simulation. The *ad hoc* $E_{\mathrm{T}}^{\mathrm{miss}}$ resolution correction is important for this estimate, as the fake $E_{\mathrm{T}}^{\mathrm{miss}}$ component can smear both the magnitude and the direction of $E_{\mathrm{T}}^{\mathrm{miss}}$, and both of them are important inputs to the calculation of M_{T}.

Finally, to be extra conservative about the estimated yields obtained from simulation, a study was conducted to evaluate how much the final yield varies with or without the

application of the $E_{\mathrm{T}}^{\mathrm{miss}}$ resolution smearing. It has been observed that yields in some of the bins can change as much as 50%, and we are assigning a simple 100% uncertainty on every individual signal region, uncorrelated. It should be noted that this is a bit over conservative especially in the lower $E_{\mathrm{T}}^{\mathrm{miss}}$ bins.

The final estimation of the one lepton from top background in each of the individual signal region is summarized together with the final results in Chapter 5 by Table 5.1 for the standard search regions and Table 5.2 for the 2 sets of dedicated search regions for top and W corridor. The associated uncertainties for the estimates are the simple 100% uncorrelated uncertainties assigned on the expected yields for each SR.

4.3.2 $\mathrm{Z} \to \nu\bar{\nu}$ background

The $\mathrm{Z} \to \nu\bar{\nu}$ category contains all background processes that enter the signal region because of the large $E_{\mathrm{T}}^{\mathrm{miss}}$ due to the invisible Z decay, and mostly consist of $\mathrm{t\bar{t}Z}$ and some small amount of WZ with jets. Most notably, the $\mathrm{t\bar{t}Z}$ process, where the Z boson decays invisibly, produces the same final states as the signal does, and hence is considered as the only irreducible background of this analysis. In regions where we require the presence of a hadronically decaying top, the $\mathrm{t\bar{t}Z}$ contribution can reach as much as 60%, as can be seen in Figure 4.1.

In the ideal case, the $\mathrm{t\bar{t}Z}$ contribution can be estimated in a data-driven way from a trilepton region, where 2 of the leptons are of the same flavour, oppositely charged and with invariant mass within the Z peak. But this method is not practical in this analysis

because there will not be enough trilepton events to facilitate such a method. As it can be seen from Figure 4.1, the $Z \to \nu\bar{\nu}$ contribution is expected to be less than 2 events in regions where it contributes more than 20%. The detectable $t\bar{t}Z$ with $Z \to \ell^+\ell^-$ events are 5 times less than the $Z \to \nu\bar{\nu}$ ones, considering the difference from the branching ratios and the acceptance[‡], so we do not expect any meaningful statistics in constructing a trilepton control region for each signal region.

Another popular choice for estimating the $Z \to \nu\bar{\nu}$ contribution is resorting to the events with photons in place of the Z boson, and pretend they are invisible Z decays by inserting 4-vector of the photon to $E_{\mathrm{T}}^{\mathrm{miss}}$. However, in the case of $t\bar{t}Z$ and $t\bar{t}\gamma$, the kinematic properties of the two final states are quite different so that we would still have to rely on the simulation for the modeling of the final state kinematics.

Hence the $t\bar{t}Z$ contribution is estimated from MC simulation, but we take into consideration the latest measured cross section for $t\bar{t}Z$ process from the CMS collaboration [62] with $35.9\,\mathrm{fb}^{-1}$ of the data collected in 2016, as this was the latest available value by the time this analysis was going for publication. The measured value for the cross section was $\sigma(t\bar{t}Z) = 0.99^{+0.09}_{-0.08}(\mathrm{stat})^{+0.12}_{-0.10}(\mathrm{syst})\,\mathrm{pb}$, and is translated to a scale factor of $1.17^{+0.10}_{-0.09}$ with respect to the central value of SM prediction $0.84 \pm 10\,\mathrm{pb}$ at NLO accuracy. The uncertainties we assign for the scale factor contain only the statistical uncertainties from the measurement, and the theoretical uncertainties are considered to vary only the differential distributions of the events but not the total normalization.

[‡]While the leptons can only be accepted within $|\eta| < 2.4$, the neutrinos are contributing to $E_{\mathrm{T}}^{\mathrm{miss}}$ in any η range they are produced.

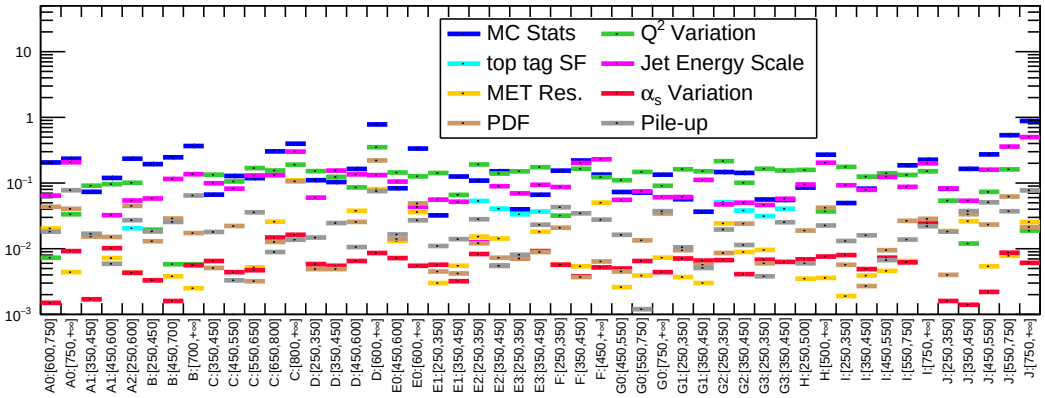

Figure 4.20: The prefit sizes of uncertainties for the $Z \to \nu\bar{\nu}$ estimation in the individual signal regions. The flat uncertainty on the cross section, which is around 8%, is not included.

The final estimation of the $Z \to \nu\bar{\nu}$ background in each of the individual signal region is summarized together with the final results in Chapter 5 by Table 5.1 for the standard search regions (A–H) and Table 5.2 for the 2 sets of dedicated search regions for top and W corridor. The associated uncertainties on the expected yields in the tables are simple quadrature sums of the statistical and systematic uncertainties. Figure 4.20 summarize the relative sizes of the leading uncertainties assigned for the $Z \to \nu\bar{\nu}$ background contribution. The flat uncertainty on the cross section, which is around 8%, is not included in the figure. The largest uncertainty is the statistical uncertainty related to the size of the MC sample (blue), followed by the renormalization and factorization (Q^2) scale variation (green) and the jet energy scale variation (magenta). The uncertainty related to top tagging is only present in bins where the top tag is required, and is only around 5%. Other less important uncertainties include the parton distribution function (PDF), the α_s scale, pile-up, lepton and b tagging scale factors.

One potential improvement that could be made to reduce the size of statistical uncertainty on the $t\bar{t}Z$ cross section, via a special trilepton control region to target the $t\bar{t}Z$ final state, to extract the cross section normalization from there using all $137.2\,\mathrm{fb}^{-1}$ of data available. However, compared with the size of other uncertainties, we determined that the expected improvement (around 5%) would not justify the extra effort to be devoted to the construction of such extra control regions.

Chapter 5

Results and interpretations

5.1 Final yields

The final results are summarized in Table 5.1 and Table 5.2, for the standard search regions and the two sets of corridor dedicated search regions, respectively, for data collected by the CMS detector from 2016 to 2018 and the corresponding SM Monte Carlo simulation for an integrated luminosity of $137.2\,\mathrm{fb}^{-1}$. The graphical representation of these numbers and the ratio between observed and estimated in each signal region can be found in Figure 5.1. The numbers and their uncertainties of the background categories are summarized from the discussions from the previous chapter. They are also called the pre-fit values, while the values after fitting the background predictions (or background+signal predictions) to the observed data are called post-fit values. Figure 5.3 shows the total backgrounds and the uncertainties before and after the background only

fit to the observed data.

Table 5.1: The observed and expected yields in the standard search regions. For the top quark tagging categories, we use the abbreviations U for untagged, M for merged, and R for resolved.

N_j	t_{mod}	$M_{\ell b}$ [GeV]	t cat.	p_T^{miss} [GeV]	Lost lepton	1ℓ (not from t)	1ℓ (from t)	$Z \to \nu\bar{\nu}$	Total expected	Total observed
2–3	>10	≤175	–	600–750	1.6 ± 0.7	1.1 ± 0.5	0.09 ± 0.09	1.8 ± 0.4	4.5 ± 0.9	3
				>750	0.26 ± 0.19	0.37 ± 0.28	–	0.59 ± 0.2	1.2 ± 0.4	4
			U	350–450	46 ± 5	16 ± 5	0.5 ± 0.5	8.5 ± 1.2	71 ± 8	88
				450–600	9.4 ± 1.5	7.3 ± 2.4	0.12 ± 0.12	3.9 ± 0.7	20.7 ± 3.0	19
			M	250–600	4.5 ± 1.1	1.2 ± 0.4	0.03 ± 0.03	1.6 ± 0.4	7.4 ± 1.3	7
2–3	>10	>175	–	250–450	6.6 ± 1.5	21 ± 10	0.18 ± 0.18	4.1 ± 0.9	32 ± 11	31
				450–700	0.55 ± 0.26	7 ± 4	–	1.7 ± 0.5	9 ± 4	10
				>700	0.07 ± 0.06	2.0 ± 1.1	–	0.36 ± 0.15	2.4 ± 1.1	2
≥4	≤0	≤175	–	350–450	245 ± 23	9.8 ± 3.5	21 ± 21	12.1 ± 2.7	289 ± 32	293
				450–550	48 ± 7	1.8 ± 0.7	4 ± 4	4.2 ± 0.9	58 ± 8	70
				550–650	16 ± 4	1.8 ± 1.0	0.6 ± 0.6	1.04 ± 0.31	19 ± 4	13
				650–800	6.6 ± 2.5	0.9 ± 0.4	0.7 ± 0.7	0.47 ± 0.19	8.6 ± 2.6	12
				>800	0.6 ± 0.7	0.25 ± 0.13	0.08 ± 0.08	0.12 ± 0.08	1.0 ± 0.7	4
≥4	≤0	>175	–	250–350	144 ± 13	38 ± 13	32 ± 32	6.5 ± 1.5	221 ± 37	186
				350–450	33 ± 5	8.3 ± 3.4	5 ± 5	2.5 ± 0.7	48 ± 8	45
				450–600	8.9 ± 2.5	4.5 ± 1.9	0.6 ± 0.6	1.05 ± 0.26	15.0 ± 3.2	17
				>600	3.2 ± 2.1	2.4 ± 0.9	0.35 ± 0.35	0.17 ± 0.16	6.2 ± 2.4	0
≥4	0–10	≤175	–	450–600	5.9 ± 1.5	1.4 ± 0.7	–	3.0 ± 0.7	10.4 ± 1.8	9
				>600	0.45 ± 0.28	0.34 ± 0.18	–	0.62 ± 0.24	1.4 ± 0.4	0
			U	250–350	186 ± 17	18 ± 6	4 ± 4	21 ± 4	230 ± 19	245
				350–450	26 ± 4	5.4 ± 1.8	0.6 ± 0.6	7.8 ± 1.3	40 ± 4	53
			M	250–350	1.7 ± 0.9	0.38 ± 0.16	2.7 ± 2.7	0.95 ± 0.27	5.7 ± 2.8	8
				350–450	2.4 ± 1.4	0.12 ± 0.12	0.5 ± 0.5	1.05 ± 0.29	4.1 ± 1.5	1
			R	250–350	5.6 ± 1.8	0.7 ± 0.4	1.9 ± 1.9	6.8 ± 1.5	15.0 ± 3.0	12
				350–450	2.6 ± 1.4	0.48 ± 0.25	0.15 ± 0.15	2.0 ± 0.5	5.3 ± 1.5	6
≥4	0–10	>175	–	250–350	10.4 ± 2.5	6.2 ± 3.2	1.0 ± 1.0	3.8 ± 0.8	21 ± 4	23
				350–450	1.2 ± 0.9	2.3 ± 1.2	0.12 ± 0.12	1.9 ± 0.8	5.6 ± 1.7	9
				>450	$0.5^{+1.0}_{-0.5}$	1.2 ± 0.7	0.08 ± 0.08	0.69 ± 0.25	2.5 ± 1.2	4
≥4	>10	≤175	–	450–550	6.5 ± 1.9	3.8 ± 1.7	0.5 ± 0.5	5.7 ± 1.0	16.6 ± 2.8	12
				550–750	2.7 ± 1.2	3.1 ± 1.2	0.1 ± 0.1	3.7 ± 0.8	9.5 ± 1.9	6
				>750	0.33 ± 0.18	0.83 ± 0.35	–	0.79 ± 0.16	1.9 ± 0.4	3
			U	250–350	34 ± 5	2.8 ± 1.2	1.1 ± 1.1	7.9 ± 1.8	46 ± 6	46
				350–450	19 ± 4	3.8 ± 1.6	0.8 ± 0.8	6.3 ± 1.5	30 ± 4	22
			M	250–350	0.37 ± 0.27	0.1 ± 0.06	0.6 ± 0.6	0.46 ± 0.15	1.5 ± 0.6	3
				350–450	0.8 ± 0.5	0.2 ± 0.1	0.3 ± 0.3	1.12 ± 0.23	2.4 ± 0.6	2
			R	250–350	2.3 ± 1.0	0.06 ± 0.09	0.09 ± 0.09	2.4 ± 0.5	4.8 ± 1.2	3
				350–450	0.8 ± 0.5	0.12 ± 0.08	0.31 ± 0.31	2.4 ± 0.6	3.6 ± 0.8	6
≥4	>10	>175	–	250–500	3.4 ± 1.4	4.2 ± 2.0	0.09 ± 0.09	1.7 ± 0.4	9.4 ± 2.5	8
				>500	1.1 ± 0.5	1.8 ± 1.0	0.3 ± 0.3	1.8 ± 0.6	5.0 ± 1.3	4

From the summary histogram of the results, we find that the observed data are in good agreement with the SM only background prediction. For comparison, Figure 5.2 shows the expected yields from example signals in the signal regions overlaid on top of

Table 5.2: The observed and expected yields for signal regions targeting scenarios of top squark production with a compressed mass spectrum.

N_{j}	$N_{\mathrm{b,\,med}}$	$N_{\mathrm{b,\,soft}}$	$p_{\mathrm{T}}^{\mathrm{miss}}$ [GeV]	Lost lepton	1ℓ (not from t)	1ℓ (from t)	$\mathrm{Z} \to \nu\bar{\nu}$	Total expected	Total observed
$\geq$5	$\geq$1	$\geq$0	250–350	403 ± 40	21 ± 8	71 ± 71	17 ± 4	511 ± 81	513
			350–450	108 ± 15	6.8 ± 2.5	12 ± 12	7.8 ± 1.6	134 ± 19	140
			450–550	31 ± 8	2.5 ± 1.0	2.0 ± 2.0	2.9 ± 0.8	39 ± 8	37
			550–750	11 ± 5	1.4 ± 0.6	0.27 ± 0.27	1.8 ± 0.5	14 ± 5	10
			>750	1.8 ± 1.1	$1.9^{+2.5}_{-1.9}$	0.16 ± 0.16	0.28 ± 0.1	4.1 ± 2.5	6
$\geq$3	$\geq$0	$\geq$1	250–350	201 ± 21	37 ± 7	27 ± 27	10.4 ± 1.5	276 ± 35	268
			350–450	38 ± 7	11.6 ± 2.2	3.4 ± 3.4	4.3 ± 0.9	58 ± 8	60
			450–550	11.5 ± 3.5	3.3 ± 0.6	0.7 ± 0.7	1.7 ± 0.6	17 ± 4	16
			550–750	3.5 ± 2.3	2.1 ± 0.5	–	1.1 ± 0.8	6.6 ± 2.5	6
			>750	0.4 ± 0.4	0.44 ± 0.16	0.02 ± 0.02	0.2 ± 0.4	1.0 ± 0.6	4

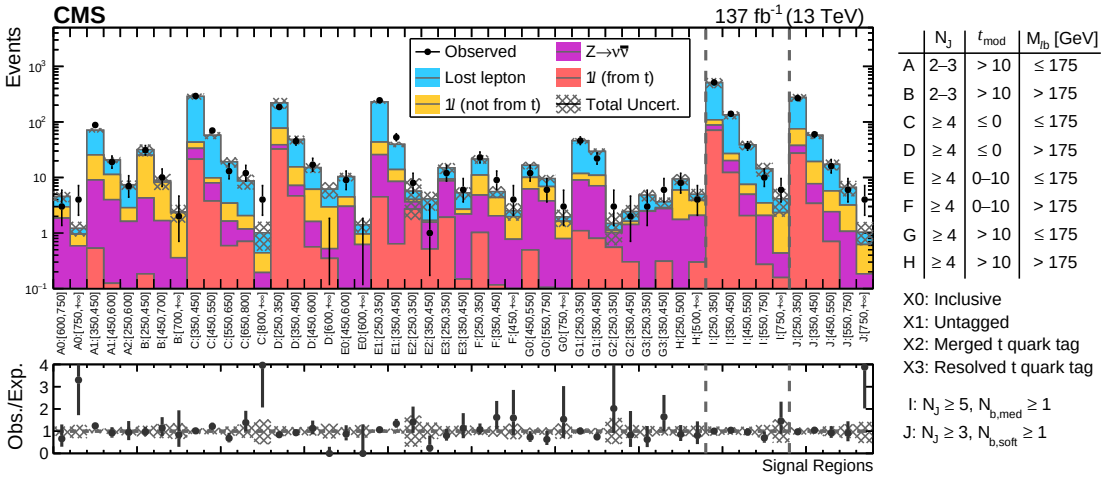

Figure 5.1: The observed and expected yields in Tables 5.1 and 5.2 and their ratios. The predicted SM contributions are shown as stacked histograms, the statistical and systematic uncertainties are summed in quadrature and are shown as shaded bands.

the results in Fig 5.1.

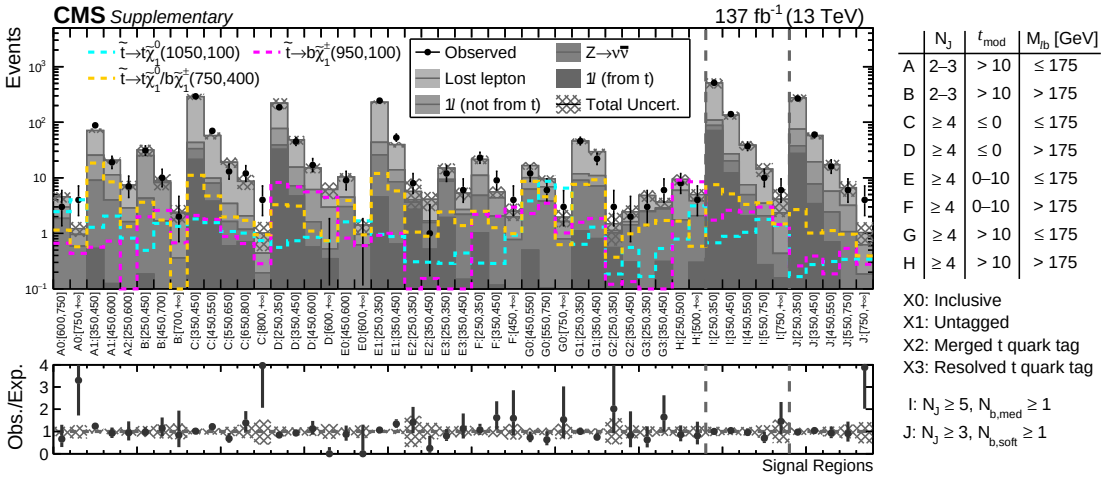

Figure 5.2: The observed and expected SM backgrounds in the signal regions, overlaid by the expected yields of selected signal hypothesis in colored lines. The SM background predictions are shown as stacked histograms with colors in grayscale, the statistical and systematic uncertainties are summed in quadrature and are shown as shaded bands.

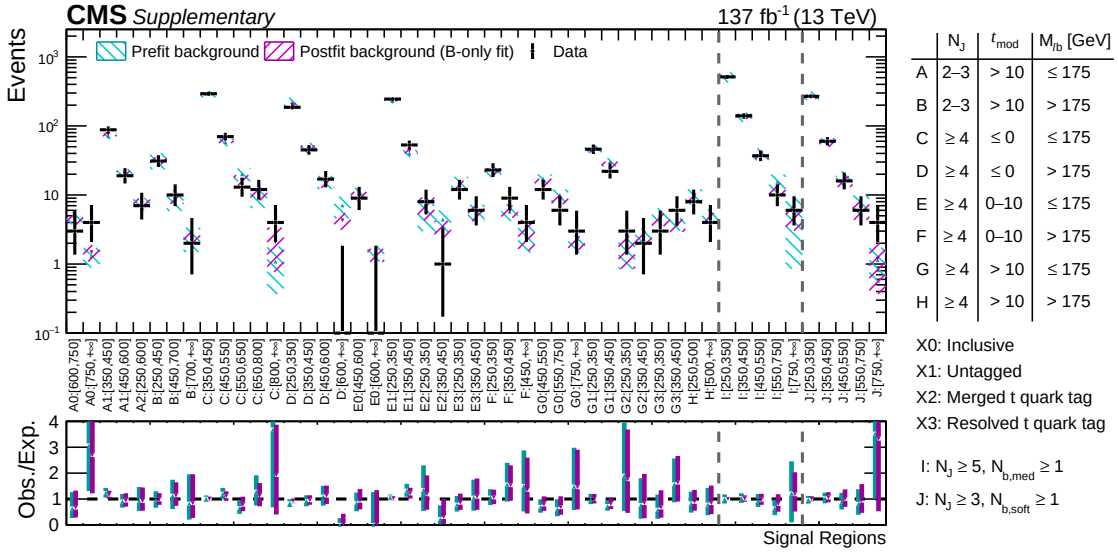

Figure 5.3: The post-fit yields and uncertainties for the total expected background after the background only fit to the observed data. The pre-fit yields and uncertainties for the background and the observed data are also drawn for comparison.

5.2 Interpretations

5.2.1 Signal contamination in control regions

The signal process can also produce events that would land in our control regions, and result in an overestimation for the corresponding background processes through the data-driven method. To counter for this effect in the final fit, the predicted signal yields in the signal regions are corrected by subtracting the overestimated part of the backgrounds brought by this signal. By changing the yield of the signal instead of correcting the background estimates, we remove the burden from readjusting this correction when the cross section of the signal moves away from its predicted value. This allows us to put upper limit on the signal cross sections with a single fit on the signal strength μ, which is a scale factor artificially introduced to control the cross section of the signal, with $\sigma_{\text{sig}} \to \mu\sigma_{\text{sig}}$.

Figures 5.4 and 5.5 show the relative size of the correction to the signal yields in SR resulting from the signal contamination in the dilepton CR and the 0b CR, respectively. For each mass point, the relative size of the correction is defined as the weighted average of the sizes of corrections in all the search regions involved, i.e. the standard search regions for points with $\Delta M(\tilde{\text{t}}, \tilde{\chi}_1^0) > 220\,\text{GeV}$, and the corresponding dedicated search regions for points with $\Delta M(\tilde{\text{t}}, \tilde{\chi}_1^0) \leq 220\,\text{GeV}$. The weight is defined by a simple $S/\sqrt{S+B}$ of the SR, where S stands for the expected signal yield and B for the expected SM background contribution in the SR in quest. In the case of T2tt, the relative signal contamination

from the top corridor strategy and the W corridor strategy has been shown where the dedicated strategies are used. Typical values of the corrections are around 5–10% of the signal yields, except for some compressed scenarios in terms of $\Delta M(\tilde{\mathrm{t}}, \tilde{\chi}_1^0)$, and they can reach as high as 25% along the W corridor.

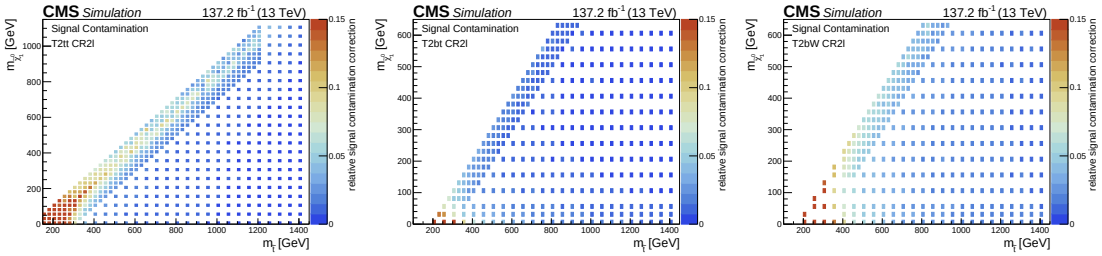

Figure 5.4: Relative correction to the signal region yields due to signal contamination in the dilepton control region. Left: T2tt, Middle: T2bt, right: T2bW.

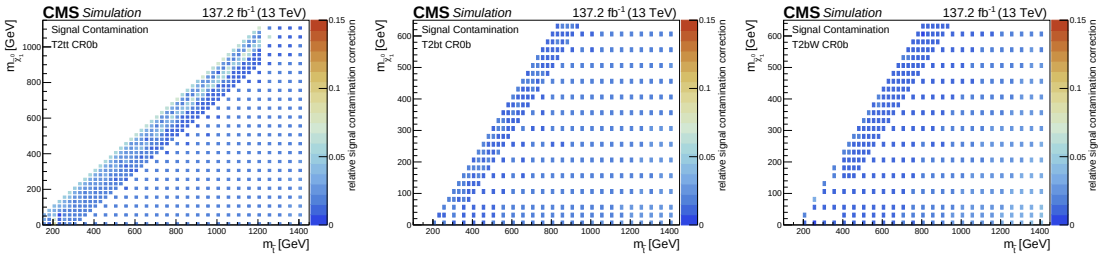

Figure 5.5: Relative correction to the signal region yields due to signal contamination in the 0b control region. Left: T2tt, Middle: T2bt, right: T2bW.

5.2.2 Signal uncertainties

The relative sizes of the systematic uncertainties vary with the signal models that are considered, as they have a wide range of preferences for the final state kinematics. The typical sizes of these uncertainties are listed in Table 5.3, separately for signals with higher or lower $\Delta M(\tilde{\mathrm{t}}, \tilde{\chi}_1^0)$, along with information on whether they are taken as

correlated across signal regions or they can vary independently in each signal region.

The largest uncertainty come from the statistical uncertainty in the signal simulation. The other dominating uncertainties are coming from the jet energy scale, and on the correction of system recoil by the number of recoiling ISR jets (the "ISR systematics", see Table 4.2).

One special treatment has been applied to the signal simulation to account for possible mismodeling in the reconstructed-$E_{\mathrm{T}}^{\mathrm{miss}}$ by taking the arithmetic mean between the reconstructed $E_{\mathrm{T}}^{\mathrm{miss}}$ ($E_{\mathrm{T,\,reco}}^{\mathrm{miss}}$) and the magnitude of the sum of the 4-vectors of the neutrinos and neutralinos from the generator truth information ($E_{\mathrm{T,\,gen}}^{\mathrm{miss}}$):

$$E_{\mathrm{T}}^{\mathrm{miss}}(\mathrm{signal}) = \frac{1}{2}\left(E_{\mathrm{T,\,reco}}^{\mathrm{miss}} + E_{\mathrm{T,\,gen}}^{\mathrm{miss}}\right)$$

On top of this, half of the difference between the original $E_{\mathrm{T,\,reco}}^{\mathrm{miss}}$ and $E_{\mathrm{T,\,gen}}^{\mathrm{miss}}$ is taken as uncertainty on the new $E_{\mathrm{T}}^{\mathrm{miss}}$ used for the signal events. While the size of this uncertainty is at a level of 5% for most signal hypothesis, it can become the most significant one for the signals with $\Delta M(\tilde{\mathrm{t}}, \tilde{\chi}_1^0) \sim m_{\mathrm{t}}$ as well as a small $m_{\tilde{\chi}_1^0}$, where the reconstructed $E_{\mathrm{T}}^{\mathrm{miss}}$ is also least trusted.

5.2.3 Limits

The results from Section 5.1 are interpreted in the context of the top squark pair production models described in Section 2.1.1.

For a given model, multiple hypotheses as a function of $m_{\tilde{\mathrm{t}}}$ and $m_{\tilde{\chi}_1^0}$ are tested, and

Table 5.3: Summary of the systematic uncertainties with their typical values in individual signal bins. The first value is for the compressed region, while the second value for the non-compressed region. Also indicated is whether the uncertainty is taken as correlated across signal regions or not.

Source	Typical size		Correlated
	low ΔM	high ΔM	
Signal sample statistics	7–15%	5–36%	–
Jet energy scale	1–20%	1–12%	✓
Pile-up	5–10%	5–10%	–
System recoil("ISR")	15%	1–8%	✓
$E_{\mathrm{T}}^{\mathrm{miss}}$ modeling uncertainty	2–7%	1–10%	–
Trigger Efficiencies	2–3%	2–3%	✓
Luminosity	2.5%	2.5%	✓
Lepton efficiency	1%	3–4%	✓
b-tagging scale factors	1–2%	1–7%	✓
Lepton veto efficiency	3%	3%	–
Merged t tagging efficiency	–	3–6%	✓
Resolved t tagging efficiency	2–3%	–	✓
Soft b tagging efficiency	2–3%	–	✓
Renormalization and factorization scale	2–4%	2–4%	✓

the 95% confidence level (CL) upper limits on the production cross sections of these hypotheses are derived given the observed data in the signal region. This is achieved by combining the observations in the search regions using a modified frequentist approach, employing the $\mathrm{CL_s}$ criterion and an asymptotic formulation [63, 64, 65, 66].

Figure 5.6 shows the 95% CL exclusion limits for the T2tt scenarios, based on the expected $\tilde{\mathrm{t}}\bar{\tilde{\mathrm{t}}}$ pair production cross sections as shown in Figure 2.1, and with the assumption that the top quarks produced in the decay of the stop are unpolarized. The observed 95% CL upper limits on the cross sections of the signals are interpolated across the available $m_{\tilde{\mathrm{t}}}$ and $\tilde{\chi}_1^0$ range and are drawn as the colored map. In this figure, the results for signal points with $\Delta M(\tilde{\mathrm{t}}, \tilde{\chi}_1^0) \leq 150\,\mathrm{GeV}$ are obtained from the dedicated W corridor search

regions, and signal points with $150\,\text{GeV} < \Delta M(\tilde{\text{t}}, \tilde{\chi}_1^0) \leq 220\,\text{GeV}$ are obtained from the dedicated top corridor search regions. For all other points, the cross section limits are obtained from the standard search regions. For signal points in the W corridor, the cross section upper limits obtained from the dedicated regions are up to five times smaller than those obtained from the standard search regions. On the other hand, the expected upper limits for the signals in the top corridor obtained from dedicated top corridor are typically 10–20% smaller than those from the standard search regions.

We exclude the existence of top squarks with masses up to 1.2 TeV for models featuring a light LSP, and models with the lightest neutralino mass up to 600 GeV have been excluded when $m_{\tilde{\text{t}}} \simeq 1.1\,\text{TeV}$. The white-out region corresponds to $\left|\Delta M(\tilde{\text{t}}, \tilde{\chi}_1^0) - m_{\text{t}}\right| < 25\,\text{GeV}$ and $m_{\tilde{\text{t}}} < 275\,\text{GeV}$, where the acceptance for top squark events is very sensitive to the details of the simulation. Therefore no interpretation for the $\tilde{\text{t}}$ signals in this region is performed in this analysis, and it is left for a dedicated analysis specially designed for it, which is out of the scope of this thesis.

Figure 5.7 shows the 95% CL exclusion limits for the T2bW scenarios. For these signal models, the signal regions with $M_{\ell\text{b}} < 175\,\text{GeV}$ drives the exclusion limits. Under the T2bW scenarios, top squarks with mass up to 1.1 TeV are excluded when the LSP in the model is light, and models with LSP masses up to 550 GeV are excluded when $m_{\tilde{\text{t}}} \simeq 1\,\text{TeV}$

Figure 5.8 shows the 95% CL exclusion limits for the T2bt scenarios, top squark masses up to 1 TeV for models with a light LSP and models with LSP masses up to

500 GeV are excluded when $m_{\tilde{t}} \simeq 950\,\text{GeV}$.

It should be noted that the above exclusion limits for the top squark pair production are obtained by considering the $\tilde{t}\bar{\tilde{t}}$ decays in the single lepton final state only. Figure 5.9 taken from [67] shows the expected and observed exclusion limits at 95% CL for the 3 signal scenarios when combined with the results from the dedicated searches for $\tilde{t}\bar{\tilde{t}}$ decays in the dilepton final state [68] and the all-hadronic final state [60]. In all 3 signal scenarios the expect exclusion limits for the top squark can be extended by 100 GeV in mass (when featuring a light LSP) with respect to the single lepton final state only results.

Other than the top squark pair production models (that this analysis is tuned for), our result can also be reinterpreted in terms of upper limits on the Higgs to invisible decay featuring $t\bar{t}H$ production channel, or direct dark matter production in association with $t\bar{t}$ ($t\bar{t}$+DM) models. More details on these upper limits can be found in Appendix B.

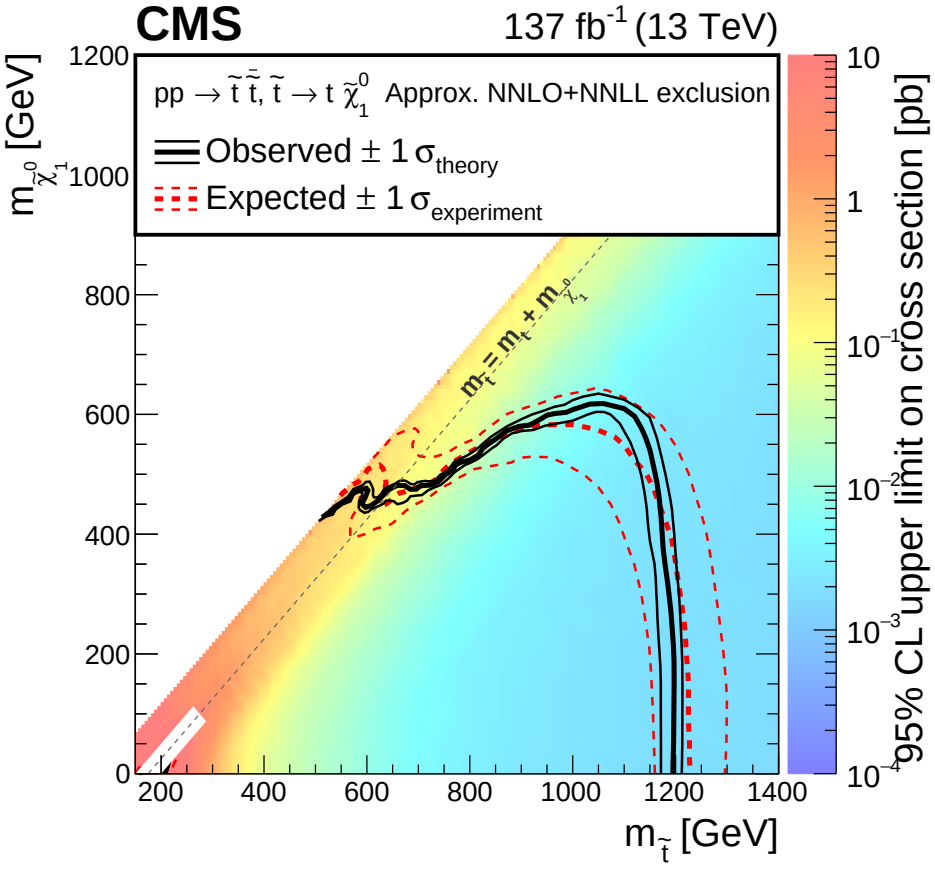

Figure 5.6: Exclusion limits at 95% CL for the T2tt ($\tilde{t} \to t\tilde{\chi}_1^0$) scenarios. The interpretation is done in the two dimensional space of $m_{\tilde{\chi}_1^0}$ vs $m_{\tilde{t}}$. The colored map illustrates the 95% CL upper limit on the product of cross section and branching fraction at each point. The area enclosed by the solid black curve represents the observed exclusion region at 95% CL, with the thin solid black lines showing the change in the observed limit by varying the signal cross sections within their theoretical uncertainties. The thick and thin dashed red lines indicate the limits under the background-only hypothesis at 95% CL and their variations within $\pm 1\sigma$ of the experiment standard deviation uncertainties.

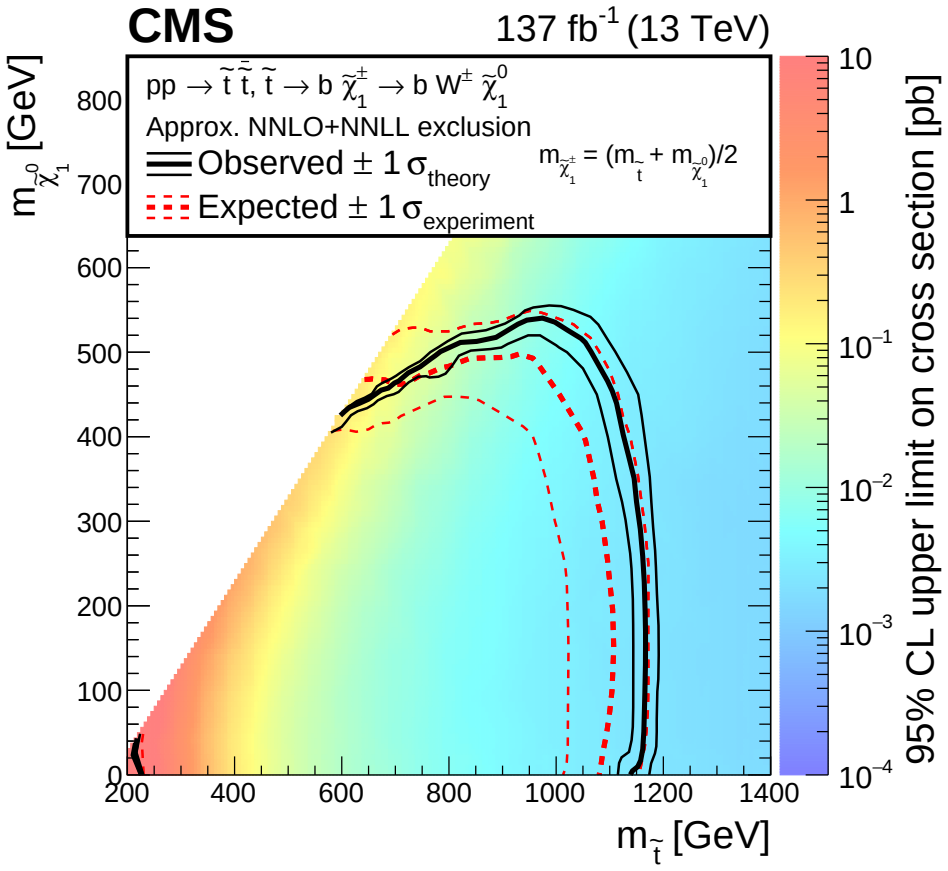

Figure 5.7: Exclusion limits at 95% CL for the T2bW ($\tilde{t} \rightarrow b\tilde{\chi}_1^{\pm}$, followed by $\tilde{\chi}_1^{\pm} \rightarrow W\tilde{\chi}_1^0$) scenarios, where the mass of $\tilde{\chi}_1^{\pm}$ is fixed to $m_{\tilde{\chi}_1^{\pm}} = (m_{\tilde{t}} + m_{\tilde{\chi}_1^0})/2$. The interpretation is done in the two dimensional space of $m_{\tilde{\chi}_1^0}$ vs $m_{\tilde{t}}$. The colored map illustrates the 95% CL upper limit on the product of cross section and branching fraction at each point. The area enclosed by the solid black curve represents the observed exclusion region at 95% CL, with the thin solid black lines showing the change in the observed limit by varying the signal cross sections within their theoretical uncertainties. The thick and thin dashed red lines indicate the limits under the background-only hypothesis at 95% CL and their variations within $\pm 1\sigma$ of the experiment standard deviation uncertainties.

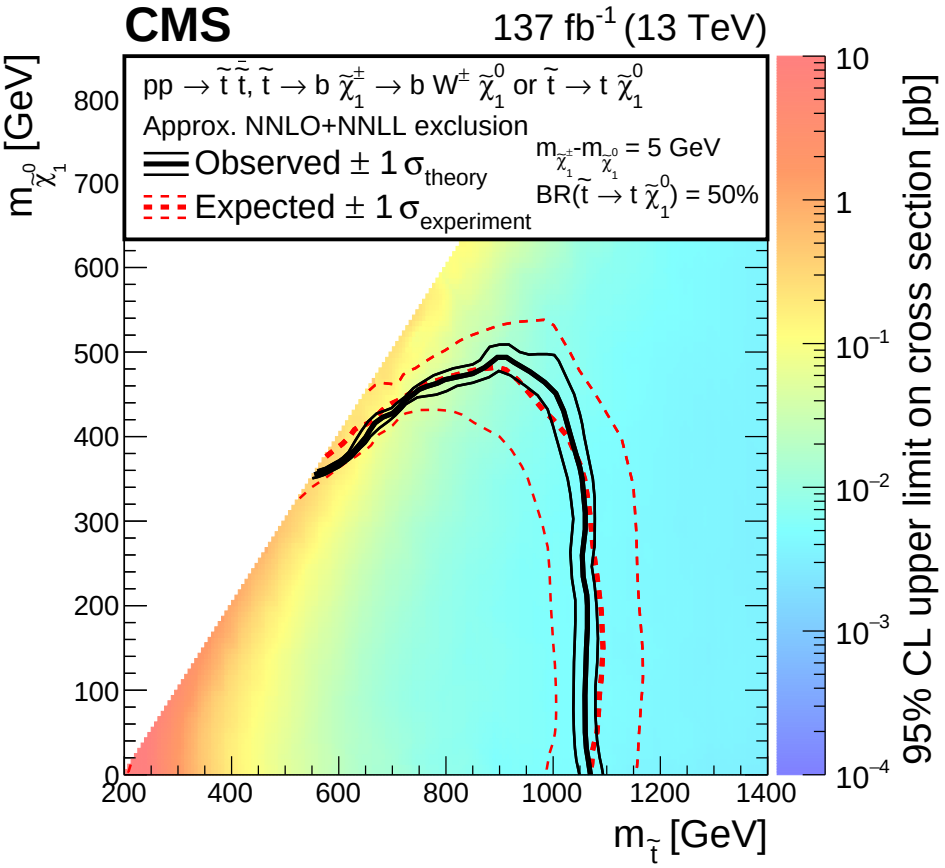

Figure 5.8: Exclusion limits at 95% CL for the T2bt ($\tilde{t} \to t\tilde{\chi}_1^0/b\tilde{\chi}_1^\pm$, followed by $\tilde{\chi}_1^\pm \to W^*\tilde{\chi}_1^0$) scenarios, where the mass of $\tilde{\chi}_1^\pm$ is fixed to $m_{\tilde{\chi}_1^\pm} = m_{\tilde{\chi}_1^0} + 5\,\text{GeV}$, and branching ratios $\text{BR}(\tilde{t} \to b\tilde{\chi}_1^\pm) = \text{BR}(\tilde{t} \to t\tilde{\chi}_1^0) = 0.5$. The interpretation is done in the two dimensional space of $m_{\tilde{\chi}_1^0}$ vs $m_{\tilde{t}}$. The colored map illustrates the 95% CL upper limit on the product of cross section and branching fraction at each point. The area enclosed by the solid black curve represents the observed exclusion region at 95% CL, with the thin solid black lines showing the change in the observed limit by varying the signal cross sections within their theoretical uncertainties. The thick and thin dashed red lines indicate the limits under the background-only hypothesis at 95% CL and their variations within $\pm 1\sigma$ of the experiment standard deviation uncertainties.

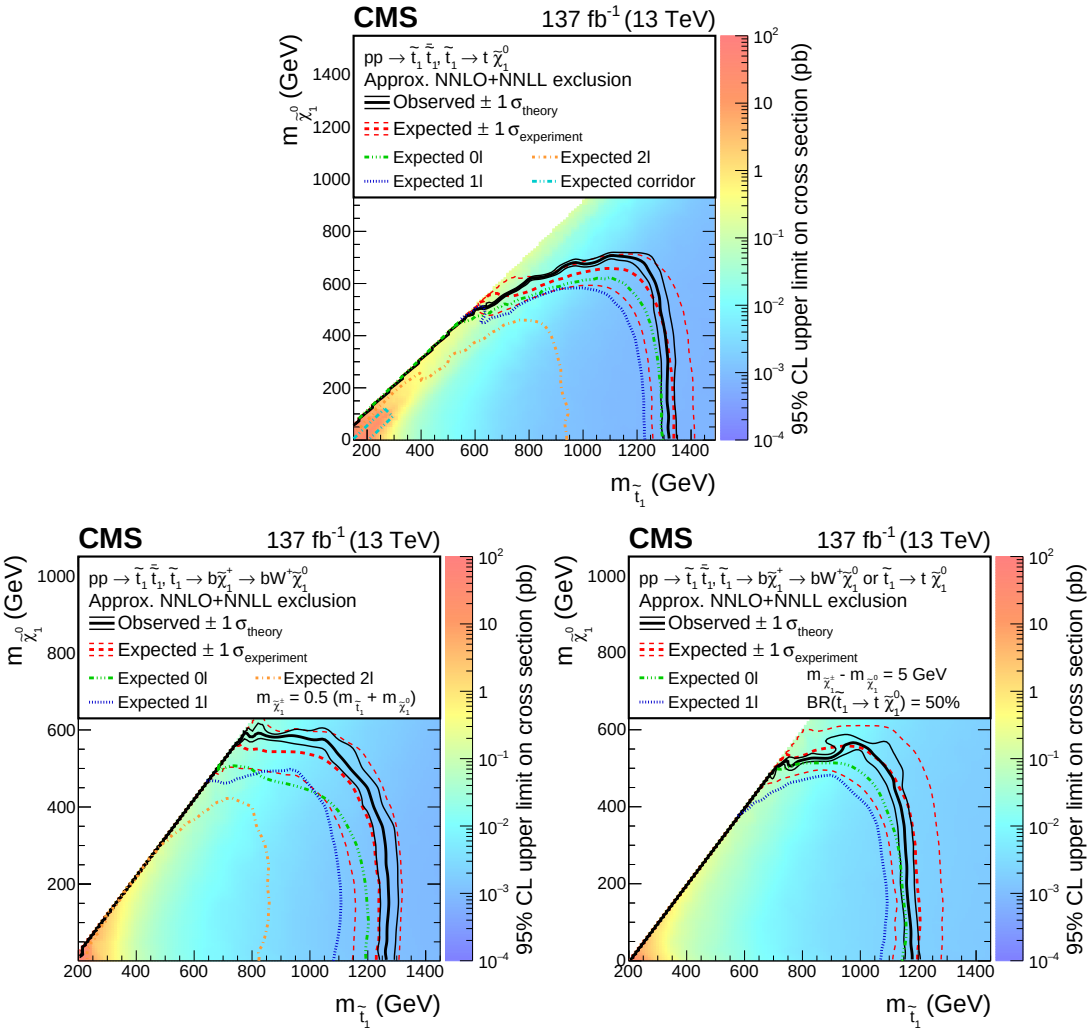

Figure 5.9: Expected and observed limits for the combined top squark searches (0ℓ, 1ℓ, 2ℓ, corridor) [67] in the $m_{\tilde{t}}$-$m_{\tilde{\chi}_1^0}$ plane, for the T2tt (upper), T2bW (lower left) and T2bt (lower right) scenarios. The color indicates the 95% CL upper limit on the cross section at each point in the plane. The area below the thick black curve represents the observed exclusion region at 95% CL, while the dashed red lines indicate the expected limits at 95% CL and the region containing 68% of the distribution of limits expected under the background-only hypothesis of the combined analyses. The thin black lines show the effect of the theoretical uncertainties in the signal cross section.

Chapter 6

Summary and conclusions

We have performed a search for new physics beyond the Standard Model, based on the proton-proton collision data at a center-of-mass energy of 13 TeV, recorded by the CMS detector at the LHC during 2016, 2017 and 2018, with the amount of data corresponding to an integrated luminosity of $137.2\,\mathrm{fb}^{-1}$. The search focus on the final state with a single isolated electron or muon, multiple jets, and large transverse momentum imbalance, and is optimized to target direct top squark pair production at the LHC. This search is an update to the previous searches for such signals with the largest data set by far as well as employing new techniques to enhance the sensitivities.

The core of this search is looking for excess of events with large missing transverse momentum, with carefully designed and data-driven techniques to control the background from the existing Standard Model processes. We found that the observed data are consistent with expectations from Standard Model processes. Exclusions for possible new

physics models are set in the context of simplified top squark pair production models. Depending on the model, existence of top squark with mass up to 1.2 TeV has been excluded at 95% confidence level, with a massless lightest supersymmetric particle (assumed to be the neutralino) in the model. In these models, the neutralino with mass up to 600 GeV is excluded that the top squark mass is at around 1 TeV. The exclusion also covers the possibility when the mass difference between the top squark and neutralino is close to the mass of the top quark or the W boson with specially designed efforts and technologies. In such models, top squarks of masses up to 550 GeV had been excluded.

With the results from this search (and many others that have been conducted at the same time) it is becoming increasingly unlikely that the SUSY hypothesis in its simplest form can fully resolve the naturalness problem. There are multiple proposals that add complexity to the SUSY hypothesis and can explain the non-discovery of the top squark at the TeV scale, and there may be new theories coming up that can explain the necessity of such complexity. On the positive side, this could mean that there may be something more profound, more revolutionary waiting for us to discover. We shall keep looking for hints from the experiment, on any front that could present a departure from the prediction of the current Standard Model, to point us in the right direction. I would like to repeat the quote from David Hilbert for the ending of this thesis: "We must know, and we will know".

Appendix A

Studies on heavy object tagging

This appendix chapter discusses the investigations on the inclusion strategy of the top taggers and the soft b tagger.

A.1 The top taggers

The studies for the top taggers was carried out with a projection of the Run II data set, and the expected luminosity used was $120\,\mathrm{fb}^{-1}$. No further reoptimization has been carried out given that the final integrated luminosity for Run II study, $137.2\,\mathrm{fb}^{-1}$, is only 12% more.

A.1.1 Resolved top tagging

The DeepResolved algorithm identifies hadronically decaying top quarks whose decay products form 3 individual jets. Top quark candidates are formed by combining three

AK4 jets which must pass p_{T} requirements of 40, 30, 30 GeV on the three jets respectively. The three jets of each candidate must have an invariant mass between 100 and 250 GeV, no more than one of the jets can be identified as a b jet, and the three jets must all lie within a cone of $\Delta R < 3.14$ of the trijet centroid.

After the loose preselection, a neural network is used to distinguish between trijet combinations whose three jets all match to the decay products of a top quark versus those that do not. The network uses high-level information such as the invariant mass of the trijet and individual di-jet pairs, as well as information from each jet including jet Lorentz vector, deepCSV heavy-flavor discriminator values, jet-shape variables, and detector level particle multiplicity and energy fraction variables. The network is trained using both $\mathrm{t\bar{t}}$ and QCD simulations, as well as data for the training inputs. The simulation is used to define the examples of signal and background. Signal is defined as any trijet passing the pre-selection where each jet is matched to a generator level daughter of a top quark within a cone of $\Delta R < 0.4$ and the overall trijet system is matched to the generator level top quark within a cone of $\Delta R < 0.6$. The background category is defined as any trijet combination which is not categorized as signal. This includes trijet combinations where some, but not all, of the jets match top decay products. The data is included in the training to inhibit the network from learning features of the MC which are not present in data. This is achieved through a technique called domain adaption via gradient reversal [69]. With this method an additional output is added to the neural network which is tasked with distinguishing between trijet candidates from QCD simulation and

a sample of QCD enriched events from data. The main network is then restricted to minimize the ability to discriminate simulation from data. This yields a network with good separation between signal and background while minimizing over-fitting on features that exist only in simulation.

Before the final selection of trijets as top quarks can be made, any trijet candidates which may share the same jets with another candidate must be removed. This is achieved by always favoring a candidate with a higher top discriminator as determined by the neural network over one with a lower discriminator. The final list of reconstructed tops is then found by placing a requirement on the neural network discriminator. In this analysis, we look for events containing at least one recognized hadronic top decay using the tight working point (discriminator value > 0.95).

Correction factors between the tagging efficiencies in the data and simulation are derived in a $\mathrm{t\bar{t}}$ enriched control region. The mistag is defined as the candidate passing the tight working point, but the 3 jets are either not coming from the same top decays, or some of the jets are coming from other sources such as ISR, and they are mainly estimated through control regions. Further correction factors tagging efficiencies are derived between the events generated by the CMS fast simulation program [46, 47] (referred to as Fastsim), and the events generated with the GEANT4 [45] package (referred to as Fullsim) in simulating the response of the CMS detector. Fullsim is used in the generation of events from all SM processes, while Fastsim is used in the generation the events for SUSY signals. The Fullsim to Fastsim correction factors are derived separately for the 3

years and with respect to the p_{T} of the top candidates.

An example of the efficiency on SM background and the signal can be seen on Figure A.1, where the expected yields in the standard model background and an example T2tt signal point is showed

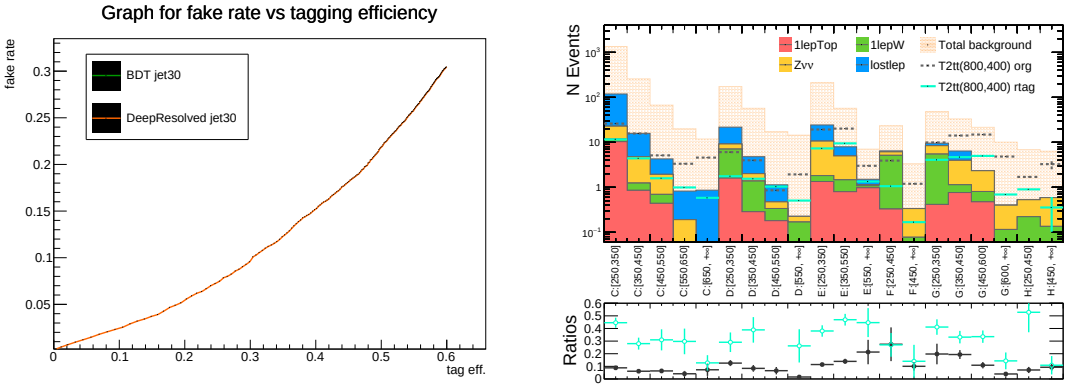

Figure A.1: Left: The signal to background efficiency curve with the analysis base selection. Right: the expected yields in signal regions for T2tt type of signal with $m_{\tilde{\mathrm{t}}} = 800\,\mathrm{GeV}$ and $m_{\tilde{\chi}_1^0} = 400\,\mathrm{GeV}$ and full standard model background, projected to $120\,\mathrm{fb}^{-1}$. The ratio panel shows the ratio after over before requiring the events to have a resolved top tag.

A.1.2 Merged top tagging

In scenarios when the hadronically decaying top quarks were produced with large boost, its decay products may be largely overlapping with each other. In such cases, the decay products may not be recognized as 3 separate AK4 jets, but are likely to be reconstructed a single AK8 jet in the final state.

This analysis utilize the DeepAK8 algorithm [61] to target this type of top decays. The DeepAK8 algorithm is a multi-class classifier for top, W, Z, Higgs and QCD jets based on standard AK8 jets. The tagger builds upon a Deep Neural Network taking

input from all the PF candidates and secondary vertices inside the AK8 jet. Inclusive PF candidates, charge PF candidates and secondary vertices are first processes separately with three one dimensional convolutional neural networks, and then the outputs from these three networks are further combined into a fully-connected layer before yielding the final prediction.

Specifically to this analysis, the efficiency for selecting events that contain at least one merged top tag has been studied on signal and background, and the results are shown in Figure A.2. On the left, the curve of signal versus background efficiency under different working points are shown, where the signal samples are T2tt FastSim scans with $\Delta M(\tilde{\mathrm{t}}, \tilde{\chi}_1^0) > 600\,\mathrm{GeV}$, and the background samples are all relevant SM contributions, passing the baseline selections of the analysis. On the right, an example for the expected yields in the individual analysis regions before and after requiring events to have at least one merged top tag is shown, for the signal point of T2tt type with $m_{\tilde{\mathrm{t}}} = 1200\,\mathrm{GeV}$ and $m_{\tilde{\chi}_1^0} = 50\,\mathrm{GeV}$ and the SM background processes.

Correction factors have been derived using a Tag and Probe method in the single muon sample, where the probe is defined as the highest p_T candidate opposite to the muon. Three mass templates: top-matched, W-matched and unmatched are used in the fit to extract tagging efficiencies in both data and simulation. The correction factors ranges from 0.96 to 1.06, depending on the p_T of the AK8 jets as well as the year of data taking and Monte Carlo simulation. They are summarized in Table A.1

Further correction factors are derived between the Fastsim and Fullsim simulations,

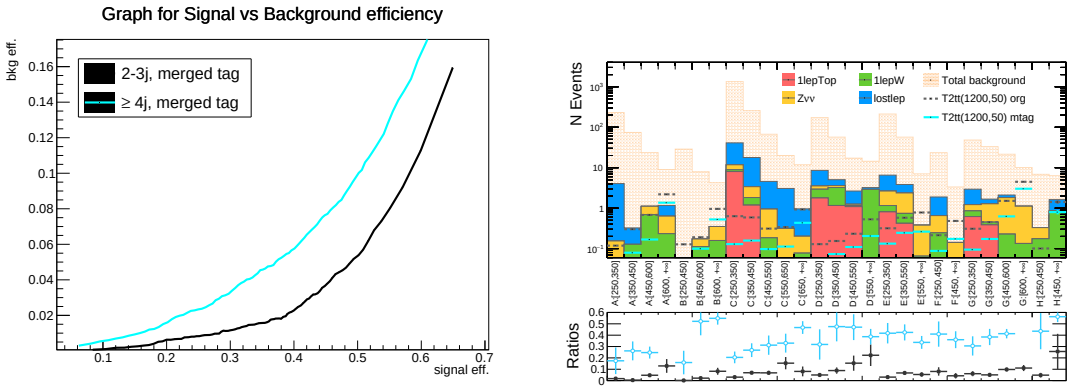

Figure A.2: Left: The signal versus background efficiency plot for the DeepAK8 top scores. The signal consists of T2tt-scan FastSim scans with $\Delta M(\tilde{t}, \tilde{\chi}_1^0) > 600\,\text{GeV}$, and the background yields are from all relevant SM backgrounds. Right: The expected yields in signal regions for T2tt type of signal with $m_{\tilde{t}} = 1200\,\text{GeV}$ and $m_{\tilde{\chi}_1^0} = 50\,\text{GeV}$ and full standard model background, projected to $120\,\text{fb}^{-1}$. The ratio panel shows the ratio after over before requiring the events to have a resolved top tag.

Table A.1: Scale factor values for DeepAK8 algorithm on identifying top with working point 0.4, between the data and simulation. The numbers are derived in bins of the p_T of the AK8 jet, and for different years of the data taking period.

Year	p_T(AK8 jet) [GeV]		
	400 – 480	480 – 600	600 – 1200
2016	1.01 ± 0.11	1.05 ± 0.08	1.06 ± 0.05
2017	1.08 ± 0.10	0.97 ± 0.07	1.02 ± 0.08
2018	0.95 ± 0.07	1.06 ± 0.05	0.94 ± 0.05

by comparing the tagging efficiencies for the truth matched hadronic top decays in the 2 types of simulations for the T2tt type signals. The numbers are summarized in Table A.2, and are applied as event weights on the Fastsim simulation, based on the year of data taking that the simulation is supposed to model, and in terms of the p_T of the leading AK8 jet that is tagged as top decay by the DeepAK8 algorithm.

Table A.2: Scale factor values for DeepAK8 algorithm on identifying top with working point 0.4, for the Fastsim simulations. The numbers are derived in bins of the p_{T} of the AK8 jet, and for different years of the data taking period.

Year	p_{T}(AK8 jet) [GeV]			
	200 – 400	400 – 480	480 – 600	600 – 1200
2016	1.12 ± 0.15	0.99 ± 0.06	0.96 ± 0.04	0.92 ± 0.02
2017	1.01 ± 0.11	0.95 ± 0.04	1.00 ± 0.04	0.96 ± 0.02
2018	0.80 ± 0.08	1.03 ± 0.06	1.03 ± 0.04	1.03 ± 0.04

A.1.3 Inclusion strategy

Depending on the topology of the signal, we may have more boosted tops in scenarios when $\Delta M(\tilde{\mathrm{t}}, \tilde{\chi}_1^0) > 600$ or more resolved tops when $\Delta M(\tilde{\mathrm{t}}, \tilde{\chi}_1^0) < 450$. Since we do not have enough knowledge of where the signal lies, we are employing both top taggers in the analysis, by splitting the existing search regions into 3 categories: merged-tagged, resolved-tagged, untagged. In order to be classified into the merged-tagged regions or the resolved-tagged regions, the event is required to have at least one merged top tag or at least one resolved top-tagged, respectively. In the case when the event contains both merged top tag(s) and resolved top tag(s), the priority is given to the merged tagged region as a better signal efficiency has been observed in the merged top tagger given the same background rejection. In the region with 2–3 jets requirement, we are only splitting events into 2 categories by the merged top tag, which is found to be very useful in identifying semi-leptonic decay of the T2tt signal when hadronically decaying top are very boosted and merged.

The correlation between the top taggers and other existing quantities has been studied and found to be minimal. However, inspecting the existing strategy, we expect the

targeted type of signal T2tt to live in the lower $M_{\ell \mathrm{b}}$ regions, so the splitting by top tags is only applied to regions where $M_{\ell \mathrm{b}} \leq 175\,\mathrm{GeV}$. Furthermore, we have found that the signal to background rejection by the top taggers are largely reduced in regions with high $E_{\mathrm{T}}^{\mathrm{miss}}$. In order to retain a reasonable statistics in the high $E_{\mathrm{T}}^{\mathrm{miss}}$ regions, where most of the signal sensitivity lies, the splitting of top tags are only applied to regions where $E_{\mathrm{T}}^{\mathrm{miss}}$ is lower than 450 GeV, with the exception on the 2–3 jets region where the $E_{\mathrm{T}}^{\mathrm{miss}}$ boundary is set at 600 GeV. Lastly, we restrict the splitting only to regions where $t_{\mathrm{mod}} > 0$ where the most sensitivity for the targeted signal type (T2tt) lies.

The final result of the binning refinement, combined with optimized binning in $E_{\mathrm{T}}^{\mathrm{miss}}$, can be found in Table 3.6.

A.2 Study on soft b identification

Signal models featuring low top squark masses remain theoretically interesting as they require minimal fine tuning. However, the only low $m_{\tilde{\mathrm{t}}}$ that have not been excluded by the previous searches are models with $m_{\tilde{\mathrm{t}}} < m_{\mathrm{t}}$. This mass constraint results in low $E_{\mathrm{T}}^{\mathrm{miss}}$, jet p_{T}, and lepton p_{T} in the signal final state. Specifically, for signal models in the W corridor ($m_{\tilde{\mathrm{t}}} \sim m_{\mathrm{t}} + m_{\mathrm{W}}$), the b quark jets in the event would have a low tagging efficiency due to their soft p_{T} spectrum (they failed to be identified as a good jet in the first place). Hence, an algorithm to tag low p_{T} b quarks is beneficial to both rising the selection efficiency for signals in signal regions as well as reducing the signal contamination in the

0b control region used to estimate the W+jets background*. The soft b tag identification was studied in detail by previous analyses [70, 28] and was optimized to identify b quarks with $p_{\mathrm{T}} < 20\,\mathrm{GeV}$. The identification of the soft b jets is described in Section **??** and the inclusion strategy is described in Section 3.3.4. In this appendix section, efficiencies, scale factors, and pile-up studies will be discussed.

The tagging efficiency and fake rate of the soft b identification is measured in a sample of eμ events, and scale factors (to correct the MC modeling to match the data) were derived for the tagging efficiencies for the 3 years separately, with values for 2016: 1.08 ± 0.03, 2017: 1.05 ± 0.06, and 2018: 1.19 ± 0.06. These scale factors are validated with the observed data and MC simulation satisfying the eμ cross-check region selections described in Section 4.1.4 and with exactly 1 b-tagged jet ($p_{\mathrm{T}} > 30\,\mathrm{GeV}$ and pass DeepCSV medium working point), and the results are shown in Figures A.3.

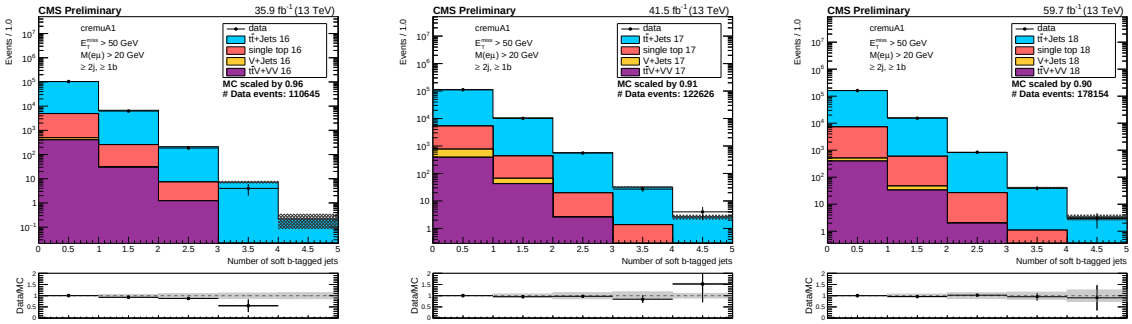

Figure A.3: The distribution of the number of soft b tags in the eμ control region with ≥ 2 jets, ≥ 1b, for the data taking period and their corresponding simulation in 2016 (left), 2017 (middle) and 2018 (right).

The difference in tagging efficiencies have also been investigated for the Fullsim and

*The signal contamination in control regions reduces the signal sensitivity, see Section 5.2.1 for more detail.

Fastsim $t\bar{t}$ samples. The tagging efficiency and fake rate of the soft b identification is estimated from simulation in a sample of $e\mu$ cross-check region selections with 1 b-tagged jet. A subset of the sample is selected for events with a generator level b quark coming from a top decay that is not overlapping with any other good jet in the event but is matched to a secondary vertex. The efficiency is estimated by the percentage of these events that pass the soft b identification requirements. The ratio between the efficiencies in Fullsim and Fastsim is defined as the Fullsim to Fastsim scale factor, derived separately for samples corresponding to the 3 years. They are applied on top of the Fullsim to data scale factors described above to the SUSY signal events, which are generated by the Fastsim program.

The modeling by the simulation for the reconstruction efficiency as a function of pile-up has been checked and found consistent with those in data (Figure A.4).

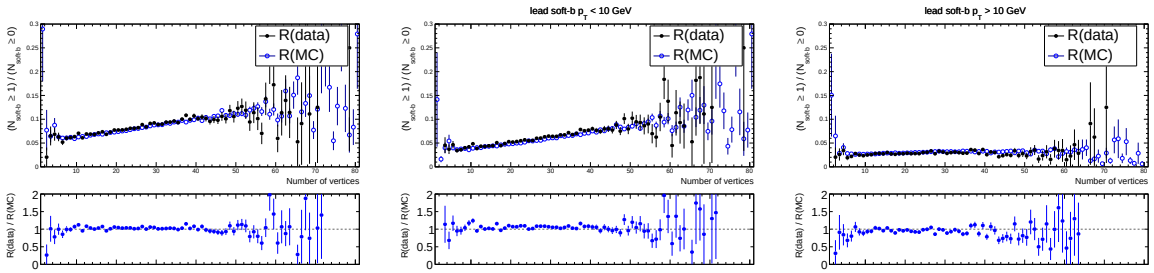

Figure A.4: The double ratio between data and simulation on ratios number of vertices distribution between events with ≥ 1 soft b tag and events ≥ 0 soft b tag. For all soft b tags (left), soft b tags with $p_{\mathrm{T}} < 10\,\mathrm{GeV}$ (middle) and soft b tags with $p_{\mathrm{T}} > 10\,\mathrm{GeV}$ (right).

Appendix B

Reinterpretations

Apart from setting exclusion limits on the top squark signals, the observations in Section 5.1 can also be used to set limits on other beyond the SM models with a $\mathrm{t\bar{t}} + E_{\mathrm{T}}^{\mathrm{miss}}$ signature.

B.1 Constraining invisible H decay

One of these examples is the model when the Higgs boson has extra decay channels into yet unknown particles that are invisible to the detector, and the Higgs boson is produced in association with $\mathrm{t\bar{t}}$ (i.e. the $\mathrm{t\bar{t}H}$ process). Figure B.1 shows the expected yields from the hypothesis for a $\mathrm{t\bar{t}H}$ production at the LHC with the production cross section at 0.507 pb and the H boson is decaying to invisible particles with branching ratio (BR) of 100%. Since this signal does not have a $E_{\mathrm{T}}^{\mathrm{miss}}$ spectrum that is as hard as the $\tilde{\mathrm{t}}\bar{\tilde{\mathrm{t}}}$ signals, the most sensitive signal regions are now the ones with the top tag requirements.

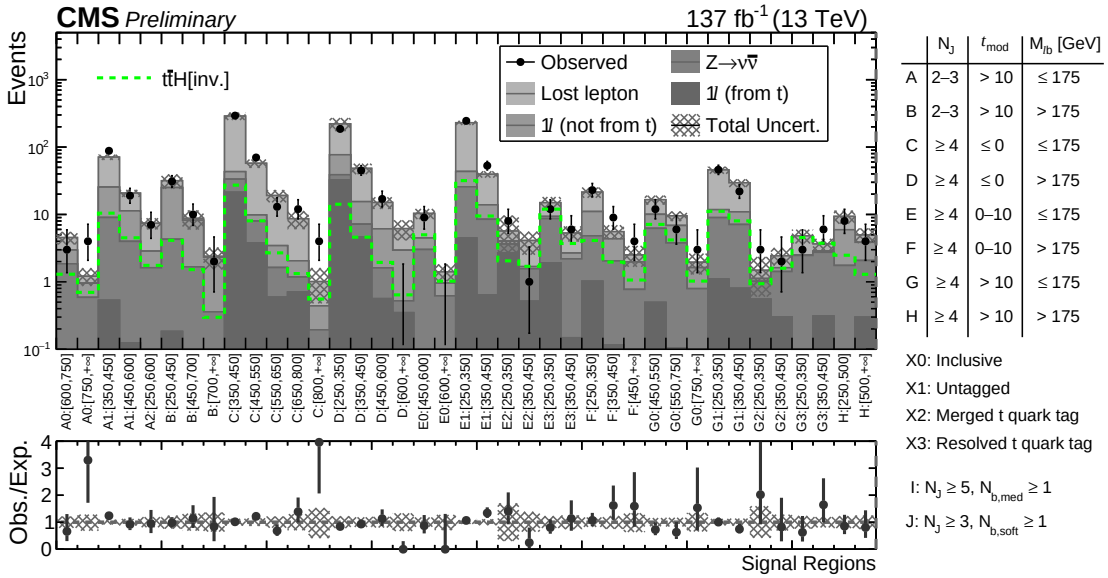

Figure B.1: The observed and expected yields in Tables 5.1 and their ratios, overlaid by the expected yields from the hypothesis with $t\bar{t}H$ production and the H boson is decaying to invisible particles with a BR of 100%. The predicted SM contributions are shown as stacked histograms, the statistical and systematic uncertainties are summed in quadrature and are shown as shaded bands.

From our results, we found the 95% CL observed (expected) upper limit for $\sigma_{t\bar{t}H} \times$ BR(H $\rightarrow$ inv.) to be 0.20 (0.22) pb.

B.2 Constraining $t\bar{t}$+DM models

Another example is for models with direct dark matter (DM) production at the LHC, in the case when the DM particle is produced in association with a $t\bar{t}$ pair, and we refer to this type of scenarios as $t\bar{t}$+DM models. Figure B.2 shows the diagram of an example of such models through either a scalar (ϕ) or pseudoscalar (a) mediator particle. If the interactions between the SM particles and the mediator is Yukawa-like, i.e. the coupling strength is proportional to the particle mass, the $t\bar{t}$+DM will be the preferred channel

to detect the production of DM at the LHC.

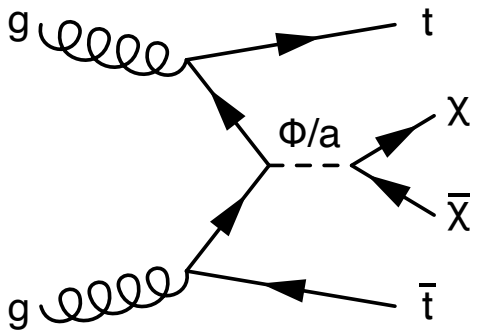

Figure B.2: Diagram of direct DM production through a scalar (ϕ) or pseudoscalar (a) mediator particle, in association with a top quark pair.

Figure B.3 shows again the SM background predictions and the observed data in our standard search regions, but overlaid with the expected yields from two example models of $t\bar{t}$+DM production at the LHC.

The reinterpretation of the $t\bar{t}$+DM models has been carried out in the combined top squark searches [67] including also the searches in the dilepton final state [68] and the all-hadronic final state [60]. Exclusion limits has been derived in the context of simplified models of associated production of DM particles with a top quark pair, assuming a fermionic DM particle with mass at 1 GeV, is shown in Figure B.4 taken from [67].

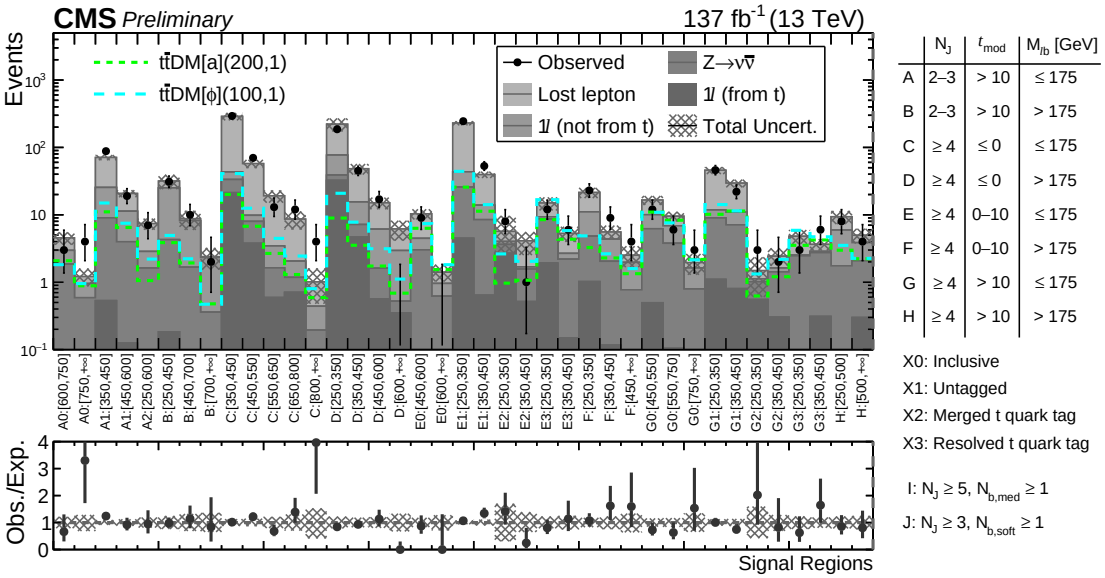

Figure B.3: The observed and expected yields in Tables 5.1 and their ratios, overlaid by the expected yields from two hypotheses of $t\bar{t}$+DM productions featuring either a scalar (ϕ) or pseudoscalar (a) mediator. The predicted SM contributions are shown as stacked histograms, the statistical and systematic uncertainties are summed in quadrature and are shown as shaded bands.

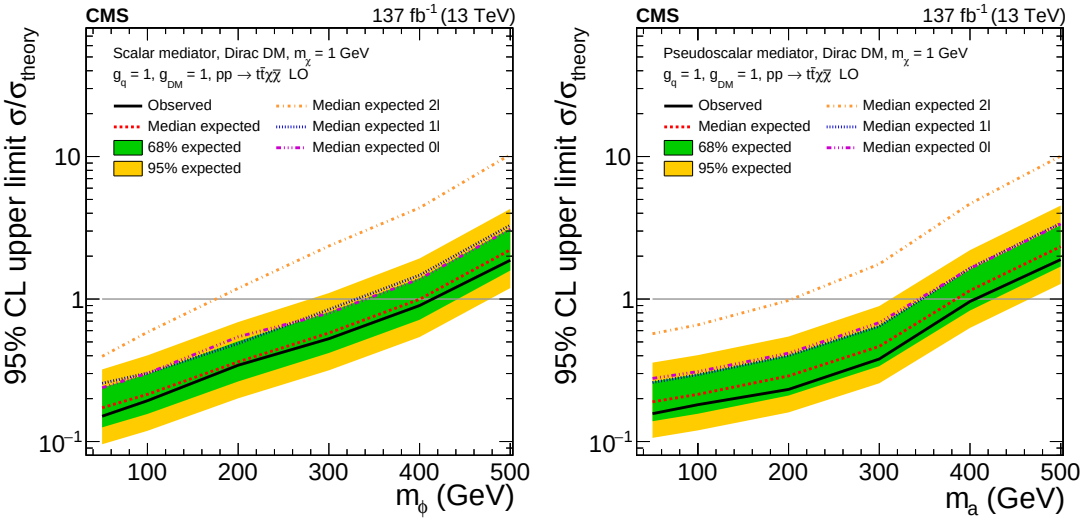

Figure B.4: The 95% CL expected (dashed line) and observed limits (solid line) on $\sigma/\sigma_{\text{theory}}$ from [67], for a fermionic DM particle with mass of 1 GeV, as a function of the mediator mass for a scalar (left) and pseudoscalar (right). The green and yellow bands represent the regions containing 68 and 95%, respectively, of the distribution of limits expected under the background-only hypothesis. The horizontal gray line indicates $\sigma/\sigma_{\text{theory}} = 1$. The mediator couplings are set 1 at both ends.

Bibliography

[1] S.L. Glashow, *Partial Symmetries of Weak Interactions*, *Nucl. Phys.* **22** (1961) 579.

[2] S. Weinberg, *A Model of Leptons*, *Phys. Rev. Lett.* **19** (1967) 1264.

[3] A. Salam, *Weak and Electromagnetic Interactions*, *Conf. Proc. C* **680519** (1968) 367.

[4] A. Loureiro et al., *On The Upper Bound of Neutrino Masses from Combined Cosmological Observations and Particle Physics Experiments*, *Phys. Rev. Lett.* **123** (2019) 081301 [1811.02578].

[5] D. Clowe, A. Gonzalez and M. Markevitch, *Weak lensing mass reconstruction of the interacting cluster 1E0657-558: Direct evidence for the existence of dark matter*, *Astrophys. J.* **604** (2004) 596 [astro-ph/0312273].

[6] M. Markevitch, A.H. Gonzalez, D. Clowe, A. Vikhlinin, L. David, W. Forman et al., *Direct constraints on the dark matter self-interaction cross-section from the merging galaxy cluster 1E0657-56*, *Astrophys. J.* **606** (2004) 819 [astro-ph/0309303].

[7] R. Barbieri and G.F. Giudice, *Upper Bounds on Supersymmetric Particle Masses*, *Nucl. Phys. B* **306** (1988) 63.

[8] P. Fayet, *Spontaneously Broken Supersymmetric Theories of Weak, Electromagnetic and Strong Interactions*, *Phys. Lett. B* **69** (1977) 489.

[9] S. Dimopoulos and H. Georgi, *Softly Broken Supersymmetry and SU(5)*, *Nucl. Phys. B* **193** (1981) 150.

[10] R. Haag, J.T. Lopuszanski and M. Sohnius, *All Possible Generators of Supersymmetries of the s Matrix*, *Nucl. Phys. B* **88** (1975) 257.

[11] G.R. Farrar and P. Fayet, *Phenomenology of the Production, Decay, and Detection of New Hadronic States Associated with Supersymmetry*, *Phys. Lett. B* **76** (1978) 575.

[12] M. Papucci, J.T. Ruderman and A. Weiler, *Natural SUSY Endures*, *JHEP* **09** (2012) 035 [1110.6926].

[13] L.R. Evans and P. Bryant, *LHC Machine*, *JINST* **3** (2008) S08001. 164 p.

[14] CMS collaboration, *The CMS Experiment at the CERN LHC*, *JINST* **3** (2008) S08004.

[15] CMS collaboration, *CMS Physics: Technical Design Report Volume 1: Detector Performance and Software*, .

[16] CMS collaboration, *Cutaway diagrams of CMS detector*, .

[17] CMS collaboration, *Particle-flow reconstruction and global event description with the CMS detector*, *JINST* **12** (2017) P10003 [1706.04965].

[18] CMS collaboration, *Description and performance of track and primary-vertex reconstruction with the CMS tracker*, *JINST* **9** (2014) P10009 [1405.6569].

[19] CMS collaboration, *The Phase-2 Upgrade of the CMS Tracker*, .

[20] CMS collaboration, *Electron and photon reconstruction and identification with the CMS experiment at the CERN LHC*, *JINST* **16** (2021) P05014 [2012.06888].

[21] CMS collaboration, *The Phase-2 Upgrade of the CMS Endcap Calorimeter*, .

[22] CMS collaboration, *The Phase-2 Upgrade of the CMS Muon Detectors*, .

[23] CMS collaboration, *Performance of the CMS muon detector and muon reconstruction with proton-proton collisions at* $\sqrt{s}$ *= 13 TeV*, *JINST* **13** (2018) P06015 [1804.04528].

[24] CMS collaboration, *The CMS trigger system*, *JINST* **12** (2017) P01020 [1609.02366].

[25] W. Beenakker, C. Borschensky, M. Krämer, A. Kulesza and E. Laenen, *NNLL-fast: predictions for coloured supersymmetric particle production at the LHC with threshold and Coulomb resummation*, *JHEP* **12** (2016) 133 [1607.07741].

[26] W. Beenakker, C. Borschensky, R. Heger, M. Krämer, A. Kulesza and E. Laenen, *NNLL resummation for stop pair-production at the LHC*, *JHEP* **05** (2016) 153 [1601.02954].

[27] CMS collaboration, *Interpretation of Searches for Supersymmetry with Simplified Models*, *Phys. Rev. D* **88** (2013) 052017 [1301.2175].

[28] CMS collaboration, *Search for direct production of supersymmetric partners of the top quark in the all-jets final state in proton-proton collisions at* $\sqrt{s} = 13$ *TeV*, *JHEP* **10** (2017) 005 [1707.03316].

[29] CMS collaboration, *Search for top squark pair production in pp collisions at* $\sqrt{s} = 13$ *TeV using single lepton events*, *JHEP* **10** (2017) 019 [1706.04402].

[30] CMS collaboration, *Search for top squarks and dark matter particles in opposite-charge dilepton final states at* $\sqrt{s} = 13$ *TeV*, *Phys. Rev. D* **97** (2018) 032009 [1711.00752].

[31] CMS collaboration, *Search for direct top squark pair production in events with one lepton, jets, and missing transverse momentum at 13 TeV with the CMS experiment*, *JHEP* **05** (2020) 032 [1912.08887].

[32] R. Brun and F. Rademakers, *ROOT: An object oriented data analysis framework*, *Nucl. Instrum. Meth. A* **389** (1997) 81.

[33] J. Alwall, R. Frederix, S. Frixione, V. Hirschi, F. Maltoni, O. Mattelaer et al., *The automated computation of tree-level and next-to-leading order differential cross sections, and their matching to parton shower simulations*, *JHEP* **07** (2014) 079 [1405.0301].

[34] P. Nason, *A New method for combining NLO QCD with shower Monte Carlo algorithms*, *JHEP* **11** (2004) 040 [hep-ph/0409146].

[35] S. Frixione, P. Nason and C. Oleari, *Matching NLO QCD computations with Parton Shower simulations: the POWHEG method*, *JHEP* **11** (2007) 070 [0709.2092].

[36] S. Alioli, P. Nason, C. Oleari and E. Re, *A general framework for implementing NLO calculations in shower Monte Carlo programs: the POWHEG BOX*, *JHEP* **06** (2010) 043 [1002.2581].

[37] E. Re, *Single-top Wt-channel production matched with parton showers using the POWHEG method*, *Eur. Phys. J. C* **71** (2011) 1547 [1009.2450].

[38] NNPDF collaboration, *Parton distributions for the LHC Run II*, *JHEP* **04** (2015) 040 [1410.8849].

[39] NNPDF collaboration, *Parton distributions from high-precision collider data*, *Eur. Phys. J. C* **77** (2017) 663 [1706.00428].

[40] T. Sjöstrand, S. Ask, J.R. Christiansen, R. Corke, N. Desai, P. Ilten et al., *An introduction to PYTHIA 8.2*, *Comput. Phys. Commun.* **191** (2015) 159 [1410.3012].

[41] J. Alwall et al., *Comparative study of various algorithms for the merging of parton showers and matrix elements in hadronic collisions*, *Eur. Phys. J. C* **53** (2008) 473 [0706.2569].

[42] R. Frederix and S. Frixione, *Merging meets matching in MC@NLO*, *JHEP* **12** (2012) 061 [1209.6215].

[43] CMS collaboration, *Event generator tunes obtained from underlying event and multiparton scattering measurements*, *Eur. Phys. J. C* **76** (2016) 155 [1512.00815].

[44] CMS collaboration, *Extraction and validation of a new set of CMS PYTHIA8 tunes from underlying-event measurements*, *Eur. Phys. J. C* **80** (2020) 4 [1903.12179].

[45] GEANT4 collaboration, *GEANT4–a simulation toolkit*, *Nucl. Instrum. Meth. A* **506** (2003) 250.

[46] CMS collaboration, *The fast simulation of the CMS detector at LHC*, *J. Phys. Conf. Ser.* **331** (2011) 032049.

[47] A. Giammanco, *The Fast Simulation of the CMS Experiment*, *J. Phys. Conf. Ser.* **513** (2014) 022012.

[48] CMS collaboration, *Performance of the reconstruction and identification of high-momentum muons in proton-proton collisions at* $\sqrt{s} = 13$ *TeV*, *JINST* **15** (2020) P02027 [1912.03516].

[49] CMS collaboration, *Performance of reconstruction and identification of* τ *leptons decaying to hadrons and* ν_τ *in pp collisions at* $\sqrt{s} = 13$ *TeV*, *JINST* **13** (2018) P10005 [1809.02816].

[50] M. Cacciari and G.P. Salam, *Dispelling the* N^3 *myth for the* k_t *jet-finder*, *Phys. Lett. B* **641** (2006) 57 [hep-ph/0512210].

[51] M. Cacciari, G.P. Salam and G. Soyez, *The anti-*k_t *jet clustering algorithm*, *JHEP* **04** (2008) 063 [0802.1189].

[52] M. Cacciari, G.P. Salam and G. Soyez, *FastJet user manual*, *Eur. Phys. J. C* **72** (2012) 1896 [1111.6097].

[53] M. Cacciari and G.P. Salam, *Pileup subtraction using jet areas*, *Phys. Lett. B* **659** (2008) 119 [0707.1378].

[54] CMS collaboration, *Jet energy scale and resolution in the CMS experiment in pp collisions at 8 TeV*, *JINST* **12** (2017) P02014 [1607.03663].

[55] CMS collaboration, *Identification of heavy-flavour jets with the CMS detector in pp collisions at 13 TeV*, *JINST* **13** (2018) P05011 [1712.07158].

[56] CMS collaboration, *Measurement of $B\bar{B}$ Angular Correlations based on Secondary Vertex Reconstruction at $\sqrt{s} = 7$ TeV*, *JHEP* **03** (2011) 136 [1102.3194].

[57] CMS collaboration, *Missing transverse energy performance of the CMS detector*, *JINST* **6** (2011) P09001 [1106.5048].

[58] CMS collaboration, *Performance of missing transverse momentum reconstruction in proton-proton collisions at $\sqrt{s} = 13$ TeV using the CMS detector*, *JINST* **14** (2019) P07004 [1903.06078].

[59] M.L. Graesser and J. Shelton, *Hunting mixed top squark decays*, *Phys. Rev. Lett.* **111** (2013) 121802 [1212.4495].

[60] CMS collaboration, *Search for top squark production in fully-hadronic final states in proton-proton collisions at $\sqrt{s} = 13$ TeV*, 2103.01290.

[61] CMS collaboration, *Identification of heavy, energetic, hadronically decaying particles using machine-learning techniques*, *JINST* **15** (2020) P06005 [2004.08262].

[62] CMS collaboration, *Measurement of the cross section for top quark pair production in association with a W or Z boson in proton-proton collisions at $\sqrt{s} = 13$ TeV*, *JHEP* **08** (2018) 011 [1711.02547].

[63] T. Junk, *Confidence level computation for combining searches with small statistics*, *Nucl. Instrum. Meth. A* **434** (1999) 435 [hep-ex/9902006].

[64] A.L. Read, *Presentation of search results: The CL(s) technique*, *J. Phys. G* **28** (2002) 2693.

[65] G. Cowan, K. Cranmer, E. Gross and O. Vitells, *Asymptotic formulae for likelihood-based tests of new physics*, *Eur. Phys. J. C* **71** (2011) 1554 [1007.1727].

[66] T.L.H.C.G. The ATLAS Collaboration, The CMS Collaboration, *Procedure for the LHC Higgs boson search combination in Summer 2011*, Tech. Rep. CMS-NOTE-2011-005, ATL-PHYS-PUB-2011-11, CERN, Geneva (Aug, 2011).

[67] CMS collaboration, *Combined searches for the production of supersymmetric top quark partners in proton-proton collisions at $\sqrt{s} = 13$ TeV*, 2107.10892.

[68] CMS collaboration, *Search for top squark pair production using dilepton final states in pp collision data collected at $\sqrt{s} = 13$ TeV*, *Eur. Phys. J. C* **81** (2021) 3 [2008.05936].

[69] Y. Ganin and V. Lempitsky, *Unsupervised Domain Adaptation by Backpropagation*, *arXiv e-prints* (2014) [1409.7495].

[70] CMS collaboration, *Search for the pair production of third-generation squarks with two-body decays to a bottom or charm quark and a neutralino in proton–proton collisions at $\sqrt{s}$ = 13 TeV*, *Phys. Lett. B* **778** (2018) 263 [1707.07274].